



저작자표시-비영리-변경금지 2.0 대한민국

이용자는 아래의 조건을 따르는 경우에 한하여 자유롭게

- 이 저작물을 복제, 배포, 전송, 전시, 공연 및 방송할 수 있습니다.

다음과 같은 조건을 따라야 합니다:



저작자표시. 귀하는 원저작자를 표시하여야 합니다.



비영리. 귀하는 이 저작물을 영리 목적으로 이용할 수 없습니다.



변경금지. 귀하는 이 저작물을 개작, 변형 또는 가공할 수 없습니다.

- 귀하는, 이 저작물의 재이용이나 배포의 경우, 이 저작물에 적용된 이용허락조건을 명확하게 나타내어야 합니다.
- 저작권자로부터 별도의 허가를 받으면 이러한 조건들은 적용되지 않습니다.

저작권법에 따른 이용자의 권리는 위의 내용에 의하여 영향을 받지 않습니다.

이것은 [이용허락규약\(Legal Code\)](#)을 이해하기 쉽게 요약한 것입니다.

[Disclaimer](#)

공학박사 학위논문

A study on the improvement of
corrosion property on
biodegradable magnesium via
laser surface treatment

생분해성 마그네슘 합금의 레이저 표면 처리를
통한 부식 저항성 개선에 관한 연구

2022년 8월

서울대학교 대학원
공과대학 재료공학부
박재호

A study on the improvement of
corrosion property on biodegradable
magnesium via laser surface
treatment

생분해성 마그네슘 합금의 레이저 표면 처리를 통한
부식 저항성 개선에 관한 연구

지도교수 선 정 윤

이 논문을 공학박사 학위논문으로 제출함
2022년 7월

서울대학교 대학원
공과대학 재료공학부
박 재 호

박재호의 공학박사 학위논문을 인준함
2022년 7월

위 원 장 최 인 석 (인)

부위원장 선 정 윤 (인)

위 원 장 혜 진 (인)

위 원 한 형 섭 (인)

위 원 전 호 정 (인)

Abstract

Magnesium alloys have received extensive recognition as orthopedic materials. They possess mechanical qualities identical to those of bones that no other biomaterial has, and they resolve within the body by promoting bone production. However, the corrosion rate of magnesium alloys is accelerated when they are present in bodily fluids with high concentrations of chloride compounds. Moreover, the rapid change in hydrogen gas and pH that occurs at the beginning of corrosion can cause excessive inflammation and fibrosis in the surrounding tissue, which limits its use as a human body implant. As a result, surface treatment and coating of the material are critical for controlling early stage corrosion reactions.

Laser surface engineering is emerging as a useful tool for the surface modification of materials owing to its simplicity and effectiveness. Surface modification engineering using lasers is possible for non-contact machining and selective processes depending on the conditions of the laser, such as the laser beam size, wavelength, and power. Different effects can be expected; therefore, it is used in a variety of fields. In this study, femtosecond (fs) and nanosecond (ns) laser surface modification or coating processing of Mg and Mg alloys was performed in three different ways to improve the bio-corrosion properties.

In the first part, galvanic corrosion was reduced by controlling the laser power and repetition rate, resulting in a significant decrease in the

corrosion rate of the Mg alloy. The initial corrosion rate decreased by 65% compared to the non-treated samples due to Mg ion elution and the amount of hydrogen gas analysis under hank's balanced salt solution (HBSS). Therefore, we observed surface and phase changes with scanning electron microscopy (SEM) and X-ray diffraction (XRD). By fs laser surface modification, we can control the corrosion rate more precisely, which will allow biomaterials to be used in various fields through optimization of laser treatment on diverse metals.

In the second part, the Mg surface was modified to achieve super-hydrophilic wettability with a micro–nanotextured surface so that the adhesion ability of the biodegradable coating layer was improved to control the corrosion rate. The laser treatment and non-laser treatment groups were compared after coating with the biodegradable polymer PLGA (poly lactic-co-glycolic acid). In the immersion test, the Mg ion assay showed that coatings on laser-treated Mg had fewer Mg ions than the control group. The cross-section of the laser-treated group showed coating layers that infiltrated deeper into the surface. These data indicate that the adhesion strength was improved physically owing to the embedded coating layer between the pits and grooves.

In the third part, hydroxyapatite (HAp) was coated on Mg using nanosecond laser coating, combining the advantages of chemical and physical treatments. The photothermal heat generated in the liquid precursor by the laser improved the adhesion of the coating through the precipitation

and growth of HAp at the localized nanosecond laser focal area and increased the corrosion resistance and cell adhesion of Mg. Physical, crystallographic, and chemical bonding were analyzed to explore the mechanism through which the surface adhesion between Mg and the HAp coating layer increased. The applicability of the coating to Mg screws used in clinical devices and the improvement of its corrosion properties were confirmed. The liquid-environment-based laser surface coating technique offers a simple and quick process that does not require any chemical ligands; therefore, it overcomes a potential obstacle in its clinical use.

Laser surface engineering is emerging as a useful tool for surface modification of materials due to its simple and effective process. Surface modification engineering by laser is possible for non-contact machining and selective process depending on the conditions of the laser such as laser beam size, wavelength, power and so on. It is possible to expect different effects, therefore it is used in variety of fields. In this study, femtosecond (fs) and nanosecond (ns) laser surface modification or coating processing to Mg and Mg alloy in three different ways to improve bio-corrosion properties.

In first part, by controlling the laser power and repetition rate, the galvanic corrosion was reduced, resulting in significantly decreasing the corrosion rate of Mg alloy. Initial corrosion rate was decreased as 65% compared to non-treated samples by Mg ion elution and amount of hydrogen gas analysis under HBSS(Hank' s solution). Therefore, we observed the surface and phase change with SEM (Scanning Electron

Microscope) and XRD (X-ray diffraction). By fs laser surface modification, we can control corrosion rate more precisely, which will allow biomaterials to be used in various fields through optimization of laser treatment on diversity of metal.

In second part, Mg surface was modified to super hydrophilic wettability with micro- nano textured surface so that adhesion ability of biodegradable coating layer was improved for controlling corrosion rate. Laser treatment group and non-laser treatment group were compared after coating with biodegradable polymer PLGA (poly lactic-co-glycolic acid). In immersion test, Mg ion assay showed that coatings on laser treated Mg have less Mg ion than the control group. The cross-section of laser treated group showed coating layers infiltrate deeper onto the surface. From these data, adhesion strength was improved physically due to imbedded coating layer between pits and grooves.

In third part, hydroxyapatite (HAp) was coated on Mg using ns laser coating, combining the advantages of chemical and physical treatments. Photothermal heat generated in the liquid precursor by the laser improved the adhesion of the coating through the precipitation and growth of HAp at the localized ns laser focal area and increased the corrosion resistance and cell adhesion of Mg. The physical, crystallographic, and chemical bonding were analyzed to explore the mechanism through which the surface adhesion between Mg and the HAp coating layer increased. The applicability of the coating to Mg screws used for clinical devices and

improvement in its corrosion property were confirmed. The liquid environment-based laser surface coating technique offers a simple and quick process that does not require any chemical ligands, and therefore, overcomes a potential obstacle in its clinical use.

Keywords: Laser surface treatment, Femtosecond laser, Nanosecond laser, Metal surface, Corrosion property, Coating

Student Number: 2018-36640

Table of Contents

Abstract	i
List of Tables.....	viii
List of Figures	ix
Chapter 1. Introduction.....	1
1.1 Study Background.....	1
1.1.1 Outline about biomaterials.....	1
1.1.2 Metallic biomaterials and their limitation.....	3
1.1.3 Magnesium and Mg alloy as biomaterials.....	4
1.1.3.1 Mechanical property.....	5
1.1.3.2 Biocompatibility.....	5
1.1.3.3 Corrosion resistance.....	6
1.1.4 Laser surface modification.....	10
1.1.4.1 Advantages of laser surface treatment.....	10
1.1.4.2 Applications of laser surface engineering.....	12
1.2 Purpose of Research.....	16
Chapter 2. Control of galvanic corrosion via femtosecond laser surface melting	18
2.1 Introduction.....	18
2.2 Experimental Procedures.....	21

2.3 Results and Discussion.....	29
2.4 Conclusion.....	56
Chapter 3. Enhancement of coating ability physically and chemically via fs laser textured surface.....	57
3.1 Introduction.....	57
3.2 Experimental Procedures.....	60
3.3 Results and Discussion.....	66
3.4 Conclusion.....	81
Chapter 4. Hydroxyapatite coating via a laser-induced hydrothermal process in the liquid precursor	82
4.1 Introduction.....	82
4.2 Experimental Procedures.....	84
4.3 Results and Discussion.....	92
4.4 Conclusion.....	120
Chapter 5. Conclusion.....	121
References.....	124
Abstract in Korean.....	144

List of Tables

Table 1. Chemical compositions of the used Mg alloy.

Table 2. Laser processing parameters.

Table 3. Elemental components of laser-treated samples on the surface; Magnesium (Mg), Oxide (O), Calcium (Ca), Phosphate (P)

Table 4. The difference in E_{corr} , I_{corr} , and P_i between specimens, as determined from the polarization test.

List of Figures

Fig. 1.1 Schematic diagram of galvanic corrosion process.

Fig. 1.2 Schematic of laser material processing depending on laser power density as a function of interaction time.

Fig. 2.1 Schematic of laser fs surface treatment experiment setup; fs: femtosecond.

Fig. 2.2 Backscattered electron (BSE) images of specimen surfaces after laser treatment with different repetition rates; scale bar: 100 μm .

Fig. 2.3 Analysis of the secondary phase decrease rate in the matrix after various pulse repetition frequencies (PRF): (a) decreasing rate of phases and (b) BSE images of surfaces after image processing; scale bar: 50 μm .

Fig. 2.4 BSE images of cross-sections of (a) as-received alloy and (b) alloy laser-treated with a 500 Hz pulse repetition frequency (PRF).

Fig. 2.5 AFM images of the alloy after laser surface melting under different pulse repetition frequencies: (a) polished, (b) 62.5 Hz, (c) 500 Hz, (d) 1000 Hz PRF, (e) Surface roughness plots and values from $30 \times 30 \mu\text{m}^2$ before and after laser surface treatment.

Fig. 2.6 Scanning electron microscopy (SEM) image and chemical composition of alloy treated with a 1000 Hz PRF; red arrows indicate ripple shape and columns, yellow arrows indicate secondary phases.

Fig. 2.7 (a) X-ray diffraction (XRD) patterns of as-received (ctrl) and laser-treated alloys; (b) the main peak of Mg matrix enlarged, (c) the main peak of secondary phase enlarged.

Fig. 2.8 Amount of hydrogen gas released by as-received (Ctrl) and laser-treated specimens in immersion tests.

Fig. 2.9 (a) Cyclic polarization curves and (b) EIS measurement for as-received (Ctrl) and laser-treated alloys following immersion in Hank's balanced salt solution (HBSS).

Fig. 2.10 SEM images of surface morphologies of the as-received and laser-treated alloys with different pulse repetition frequencies: (a) as-received, (b) 1000 Hz, (c) 500 Hz, (d) 62.5 Hz PRF; scale bar: 100 μm .

Fig. 2.11 SEM images of cross-sections of samples after immersion in HBSS for 1 week: (a) as-received sample, and after (b) 1000 Hz, (c) 500 Hz, and (d) 62.5 Hz PRF.

Fig. 2.12 BSE images of the boundaries between the as-received and laser-treated surface at three different positions with 500 Hz PRF after immersion

in HBSS for 10 min (left region: laser-treated surface; right region: as-received surface); scale bar: 100 μm .

Fig. 2.13 Microhardness values for the top surfaces of as-received and 500 Hz PRF laser-treated samples.

Fig. 2.14 Cell viability of as-received and laser-treated Mg alloys using various PRFs after immersion testing in Dulbecco's modified eagle medium for 1, 3, and 7 days.

Fig. 3.1 Schematic graphical illustration of PLGA coating on treated Mg surface after formation of hierarchical topography via fs laser.

Fig. 3.2 Characteristics of treated Mg treated by fs laser: (a-d) SEM surface images of the morphology of Mg substrate and (e-h) 3D topography images and depth profile according to each laser parameter. (i) The mean contact angle of laser-treated Mg surface. (j) Weight percent (wt.%) change of Mg (black square) and oxygen (blue triangle) of each laser condition. (k) XRD patterns of as-received (black line; bare) and laser-treated alloy (red line; Canyon).

Fig. 3.3 (a-d) TEM-EDS of cross-section mapping on Canyon surface, (e-h) SAED pattern of the boundary of MgO between Mg. (i) EDAX line profile from the surface to bottom. (j) HR investigation at the boundary of MgO between Mg.

Fig. 3.4 (a) SEM images of a cross-section of samples after spin-coating; PLGA@Bare (left) and PLGA@FsMg (right). (b) Adhesion strength curve between PLGA coating layer between Mg substrates.

Fig. 3.5 (a) Amount of hydrogen gas and (b) concentration of Mg ion released by Ctrl, PLGA@Bare, and PLGA@FsMg. (c) The behavior of coating layer on substrates in immersion test after 7 days (left image: PLGA@Bare; right image: PLGA@FsMg); scale bar indicates 4 mm. (d) SEM images of cross-section after corrosion test (left image: PLGA@Bare; right image: PLGA@FsMg); scale bar indicates 20 μm .

Fig. 3.6 (a) Cell viability of ctrl, PLGA@Bare, coating on PLGA@FsMg after immersion test in DMEM without serum for 1, 3, and 7 days. (b) Cell morphology on surface of ctrl (upper images) and PLGA@FsMg (below images) after corrosion test for 3 days.

Fig. 4.1 Schematic of LISSC in the precursor solution.

Fig. 4.2 (a) Surface analysis of SEM images and roughness profile with 3D microscopy under each solution condition following laser treatment. (b) Mapping images of laser-treated and bare Mg in modified biomimetic solution. Each color indicates Mg (blue), O (green), Ca purple), and P (yellow). The contrast shows the quantity of each element on the surface after laser treatment.

Fig. 4.3 Ratio of Ca and Mg at the modified biomimetic solution.

Fig. 4.4 (a) Electrochemical polarization curve with Ag/AgCl as the standard reference electrode and platinum as the counter electrode. (b) XRD curves of as-received (control) and laser-treated surface in biomimetic solution at 100X concentration.

Fig. 4.5 Comparison of coating ability between thermally indirect layer and the laser-induced coating layer. (a) Illustration of adhesion test. (b) OM images before and after peel-off test in the bare, TFH, and LIH areas. (c, d) SEM and mapping of each element before the adhesion test. (e, f) SEM and distribution of Mg, O, Ca, and P after the peel-off test using adhesive tape. (g) Optical and SEM surface images following the scratch test. (h) Graph representing the critical load of the scratch test where interface breakage occurs.

Fig. 4.6 (a) SEM surface images of coating layer after laser treatment. CaP coating layer evenly formed by laser (left) and peeled coating layer due to poor adhesion at thermally indirect region (right). (b) OM images in DMEM; bare, thermally formed region, and laser-induced coating region at 1,3, 7 days after the peel-off test.

Fig. 4.7 EDS mapping of cross-section 4 weeks following the corrosion test on each area on the Mg surface.

Fig. 4.8 (a) SEM images under each condition after the corrosion test: scratched area (SA) and coated area (CA). (b) Cross-sectional BSE images on each condition at 4 weeks and 8 weeks after the scratch test.

Fig. 4.9 (a) Cross-section of BSE and mapping under each condition 4 weeks after the scratch test. (b) Depth profile analysis at the scratched zones of the TFH and LIH regions. (c) Depth of corrosion as a function of the distance from the scratched zone.

Fig. 4.10 (a) TEM-EDS of cross-section mapping in the LIH region. (b) SAED pattern in the HAp and Mg regions. (c) HR investigation at the boundary between CaP and Mg. (d) Distribution of Mg and Ca at each point of the cross-section. (e) Atomic percent of elements at the sections. TEM-EDS: transmission electron microscopy/energy-dispersive X-ray spectroscopy; SAED: selected area electron diffraction; HR: high-resolution.

Fig. 4.11 (a) SEM images depicting surface morphology after laser processing in DW. The surface was melted by increasing the number of laser loops. (b) Weight percent (wt%) change in oxygen under each laser loop condition. (c) Cross-section images after laser treatment under the 50 loops condition in DW. (d, e) XPS spectra of Mg 2p and O 1s at each loop.

Fig. 4.12 Schematic depicting the mechanism of LIH coating on the Mg substrate.

Fig. 4.13 (a) OM images for Mg screws after corrosion test in DMEM for 1, 3, and 7 days. (b) Cross-section of BSE for each condition of Mg implantable screw for 1 week. (c) EDS Mapping of cross-section after corrosion test 4W on each area on Mg surface.

Fig.4.14 (a) The amount of released Mg ion after corrosion test at 1,3, and 7 days. (b-d) Comparison of cell adhesion at each area; cell nucleolus indicated blue, and actin indicated orange. (e) The analysis of cell adhesion area by calculating image processing.

Chapter 1. Introduction

1.1 Study Background

1.1.1 Outline about biomaterials

Biomaterials are used to compensate for morphometric and functional faults in the human body and comprise artificial organs, rehabilitation instruments, and implants that replace wound tissue [1]. These materials play an essential role in fixing and replacing faulty tissues. As an expanding concept, it means biomaterials are materials in contact with the biological function such as bio-sensor, drug-delivery systems, and orthopedic applications.

From a material perspective, biomaterials can be grouped into three major classes: metals, polymers, and ceramics. Here, a chemically inert polymer is biocompatible but is to be vulnerable to wear resistance and has low strength. Compared to polymers, ceramics are more suitable for hard tissues because they have superior wear and thermal resistance. However, ceramics are brittle and can be easily broken and damaged, even with a weak external impact. In contrast, metals have a high mechanical strength and elastic modulus. In addition, permanent materials can release toxic ions or products when they corrode and wear in the human body.

Currently, widely used biodegradable materials have drawbacks. The polymer has poor mechanical properties and can degrade acids in the living body. Ceramics have the shortcoming of low fracture toughness. However, degradable metal has been considered a prime candidate material in living systems for its appropriate mechanical property, biocompatibility, and corrosion and wear property. Each material needs to be used in the field with a sufficient understanding of the material.

Among these materials, metals have been evaluated as attractive applications because of their benefits in orthopedic operations owing to their compatible mechanical properties with bone. Metals can be classified into inactive and active metals based on their stability. Stainless steel, Ti alloy, and Co-Cr alloy are inactive metals, whereas Mg, Zn, and Ca are active metals. The use of inactive metal implants in orthopedic surgery could result in their separation owing to side effects and chronic inflammation, which causes problems because the implant has better mechanical properties than human bone. For these reasons, patients who need to be cured of their faulty bone are usually recommended to eliminate inactive metal implants used for curing following the recovery of wound tissue. Secondary surgery is accompanied by psychological stress, financial burden, and risks. In contrast, active implants in a living system, namely, biodegradable metallic materials, heal fractures, replace broken bone, and degrade themselves. The use of biodegradable metallic materials for implantation is advantageous because it

does not require secondary surgery after implantation. Therefore, research on biodegradable metals has been conducted for several years.

1.1.2 Metallic biomaterials and their limitation

A variety of metallic elements, including iron (Fe), chromium (Cr), cobalt (Co), nickel (Ni), titanium (Ti), and magnesium (Mg), have been used in implantable biomedical devices. These metallic materials are used for the manufacturing of metal alloys that are mostly utilized for treatment-related hard tissue owing to their outstanding mechanical properties and compatibility. For example, 316 L stainless steel (316LSS), cobalt-chromium alloys (Co-Cr), and titanium alloys (Ti alloys) are widely used as inert orthopedic implant materials [2].

However, these alloys can excrete toxic components, such as Ni, Cr, and Co, when degrading themselves in the human environment. It has been reported that Ni is detrimental to the skin, resulting in skin ailments and promoting an alleged reaction [3, 4]. In addition, 316LSS, Cr-Co alloys, and Ti have a higher modulus of elasticity than natural bone, resulting in a stress-shielding effect that causes a difference in the elastic modulus between the metal and hard tissue. Most of the forces are transmitted to an object that has a high modulus of elasticity under the same conditions so that the circulation of the load is restricted to one side. When this effect

occurs in the human system, the hard tissue, which has a lower elastic modulus than metal implants, becomes vulnerable due to anaplasia. It could lead to osteolysis and osteoporosis by diminishing the density or weight of the bone. For these reasons, secondary surgery to remove inactive implants after fixation is indispensable for patients but also has many drawbacks [1].

1.1.3 Magnesium and Mg alloy as biomaterials

Magnesium has an atomic number of 12 and is the eighth-most abundant element on earth. The common oxidation number of Mg is +2, and Mg ions have high solubility in water. The crystal structure of Mg is hexagonal close-packed (HCP), and the c/a value is 1.624, which is close to the ideal structure of HCP.

It has been reported that the density of Mg is 1.74–2.0 g/cm³, which is similar to that of hard tissue (1.8–2.1g/cm³) in humans and lower than that of Ti (4.4–4.5g/cm³) [2, 5]. The fracture toughness of Mg is higher than that of ceramic. With an elastic modulus similar to that of bone, Mg-based alloys prevent the stress-shielding effect.

In addition, Mg is an essential element that occupies a large amount of the fourth mineral that makes up the human body. In addition, calcium ions and phosphoric acid in body fluid also react to form calcium phosphate, which is a material similar to bone [2].

For these reasons, among biodegradable metallic materials, Mg is considered a potential candidate for orthopedic applications because of its excellent biocompatibility and mechanical properties, which are similar to those of the human bone [6]. Mg has not only these benefits but also the characteristics of degradation in the living system, which meets the essential requirements of biodegradable implants [7].

1.1.3.1 Mechanical property

The mechanical properties of Mg-based alloys, such as strength, elastic modulus, and elongation, are similar to those of natural bone. The tensile strength and elongation of the Mg alloy were 86.8–280 MPa, and 3–21.8%, respectively. These properties have been improved by an advanced casting process and the design of alloying-added elements. In a previous study, it was reported that the mechanical properties of alloys were improved by including components such as Al, Ag, Si, Sn, Zn, and Zr. By applying an effective process, the elongation of the alloys is enhanced as well [8].

1.1.3.2 Biocompatibility

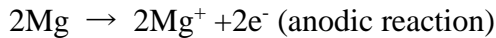
The total amount of Mg stored in the body is estimated to be 1 mol of a normal adult (70 kg), with approximately half of the Mg in the natural

bone. The concentration of Mg ions in the extracellular fluid ranges between 0.7 and 1.05 mmol/L. A serum Mg concentration exceeding the permitted limit can lead to excretion of the element in urine to maintain homeostasis [9]. Mg is biocompatible, and additional elements for reinforcing the mechanical properties of Mg alloys should be nontoxic. Typical alloying elements in Mg-based alloys are calcium (Ca), zinc (Zn), manganese (Mn), and zirconium (Zr), which are present in the human body. While Ca is a major ingredient of bone, the alloys that contain Ca have a density of 1.55g/cm² resulting in a lessening gap in that of natural bone. It has been evaluated that the addition of Zn, Mn, and Zr enhances mechanical and corrosion properties by changing microstructure such as grain sizes and phases [10].

1.1.3.3 Corrosion resistance

It has been reported that the period of healing wounds such as hard tissue and making new bone on fracture ranges from three to four months in orthopedic applications. Degradable implants are required to maintain the mechanical properties of the application. It fulfills the purpose of fixation to prevent fractures and breaks before degradation [11].

Mg is one of the active metals with a standard reduction potential of -2.37V with regard to the standard hydrogen electrode. The corrosion of Mg during dissolution occurs via the following reaction [12]:



The radical formation of hydrogen gas in the corrosion reaction leads to a change in pH. Such behavior of Mg causes excessive inflammation and fibrosis progression around the tissues.

The major mechanisms of Mg are classified into three typical forms: galvanic, pitting, and intergranular corrosion [13]. Galvanic corrosion occurs when two different metals with different electrochemical potentials are in physical (electronic) contact and soaked in ionic conducting fluid media, such as serum or interstitial fluid. This is also referred to as coupled corrosion.

Galvanic corrosion is a major obstacle to the use of Mg in an aggressive environment. Because Mg was the most active metal in the

galvanic series, an Mg-based alloy implant was always an active anode if it was in contact with the other metal. Even in the same materials, galvanic corrosion can occur between the matrix and intermetallic particles.

Pitting corrosion occurs at the free corrosion potential of Mg when it is exposed to chloride ions in a medium. Pitting corrosion occurs when discrete areas of a material undergo a rapid attack, whereas the majority of the surface remains virtually unaffected [14].

Intergranular corrosion occurs at the grain boundaries owing to precipitation of the second phase. Grain boundaries are the preferred sites at which precipitation and segregation occur in alloys. It is generally considered that alloys with intermetallic phases or compounds are highly susceptible to intergranular corrosion. Corrosion tends to be concentrated in the area adjacent to the grain boundary until the grain may eventually be undercut and fall out.

Therefore, controlling the corrosion properties of Mg is important to retain its mechanical properties and biocompatibility in the human body. It has been studied to solve the problem of the corrosion rate. Many studies have been conducted to control the corrosion properties of Mg-based alloys, including alloy design and surface modifications such as coating, laser melting, and chemical treatment [15-18].

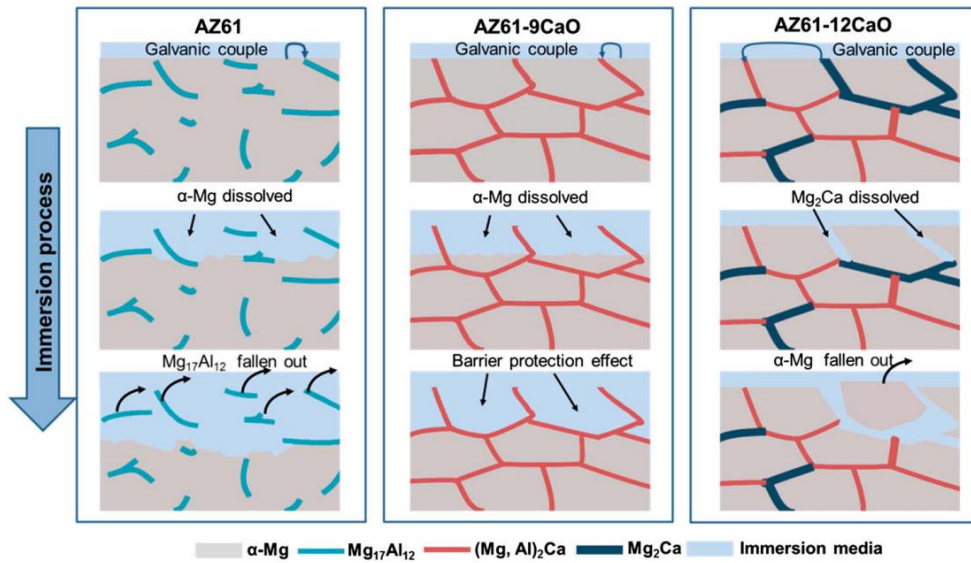


Fig. 1.1 Schematic diagram of galvanic corrosion process [19].

1.1.4 Laser surface modification

1.1.4.1 Advantages of laser surface modification

Surface modification using laser has the following advantages [20, 21] :

- With simple operation, it is possible to induce various engineering applications, such as laser surface hardening, surface annealing, shocking peening, surface texturing, cladding, alloying, and cutting.
- It was utilized by localized heating from the laser beam, resulting in reduced thermal distortion and size of the heat-affected zone (HAZ), and thereby does not alter the bulk properties of the material (especially fs laser). Refinement and homogenization of the microstructure in the laser-processed regime led to improved mechanical properties and corrosion resistance.
- Controlled levels of dilution within the coating and metallurgical bonding at the interface.
- The ability to synthesize novel corrosion and wear resistance phases owing to the nonequilibrium nature of the process.

For these reasons, by properly selecting the laser processing parameters, the topography and chemistry of the implant surfaces can be optimized for desired biomedical applications.

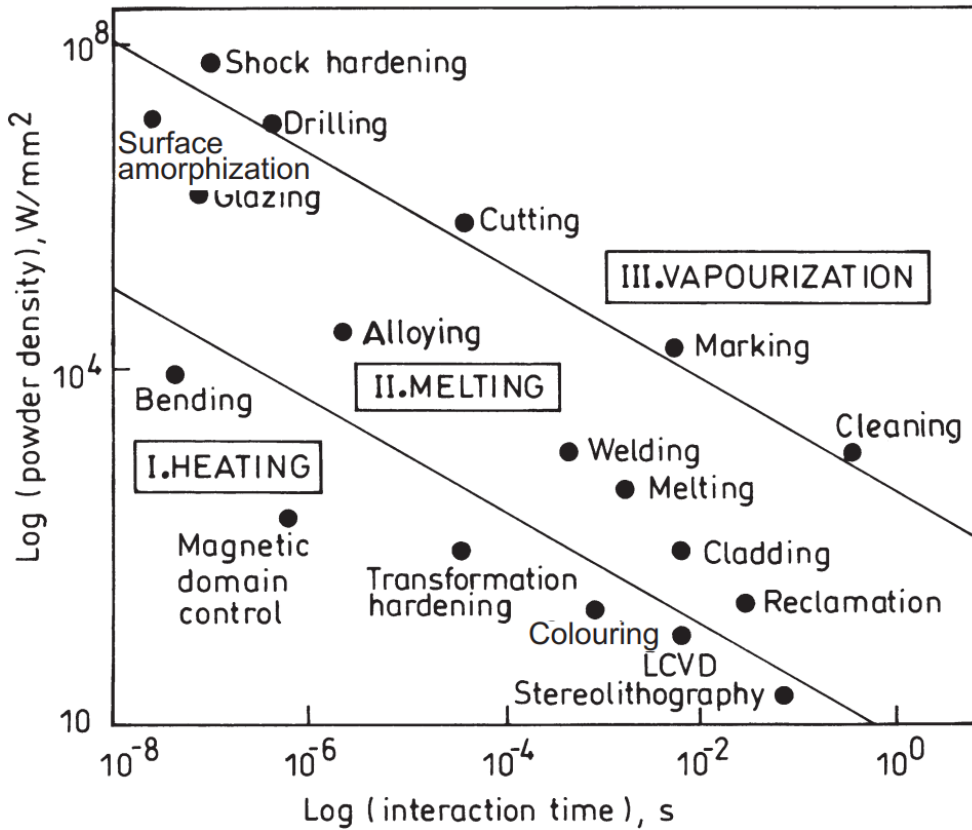


Fig. 1.2 Schematic of laser material processing depending on laser power density as a function of interaction time [22].

1.1.4.2 Applications of laser surface engineering

Laser surface melting (LSM) engineering, which was proposed in the late 1980s, is a recently developed manufacturing process [23-25]. LSM has numerous advantages over conventional techniques such as simple production processing steps, flexibility, and efficiency. Furthermore, because the metal has a high melting point, LSM improves the surface properties by rapid solidification, homogenization, dissolution of the second phases, and refinement of the microstructure on the surface.

A previous study of LSM employed by Liu et al. observed that LSM enhances the corrosion property of AM60B Mg alloy associated with the distribution of the second phase and grain refinement [26]. Mondal et al. reported an improvement in the corrosion and wear resistance of ACM720 Mg alloy by laser surface treatment because of the fast cooling rate and solid solution strengthening [27]. Taltavull et al. pointed out that the β -phase is molten while the Mg matrix remains solid using selective LSM of the AZ91D alloy [28]. Abbas et al. reported a similar development for AZ31, AZ61, and WE43 alloys with the distribution of the β -phase using a continuous-wave CO₂ laser [29]. Some authors have already suggested an enhancement in corrosion characteristics using an excimer nanosecond-pulsed laser [30-34]. However, because of the accompanying heat-affected

zone, which is caused by thermal stresses using conventional laser engineering, surface modification requires control of the pulse duration and laser beam power during the process [35, 36]. The purpose of the current study is to improve the corrosion of Mg alloys by fs laser, which affects the minimal melted layer without changing the mechanical properties of the Mg matrix.

Direct writing technology has been the most widely examined for variable material surfaces, such as micro-and nanotextured surfaces, because of its simple and effective process [37-40]. This laser technology can be used to change the surface morphology of a wide range of materials, allowing the texturing of non-planar surfaces. In addition, laser surface engineering enables maskless single-step processes on a material in an ambient air environment without a vacuum. Textured morphology, such as columns, pillars, and worms, is another laser-induced structure observed on various materials (metals, semiconductors, and polymers) with ultrashort-pulsed width [41]. Furthermore, this technology enables not only the production of micro patterns but also the formation of nanoparticles and nanoscale patterns on the surface. Because of the numerous applications of these types of structures, the ultrafast laser fabrication of changed structures on the surface has been extensively highlighted in the field. In addition, changes in surface morphology result in several properties, such as roughness, energy state, and wettability, which lead to modification

into a hydrophilic or hydrophobic state. Vorobyev et al. found that laser surface texturing allows for variable nanostructures with a period of micro-roughness of commercially pure titanium [42]. Ahmmed et al. suggested that each textured surface topography can be influenced by electron-phonon coupling and thermal conductivity using femtosecond laser surface texturing on titanium, stainless steel, aluminum, and copper [43]. Kam et al. reported that creating a wide range of micro-cone densities on AISI 316 L stainless steel is controlled by simple femtosecond laser irradiation depending on the pulse energy, repetition rate, and scan speed, leading to changes in wettability, such as the hydrophobic and hydrophilic states [44]. Similarly, Demir et al. reported that variable microstructures, such as transition, worms, buds, and cauliflower, can be formed using laser structuring on AZ91 Mg alloy, which shows an effective change in wetting behavior [45]. Zorba et al. demonstrated that it is possible to render silicon hydrophobic via femtosecond laser surface treatment [46]. In contrast, Demir et al. reported that the wettability of laser-treated surfaces, such as worms, is modified into a hydrophilic behavior [47].

Another approach has been studied for laser irradiation, specifically laser processing, in a supersaturated solution. This method combines a physical laser process and a chemical precipitation reaction in a single step, allowing for rapid and localized coating at the laser-irradiated solid-liquid interface (i.e., the interface between a substrate and a metastable

supersaturated solution) [48-52]. Prior to immersion in a supersaturated CaP solution, laser stimulation was employed as the CaP pre-coating method [53-55]. Recently, these two-step approaches have been enhanced, and a one-step CaP coating was accomplished using a laser-induced single-step coating (LISSC) process. LISSC employs the effect of hydrothermal synthesis at a laser-irradiated solid (substrate)/liquid (coating precursor solution) interface. Deposition from the liquid state has advantages over other states of matter in terms of relative ease of handling, simple setup, and recyclability [56-59]. In addition, with the LISSC coating, simultaneous synthesis and coating are possible on the surface of the material where the laser is focused. Therefore, various coating layers comprising the desired materials can be formed depending on the type of immersion solution.

Oyane et al. reported a laser liquid–solid interaction process as a CaP pre-coating technique that utilizes laser processing on metal and polymer substrates in supersaturated CaP solutions [60-63]. In this process, unfocused pulsed laser light is irradiated by scanning a substrate immersed in an SBF. Um et al. demonstrated that it was possible to coat and synthesize CaP simultaneously on a Ti alloy using the LISSC method. The substrate has been used as a bio-inert material in these; therefore, attempts are needed to apply it to biodegradable materials.

In conclusion, the liquid-environment-based laser surface coating technique provides a simple and quick process that does not require any chemical ligand; hence, it circumvents a potential obstacle in its clinical use.

1.2. Purpose of Research

This dissertation covers research on improving the corrosion properties of biodegradable Mg using laser surface modification and coating processes. Mg is used in orthopedic applications, exhibiting excellent mechanical properties, degradable properties, and biocompatibility. This dissertation comprises three parts.

First, we describe the control of the galvanic corrosion properties of Mg alloys. The treatment with the fs laser resulted in a modified surface microstructure that prevented galvanic corrosion by reducing the potential gap between the secondary phases in the matrix. An exceptionally thin and uniformly refined microstructure is observed, resulting in a reduced corrosion rate.

Second, we developed a quick and simple method to obtain a physically and chemically modified Mg surface with extreme hydrophilic properties to improve the coating ability using an fs laser. The enhanced coating quality leads to increased adhesion strength and minimized

delamination from the substrate, resulting in improved corrosion properties and biocompatibility.

Third, a simple, quick, and one-step coating technology (LISSC) was developed to coat physicochemical hydroxyapatite (HAp) on the surface of Mg in a liquid precursor environment. The laser-treated surface was modified through the nucleation and growth of HAp on the surface of Mg in a short time such that the coating material adhered tightly without pretreatment or chemicals. The enhanced coating ability improved the adhesion strength, which resulted in increased resistance to corrosion and functional properties, such as biocompatibility and rapid coating recovery.

Chapter 2. Control of galvanic corrosion via femtosecond laser surface melting

2.1 Introduction

The recent increase in the aging population and industrialized lifestyle of the general population has increased the occurrence of bone-related disorders and traumas tremendously. The dominant intervention to treat such conditions in the last decade has consisted of the application of inert metallic materials such as titanium alloys (Ti6Al4V), cobalt-chromium-based alloys (Co-Cr), and stainless steel (316L), due to their good mechanical properties and biocompatibility, as well as excellent corrosion resistance [64]. However, due to well-known shortcomings such as medical image distortion, stress shielding, and fatigue fractures, implants made from these inert metals require subsequent surgery to remove them after they have fulfilled their purposes. This subsequent surgery not only puts further stress on the patient but also burdens society by increasing medical costs. To overcome these shortcomings, a significant amount of research on biodegradable metals based on Mg [65, 66], Zn [67-69], and Fe [6, 70] has been performed to develop a new generation of orthopedic and cardiovascular implant devices in the last decade [71, 72].

Among these biodegradable materials, Mg-based alloys have been highlighted in the field as a next-generation biodegradable metallic material. Benefitting from having similar mechanical properties as human bones, Mg is an essential mineral for humans and is involved in many metabolic activities and biological mechanisms. Pure Mg is, however, not suitable for human implantation due to its insufficient strength and rapid corrosion rate in physiological environments [73]. Alloying with Ca [74-76], Al [77], Mn [78, 79], and rare earth (RE) elements [80, 81] is commonly practiced to increase the strength of Mg and overcome such limitations. However, Mg-based alloys are often multi-phased, and differences in chemical potential between such phases cause galvanic corrosion that accelerates the dissolution of the Mg alloys in physiological systems [82]. In addition, rapid corrosion leads to the formation of hydrogen gas and a radical change in pH that could result in severe inflammation or necrosis of tissues. To address these issues, various coating methods utilizing polymers, sol-gel, hydroxyapatite, chemical conversion, electrochemical treatment, and electrodeposition have been employed in the literature [83-87]. Moreover, laser surface modification techniques such as laser cladding [88-91], laser alloying [92], laser peening [93-95], laser texturing [96], and laser surface texturing assisted coating [47, 97] are actively being studied.

Among various laser surface treatments, laser surface melting (LSM) is one of the recently developed manufacturing processes that could

be utilized as a surface modification tool to improve the corrosion properties of Mg alloys [23, 24, 98]. LSM has numerous advantages compared to conventional coating techniques, such as simple production processing without the need for pretreatment, selective irradiation, and an improvement in efficiency. Furthermore, the high melting point of metals enables LSM to provide improved surface properties by rapid solidification, homogenization by the dissolution of the second phases, and refinement of the surface microstructure [20, 99]. Therefore, additional improvement in corrosion resistance may be achieved to overcome issues such as delamination and crack formation on the coating layer, by continuously forming a heat-treated layer of biodegradable metal.

For example, Liu et al. utilized LSM and observed an enhancement in the corrosion properties of the AM60B Mg alloy by grain refinement [26], and Mondal et al. reported improvement of the corrosion and wear resistance of the ACM720 Mg alloy by LSM treatment [100]. Likewise, several publications studied the enhancement of corrosion characteristics using an excimer nanosecond pulsed laser [28, 30-34, 101, 102]. However, the abovementioned conventional laser with a pulse duration longer than a nanosecond is accompanied by a heat-affected zone (HAZ) with a thick molten layer caused by thermal stresses; hence, it is crucial to control the pulse duration and laser beam power during surface modification processes for ideal outcomes [35, 36]. In this respect, femtosecond (fs) lasers have

significant benefits compared to other lasers, since their pulse width is much shorter than the time of thermal diffusion, which leads to a diminished HAZ and fewer pores [103-105].

Recently, our group reported the clinical outcomes when using a new Mg alloy system consisting of 5 wt.% Ca and 1 wt.% Zn (Mg-5wt%Ca-1wt%Zn) minimized the potential gap by doping the Mg₂Ca phase with Zn [106]. Herein, we applied fs LSM and optimized the laser conditions to dramatically increase the overall corrosion resistance of the clinically proven Mg-5wt%Ca-1wt%Zn alloy by decreasing the secondary phase fraction. Additionally, we propose a new approach to improve the initial corrosion rate of Mg alloys by creating a minimally melted, nonporous layer while maintaining the alloy's mechanical properties.

2.2 Experimental Procedures

2.2.1 Preparation of samples

Mg-5wt%Ca-1wt%Zn alloys (5.0 wt.% Ca, 1.0 wt.% Zn, and remaining balance Mg) were prepared using high purity ingots and granules. Casting was carried out in a furnace in an argon atmosphere at approximately 720 °C. The specimens were solidified at room temperature to prepare a billet of size Φ 50 mm \times 60 mm after stirring for 15 min.

Following homogenization by heat treatment, the specimens were extruded at a ratio of 39: 1 to obtain an extruded rod of a diameter of 8 mm. Disk-shaped specimens with a diameter of 8 mm and height of 1 mm were machined. The chemical compositions of the specimens, listed in Table 1, were verified by inductively coupled plasma atomic emission spectroscopy (ICP). Specimens were polished with 2000 grit SiC paper, washed in a sonication bath with 99% ethanol and acetone for 10 min, and finally dried in air for laser treatment. These specimens (approximately 50 in number) were then used for the laser surface modification experiments.

2.2.2 Laser surface modification

All experiments were conducted with a ytterbium fs laser (s-pulse HP, Amplitude, Pessac, France) delivering a 400 fs duration at a wavelength of 343 nm for laser surface modifications. The spot diameter of the laser beam on the surface was 100 μm (Fig. 2.1). The laser pulse energy used was 42 μJ and monitored using a pyroelectric laser energy sensor (Nova 2, OPHIR, Jerusalem, Israel). The energy density was set at 0.535 J/cm^2 and specimens, mounted on an XYZ stage, were scanned at 2 mm/s using a parallel track in an air environment; the spot-to-spot distance was fixed at 100 μm . The pulse repetition frequency (PRF) was varied to 62.5, 125, 250,

500, and 1000 Hz. Three laser treatment conditions were selected, which was followed by a series of experiments (Table. 2).

Table 1. Chemical compositions of the used Mg alloy.

Mg alloy	Ca	Zn	Ni	Mn	Fe	Si	B	Mg
wt %	4.67	1.16	<0.002	<0.001	<0.002	<0.001	<0.002	Bal.

Table 2. Laser processing parameters.

Parameter	Value, Property
Wavelength [nm]	343
Pulse energy [μ J]	42
Pulse duration [fs]	400
Spot diameters [μ m]	120
Repetition rate [Hz]	62.5, 500, 1000
Energy density [J/cm^2]	0.5
Scan speed [mm/s]	2
Spot-to-Spot distance [μ m]	100
Focal length [mm]	40

2.2.3 Analysis of laser-treated surfaces

The topographies of the samples following laser surface modification were characterized by scanning electron microscopy (SEM; Inspect50, FEI, Hillsboro, OR). The effects of laser treatment were analyzed using the back-scattered electron (BSE) detector, followed by a calculation of the area fraction of each phase after LSM using a homemade image processing program. The microstructural characteristics of the melted layers were observed using SEM as well as X-ray diffraction (XRD; D/MAX-2500, Rigaku, Tokyo, Japan). Different phases in samples were identified using XRD with $\text{CuK}\alpha$ radiation. Measurements were conducted in the 2θ range from 10° to 90° with a span of 0.02° and a scan speed of $2^\circ/\text{min}$. Ten samples were fabricated under the same conditions.

Atomic force microscopy (AFM; XE-100, Park system, Korea) scans were performed to observe the roughness. For each specimen, a $30 \times 30 \mu\text{m}^2$ area of samples were recorded using a scan rate of 0.4 Hz in the non-contact mode. The specimens were cleaned with alcohol after the laser treatment and then measured. Two samples were used for each condition and randomly chosen 3 different positions were measured per sample. The roughness value was calculated by averaging the measured AFM data. The

images were then evaluated using a special software package (XEI, Park system, Korea).

The microhardness of each melted surface was measured using a Vickers microhardness tester (Mxt-alpha7, Future-tech corp., Kawasaki, Japan). Three samples were prepared, and the hardness was measured at 3 different positions per sample. A Vickers hardness tester was used to analyze the micro hardness of the surface, which was calculated with a diamond indenter under approximately 1000 gf load. The points taken from a sample were then averaged together, and the standard deviation was calculated.

2.2.4 Corrosion tests

2.2.4.1 Immersion tests

Immersion tests were carried out to measure the evolution of hydrogen gas at 37 °C in Hank's balanced salt solution (HBSS; pH 7.4). To approximate the diuresis process in the human body, a portion of the solution was replaced every 24 h. The hydrogen gas accumulated owing to corrosion of the samples causes the water level to fall over time in a funnel system. The amount of gas is measured by checking the difference in the height of the water over a period of time and converting it to gas volume. After one week of immersion testing, facets of the corroded surfaces and

cross-sections were dried in air and examined with SEM. Under the same conditions mentioned above, 21 specimens were prepared.

2.2.4.2 Electrochemical tests

Electrochemical measurements were used to acquire polarization curves (263A potentiostat/galvanostat, EG&G PAR, Oak Ridge, TN). These electrochemical tests were carried out at 37 °C in a beaker containing HBSS; with Ag/AgCl as the standard reference electrode; a platinum electrode was used as the counter electrode. All samples were stored in a vacuum after laser treatment. The electrochemical test was carried out within 6 h. The working electrode was a specimen with an exposed area of approximately 0.25 cm². Since the magnesium alloy reacts immediately upon contact with the solution because of its rapid reactivity, the corrosion resistance of the magnesium alloy was measured as soon as it was immersed. This method yields the potential and current density where the cathodic and anodic reactions occur at the working electrode. All samples were tested at a scan rate of 0.05 V/s from -2 V to -1 V. The corrosion rate (P_i) of the samples obtained from the corrosion current density was measured according to the following equation: $P_i = 22.85 i_{\text{corr}}$.

Electrochemical impedance spectroscopy (EIS) measurements were done from 1 kHz to 100 MHz frequency range with 10 points per decade

and sinusoidal wave perturbation of 10 mV. The other conditions were kept the same from the experimental measurement of polarization curves.

2.2.5 Cytocompatibility test

The biocompatibility of each sample was evaluated with a CCK-8 kit to measure cell viability. An L929 murine fibrosarcoma cell line was cultured in media in which alloys had been degrading for 1, 3, and 7 days, and the resulting cell densities were measured. The number of live cells was determined by measuring the absorbance of formazan, which is formed during the metabolic processes of live cells. For cell culture, 1X Dulbecco's modified eagle medium without serum was used, and the alloy area exposed to media was 1 cm²/mL. Cell culture was performed at 37 °C and 5% CO₂ to mimic the human physiological environment. This assay was conducted according to ISO 10993.

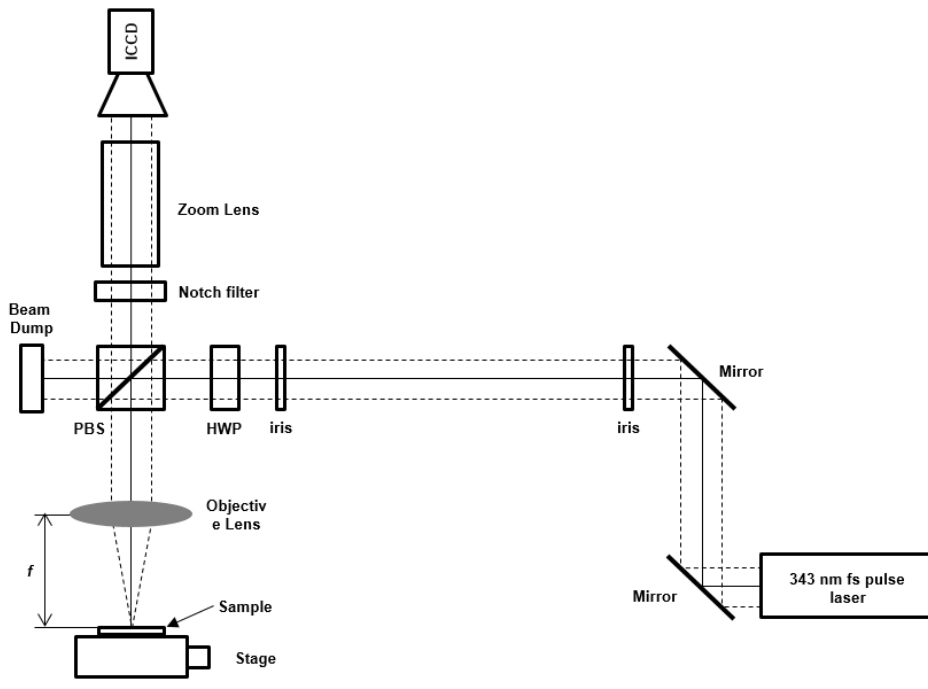


Fig. 2.1 Schematic of laser fs surface treatment experiment setup; fs: femtosecond.

2.3 Results and Discussion

2.3.1 Laser-modified surface morphology

Fig. 2.2 shows the morphologies before and after laser treatment. To analyze the level of solidification, general features of the treated surfaces were examined using the BSE mode in SEM after carving crisscross sections for accurate detection. The average decrease rate of the secondary phase for each condition was calculated in each quadrant area ($200\ \mu\text{m} \times 200\ \mu\text{m}$) and divided by the crisscross pattern. Fig. 2.3a illustrates the decreasing rate of the secondary phase at each condition, analyzed using image processing software; the secondary phases are indicated in blue in Fig. 2.3b; white and gray colored areas indicate Mg_2Ca and the Mg matrix, respectively (Fig. 2.3b). After image processing, the decreasing rates were calculated to be 51.83 ± 4.17 , 63.3 ± 2.27 , 48.36 ± 3.34 , 21.87 ± 2.98 , and $10.66 \pm 2.44\%$ for PRFs of 1000, 500, 250, 125, and 62.5 Hz, respectively. These results show that the greatest decline of the secondary phase in the Mg matrix was present for a PRF of 500 Hz. Indeed, at a PRF of 1000 Hz, the secondary phase fraction in the matrix was higher than for a PRF of 500 Hz. Compared with other conditions, laser-treated specimens at 125 and 62.5 Hz PRF values mostly retained their secondary phase in the matrix. Additional experiments were conducted for three selected samples with

PRFs of 1000, 500, and 62.5 Hz. Fig. 2.3b shows blue regions that indicate the secondary phase locations on the surface of the selected samples both before and after laser treatment.

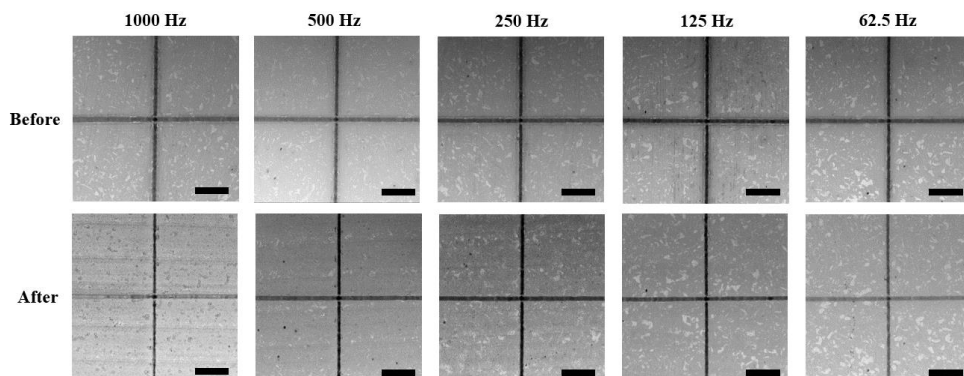


Fig. 2.2 Backscattered electron (BSE) images of specimen surfaces after laser treatment with different repetition rates; scale bar: 100 μm .

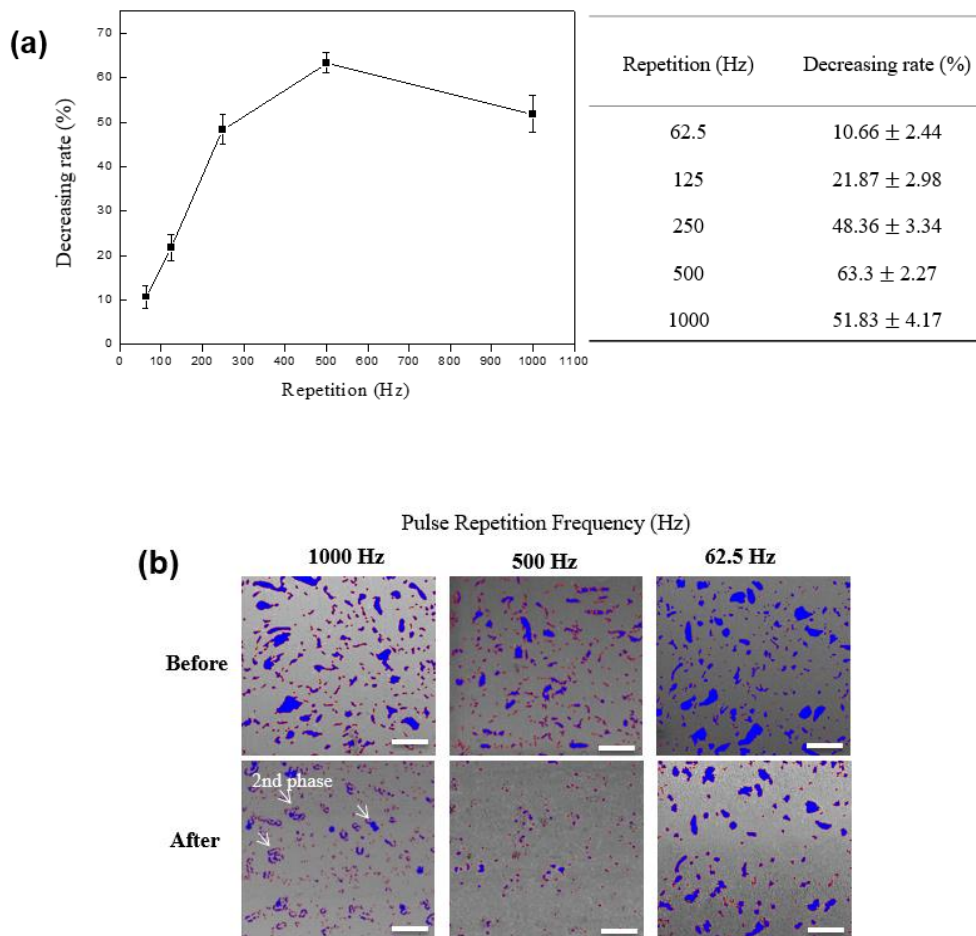


Fig. 2.3 Analysis of the secondary phase decrease rate in the matrix after various pulse repetition frequencies (PRF): (a) decreasing rate of phases and (b) BSE images of surfaces after image processing; scale bar: 50 μm .

Fig. 2.4 shows SEM images of the cross-sections before and after laser treatment with a PRF of 500 Hz. The secondary phase (white color) is located on the edge of the surface, and a melting zone with a depth of ~2-3 μm , created by laser irradiation, can be observed.

In our study, LSM occurred at 0.535 J/cm^2 , similar to previously reported studies that showed surface melting of Mg alloys. Liu et al. [26] demonstrated the effect of LSM conducted at 0.89 J/cm^2 on AM60B alloys, while Wang et al. [97] performed surface melting engineering by irradiation at 0.32, 0.67, and 0.89 J/cm^2 for AZ91D alloys.

Fig. 2.5 shows the change in roughness under different pulse repetition conditions with AFM. The roughness (Ra) values were calculated to be 70.96 ± 13.10 , 91.84 ± 2.01 , 124.21 ± 8.55 , and $321.01 \pm 33.11 \text{ nm}$ for PRFs of as-received, 62.5, 500, and 1000 Hz, respectively. These results show that the formation of such structures increases the roughness of the surface.

Fig. 2.6 shows the elemental composition of a laser-treated surface at 1000 Hz PRF. At a 1000 Hz PRF, the highest power used for surface irradiation in this study, secondary phases, including protruding particles, were observed. These particles were produced by the texturing effect of the fs laser. The formation of microstructures such as ripple shapes and columns was observed on alloy surfaces as the irradiation energy was higher than the threshold. These structures have been reported to be commonly obtained

when utilizing an ultrafast laser [44, 107, 108]. The texturing effect separates the secondary phase from the matrix (yellow arrow in Fig. 2.6); this accelerates galvanic corrosion, resulting in decreased mechanical properties. A PRF of 500 Hz on the surface resulted in secondary phase reduction by 63.3%, which indicates the melting of these phases in the matrix. Although traces of beams were detected at the lowest power level in this study, the secondary phases remained; this implies that the energy level at 62.5 Hz PRF was too low to melt the phases on the surface.

The cause of this change can be interpreted as the temperature rise due to heat accumulation. The heat accumulation equation is expressed as follows.

$$\Delta T = \frac{8 \cdot \eta_{abs} \cdot E_p \cdot \sqrt{f}}{\pi \cdot d^2} \cdot \frac{1}{\rho \cdot c_p \cdot \sqrt{4 \cdot \pi \cdot \kappa}} \cdot (2\sqrt{f \cdot t} - 1.46) \quad (1)$$

where f is the pulse repetition rate, d is the diameter of the laser beam on the surface of the workpiece, and $t > 0$ is the time of the processing. The first term is the heat input, the second term is given by the material properties, and the last term determines the temporal evolution of the temperature increase. The scan speed is 2 mm/s, the size of the beam is 120 μm , and the time to receive energy from the center of the beam is 0.03s. (material properties at 298 K - ρ : density (1.738 g/cm³), C_p : specific heat capacity (0.243cal/g·K), κ : thermal diffusivity (thermal conductivity/ ρC_p), η_{abs} : absorption coefficient (0.9 at 343nm)). The T at 500 Hz PRF where

phase re-dissolution appeared was calculated to be 1063.47 K, which is slightly higher than the melting point of the Mg alloy. The beam energy was calculated by average energy having a gaussian distribution, and it was determined that sufficient melting was conducted on the surface of the Mg alloy. T at 1000 Hz PRF showed 1532.12 K, which has a value exceeding the boiling point in the Mg alloy. This means that ablation could occur rather than melt on the surface. When the Mg matrix and the secondary phase exposed on the surface are compared, the secondary phase was not adequately dissolved and existed on the surface due to the higher burning loss rate of Mg atoms. Similar results were reported in ZK60 alloys, wherein a greater drop in Mg and Zn content was found at slower scanning speeds, with subsequent enrichment of Zr following processing [109].

The thickness of the cross-section at 500 Hz PRF was estimated through the melting area analysis.

$$S = \frac{0.16 \cdot I \cdot \Delta T}{\rho \cdot L_m} \quad (2)$$

where I is the average fluence of the laser beam, and L_m is the latent heat of fusion (84.8 kJ/mol). The thickness of the ablation area is measured by the following equation.

$$Z = \frac{I \Delta t}{\rho(L_m + L_v)} \quad (3)$$

where L_v is the latent heat of vaporization (128 kJ/mol). The calculated value is 451.23 μm (S) and 436.69 μm (Z), respectively. The upper layer of melting is ionized through vaporization, so the remaining area (effective melting depth) after ablation was about 15 μm . Although it did not exactly match the actual measured value, it showed a thickness value of an almost similar cross-section. Assuming that a laser beam with higher energy than the average was irradiated due to the short femtosecond pulse width, more areas are ablated, and the cross-section given in the experimental result may be determined.

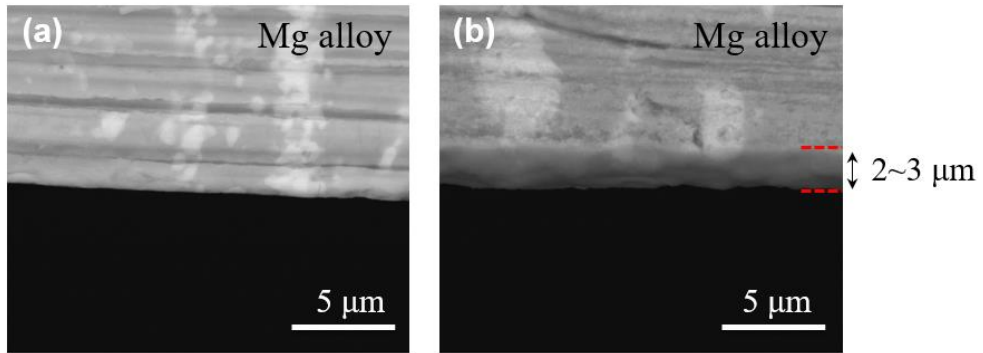


Fig. 2.4 BSE images of cross-sections of: (a) as-received alloy and (b) alloy laser-treated with a 500 Hz pulse repetition frequency (PRF).

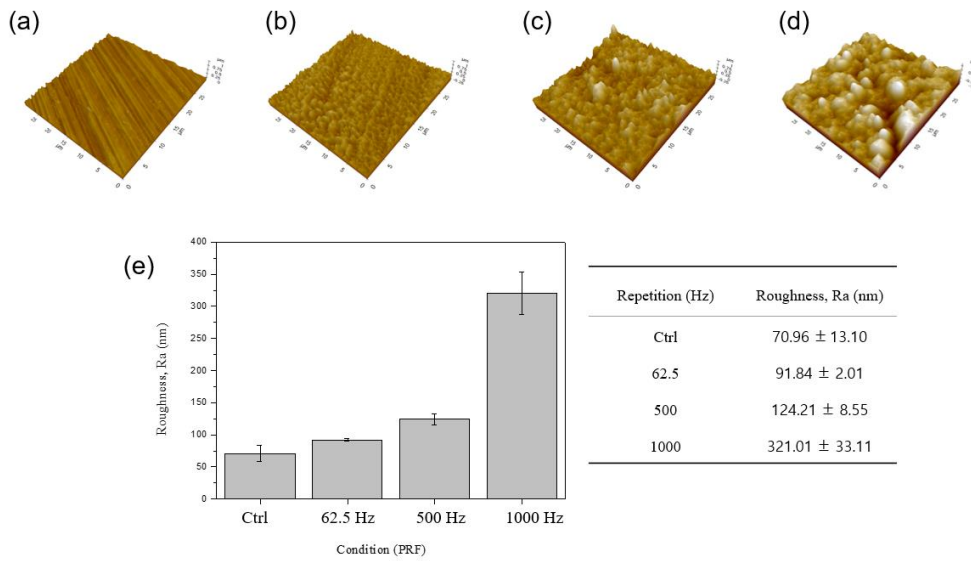
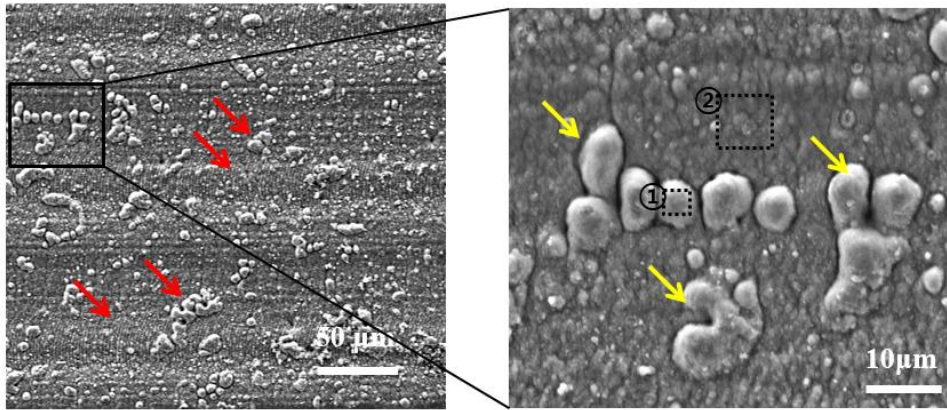


Fig. 2.5 AFM images of the alloy after laser surface melting under different pulse repetition frequencies: (a) polished, (b) 62.5 Hz, (c) 500 Hz, (d) 1000 Hz PRF, (e) Surface roughness plots and values from $30 \times 30 \text{ um}^2$ before and after laser surface treatment.



①

Element	wt.%	at.%
O	10.26	15.71
Zn	03.74	01.40
Mg	76.54	77.11
Ca	09.46	05.78
Matrix	Correction	ZAF

②

Element	wt.%	at.%
O	04.15	06.18
Mg	95.85	93.82
Matrix	Correction	ZAF

Fig. 2.6 Scanning electron microscopy (SEM) image and chemical composition of alloy treated with a 1000 Hz PRF; red arrows indicate ripple shape and columns, yellow arrows indicate secondary phases.

Low angle (2°) XRD of non-treated and laser-treated Mg alloys (62.5, 500, and 1000 Hz PRF) are shown in Fig. 2.7a. XRD peaks for magnesium, magnesium oxide, and the secondary phase were present in all specimens. The spectra of the main peak in each sample, corresponding to α -Mg, are illustrated in Fig. 2.7b. For 62.5 Hz and non-treated samples, similarities were observed in the peaks corresponding to α -Mg. within the 500 and 1000 Hz samples; on the other hand, the diffraction peaks for α -Mg gradually increased when compared to the non-treatment specimen. The diffraction peaks corresponding to Mg_2Ca are shown in Fig. 2.7c. For the 500 Hz sample, this diffraction peak was at the lowest level, suggesting dissolution of this phase by laser melting. For the 1000 Hz sample, on the other hand, the intensity of this peak was at the highest level and its width was increased when compared to the other samples. According to the Scherrer formula, the size of Mg_2Ca was therefore diminished [110].

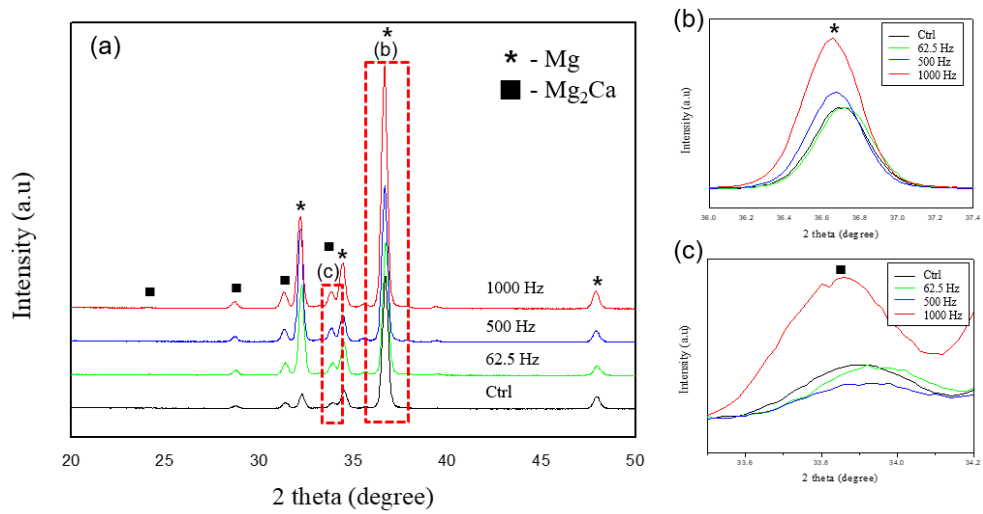


Fig. 2.7 (a) X-ray diffraction (XRD) patterns of as-received (ctrl) and laser-treated alloys; (b) the main peak of Mg matrix enlarged, (c) the main peak of secondary phase enlarged.

2.3.4 Corrosion properties

2.3.4.1 Amount of released hydrogen gas in immersion tests

In general, the volume of released hydrogen gas resulting from the reaction of Mg alloy with a physiological solution increases as time passes. In HBSS, different laser treatments resulted in significantly differing corrosion behaviors (Fig. 2.8). Mg alloy treated with 1000 Hz PRF exhibited the highest level of corrosion compared to those treated under other conditions. Treatment with 62.5 Hz PRF showed a similar volume of hydrogen gas as for no treatment. Meanwhile, 500 Hz PRF resulted in the lowest amount of released hydrogen gas among all conditions. The amount of released hydrogen gas for samples at 500 Hz PRF was 65% lower than for the control group after 180 h of immersion, which reveals that laser treatment with 500 Hz PRF greatly improved the corrosion properties. These results suggest that corrosion was not accelerated in the Mg alloy treated with 500 Hz PRF, owing to the formation of a uniform corrosion layer. However, Mg alloys treated with the other conditions continued to react with the solution rapidly, indicating irregular corrosion layer formation and pitting corrosion. Appropriate laser treatment induces remelting of the secondary phase, reducing the effect of galvanic corrosion caused by the potential gap between the matrix and secondary phase, thereby preventing the occurrence of pitting corrosion and consequently forming a uniform corrosion layer during the corrosion reaction.

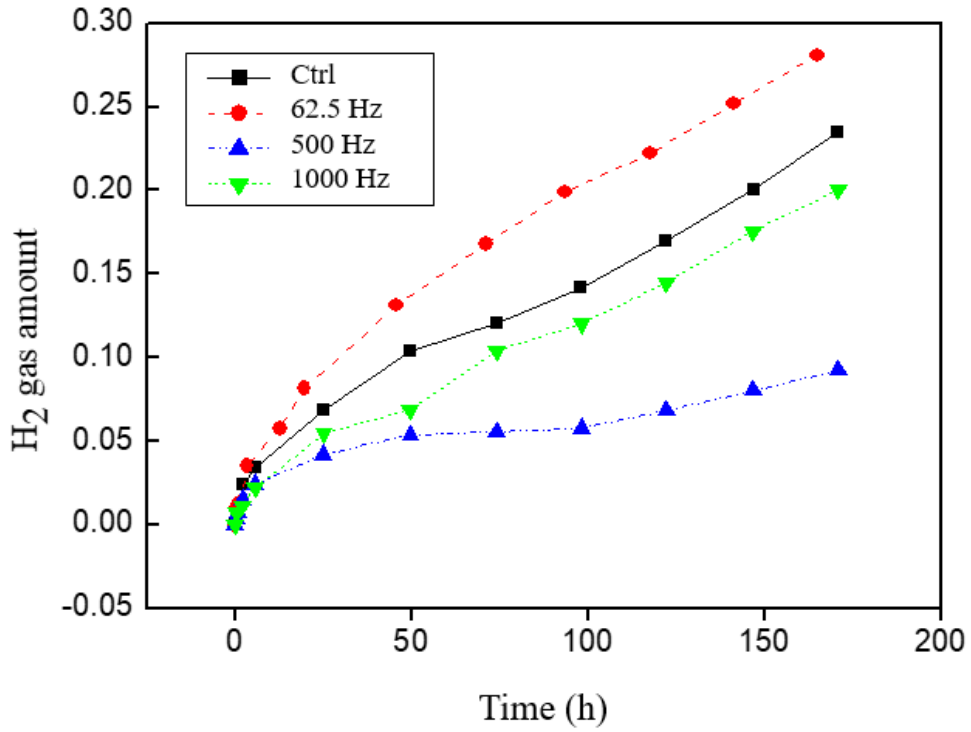


Fig. 2.8 Amount of hydrogen gas released by as-received (Ctrl) and laser-treated specimens in immersion tests.

2.3.4.2 Polarization curves and EIS measurements

Fig. 2.9a shows the corrosion behavior of the samples treated under different conditions as represented by cyclic polarization curves. Table 3 lists the effects of laser surface modification obtained from cyclic polarization testing, including the polarization resistance (R_p), corrosion potential (E_{corr}), current density (I_{corr}), and corrosion rate (P_i) values. In general, a lower I_{corr} and higher E_{corr} indicate improved corrosion resistance. Treatment with 500 Hz PRF showed the highest E_{corr} and lowest I_{corr} , while treatment with 1000 Hz PRF showed a low E_{corr} and the highest I_{corr} . Treatment with 62.5 Hz PRF and no treatment resulted in similar values for both E_{corr} and I_{corr} . The polarization resistance (R_p) also shows the same tendency; it is an indirect indicator of corrosion, and was calculated using the relation:

$$\text{Polarization resistance } (R_p) \quad \left(\frac{\Delta E}{\Delta i} \right) = \frac{\beta_a \beta_c}{2.3 i_{corr} (\beta_a + \beta_c)}$$

where, β_a and β_c , which are the Tafel constants, are slopes of tangents derived from the anodic and cathodic polarization curves, respectively.

Treatment with 500 Hz PRF resulted in the highest polarization resistance, while that with 1000 Hz PRF showed the lowest polarization resistance. These results are in general agreement with those obtained in the HBSS immersion tests.

The corrosion test of laser-treated Mg alloy after exposure in HBSS solution was also investigated with EIS measurements on open circuit potential as shown in Fig. 2.9b. The Nyquist plots contained one capacitive loop. Since the scale of the capacitive loop is related to the polarization resistance, it can be used to measure corrosion resistance. A larger capacitive loop indicates a lower corrosion rate, whereas a smaller diameter of the capacitive loop means a higher corrosion rate. Similar to the result of the polarization test, the capacitive loop at 62.5 Hz PRF is larger than the as-received alloy. At 500 Hz PRF, the largest capacitive loop is observed among the plots, which indicates that corrosion reaction is most effectively suppressed at 500 Hz PRF. At 1000 Hz PRF, the capacitive loop was smaller than that of control indicating accelerated corrosion due to surface modification. This result indicates that the laser treatment at 500 Hz PRF contributes to increasing the polarization resistance due to the suppression of galvanic corrosion.

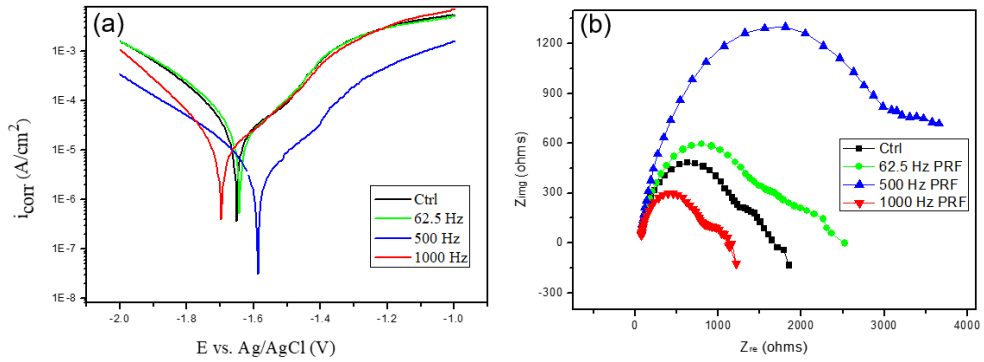


Fig. 2.9 (a) Cyclic polarization curves and (b) EIS measurement for as-received (Ctrl) and laser-treated alloys following immersion in Hank's balanced salt solution (HBSS).

2.3.4.3 Corrosion behavior

The corrosion behavior was observed with SEM images obtained following the immersion tests. Fig. 2.10 shows the surfaces of the Mg-based alloy after immersion testing in HBSS. The red dashed circles indicate where pitting occurred on the surfaces. Local pitting corrosion was particularly evident on the surface treated with 1000 Hz PRF, while it was not seen on the surface treated with 500 Hz PRF. Furthermore, after 3 h of immersion, the corrosion layer had formed a uniform corrosion by-product layer in the sample surface treated with 500 Hz PRF. In contrast, local pitting corrosion sites and irregular corrosion by-products formed under other conditions. There was a definite difference in corrosion behavior after 24 h of immersion. The corrosion layers were irregular, and greater amounts of corrosion products were created, in the control, 1000 Hz PRF, and 62.5 Hz PRF samples. However, the corrosion layer was homogeneous in the 500 Hz PRF sample.

The corrosion behavior was further analyzed by observing the cross-sections of the specimens. Pitting and intergranular corrosion were observed in the control, 1000 Hz PRF, and 62.5 Hz PRF samples, but not in the 500 Hz PRF sample, after 1 week of immersion (Fig. 2.11). These

results indicate that uniform corrosion occurred by irradiation with laser pulses using a PRF of 500 Hz.

In short, a decreasing secondary phase fraction impeded galvanic corrosion so that overall corrosion properties were improved. The corrosion behavior observed for the highest power level in this study, 1000 Hz PRF, indicated rapid corrosion. This result may be due to the increase of textured structures in the surface area as a result of laser treatment, which leads to volume expansion and an increase in surface roughness. The lowest power in this study, 62.5 Hz PRF, resulted in a corrosion behavior similar to the control group in immersion tests because the power of the laser pulses was not high enough to melt the surface.

The 500 Hz PRF improved corrosion properties due to remelting of the secondary phases on the surface, causing inhibition of galvanic corrosion. This result is supported by the immersion test and observed corrosion behavior. In the polarization curves, the 500 Hz PRF condition showed the lowest I_{corr} and highest E_{corr} among all conditions, which implies that the laser treatment improved corrosion resistance. In addition, SEM images of corroded samples reveal boundary interfaces between the laser-treated and non-treated areas (Fig. 2.12); the polished region on the right side of the surface shows pitting corrosion. These images also reveal that the corrosion properties were drastically improved by laser treatment.

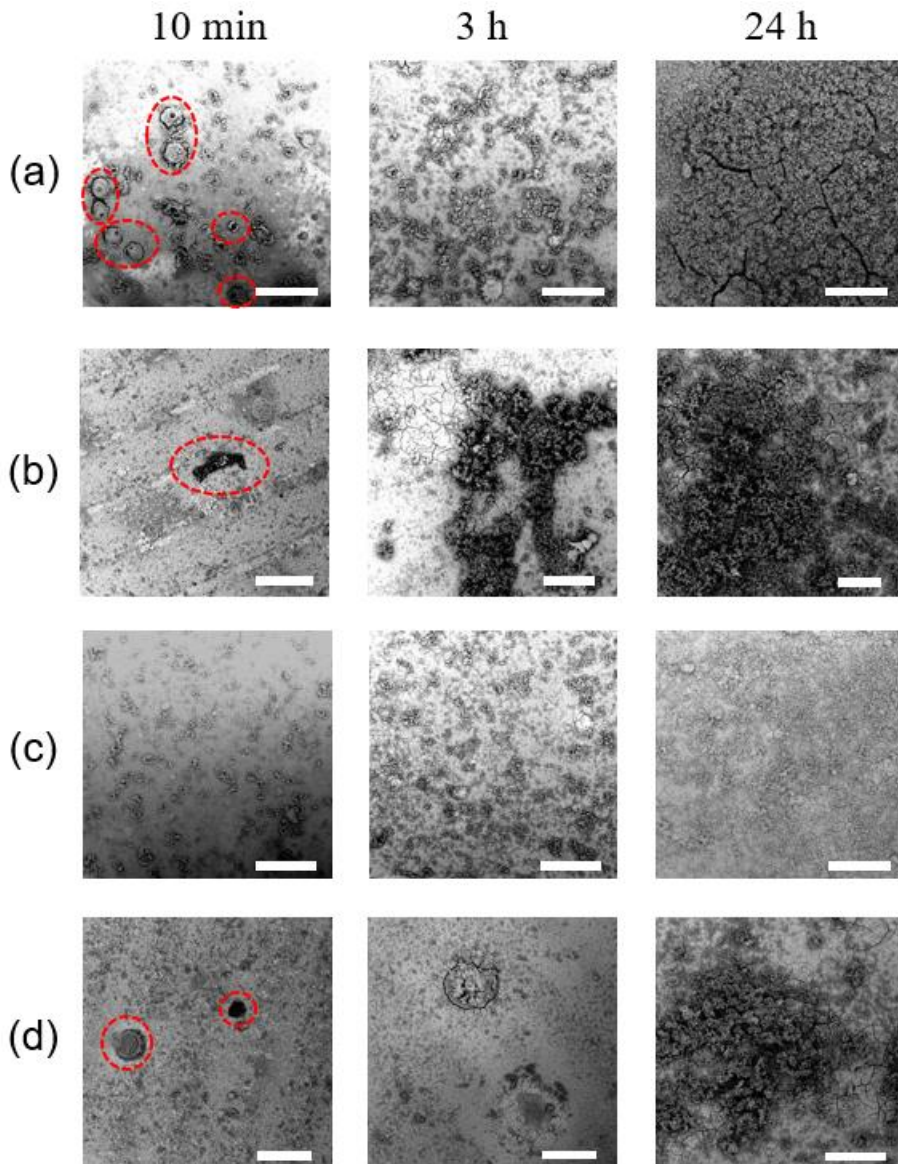


Fig. 2.10 SEM images of surface morphologies of the as-received and laser-treated alloys with different pulse repetition frequencies: (a) as-received, (b) 1000 Hz, (c) 500 Hz, (d) 62.5 Hz PRF; scale bar: 100 μm .

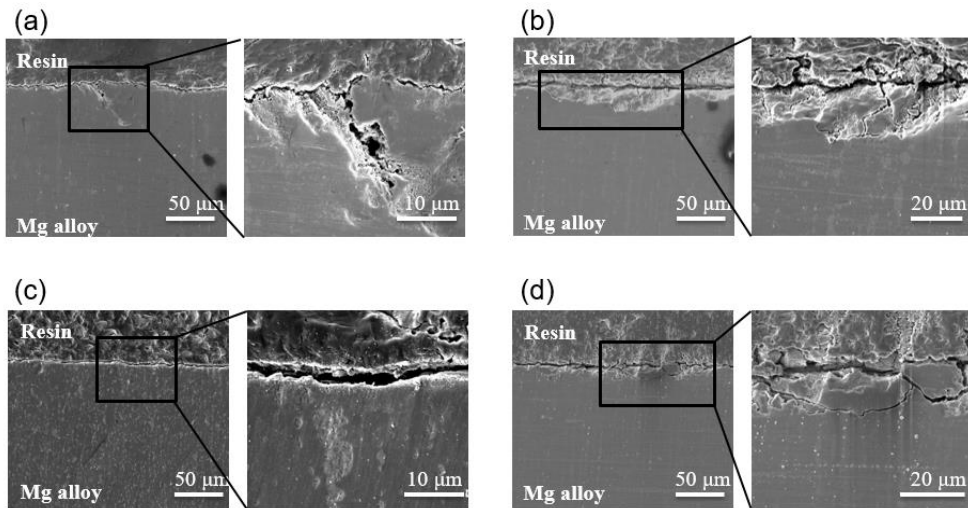


Fig. 2.11 SEM images of cross-sections of samples after immersion in HBSS for 1 week: (a) as-received sample, and after (b) 1000 Hz, (c) 500 Hz, and (d) 62.5 Hz PRF.

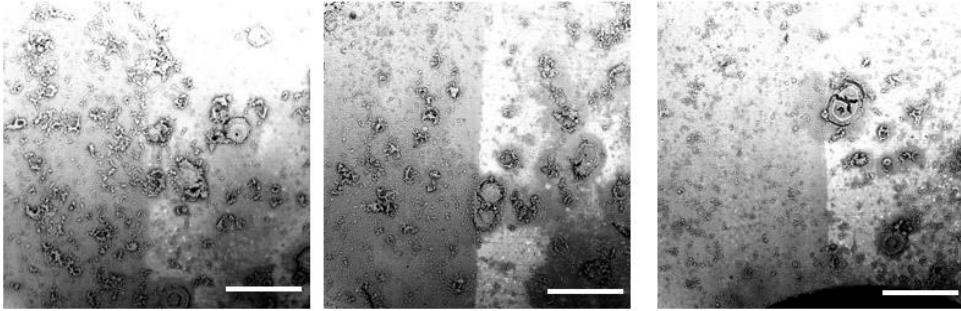


Fig. 2.12 BSE images of the boundaries between the as-received and laser-treated surface at three different positions with 500 Hz PRF after immersion in HBSS for 10 min (left region: laser-treated surface; right region: as-received surface); scale bar: 100 μm .

2.3.6 Hardness

Compared to conventional laser treatment, the mechanical properties of Mg alloys were expected to remain the same after fs laser treatment, since the laser only affects a layer of 2-3 μm thick (see also Fig. 4). The hardness of the control Mg-based alloys was 83.56 ± 1.67 HV, while that of samples treated with 500 Hz PRF was 83.18 ± 1.84 HV (Fig. 2.13). This result confirms that the mechanical properties of the Mg alloys were maintained after laser treatment.

2.3.7 Cell viability

While laser treatment modifies the corrosion properties and retains the mechanical properties of Mg-based alloys, biocompatibility is crucial for these alloys to be utilized as a biomaterial. The formazan-based assay, as stipulated by ISO 10993, showed over 80% cell viability on days 1, 3, and 7 (Fig. 2.14).

The uniform initial corrosion reaction induced proper formation of the corrosion layer, and there was no significant change in pH on the Mg alloy treated with 500 Hz PRF. The corrosion layers formed under other conditions did not have an environment conducive to the viability of cells, owing to the continuous progress of corrosion.

The Mg alloy exhibited the lowest cell viability at 1 day due to its rapid initial corrosion until the formation of the corrosion layer, and it can be seen that a stable environment was created after 3 days. The cell viability showed a slight decrease on day 7 compared to day 3, indicating the continuation of corrosion.

When assessing toxicity, samples that exhibited cell viability higher than 80% were considered nontoxic. Nonetheless, among the various samples, the Mg alloy treated with 500 Hz PRF exhibited the highest level of cell viability. Therefore, we conclude that cell viability can be increased via laser treatment under proper conditions.

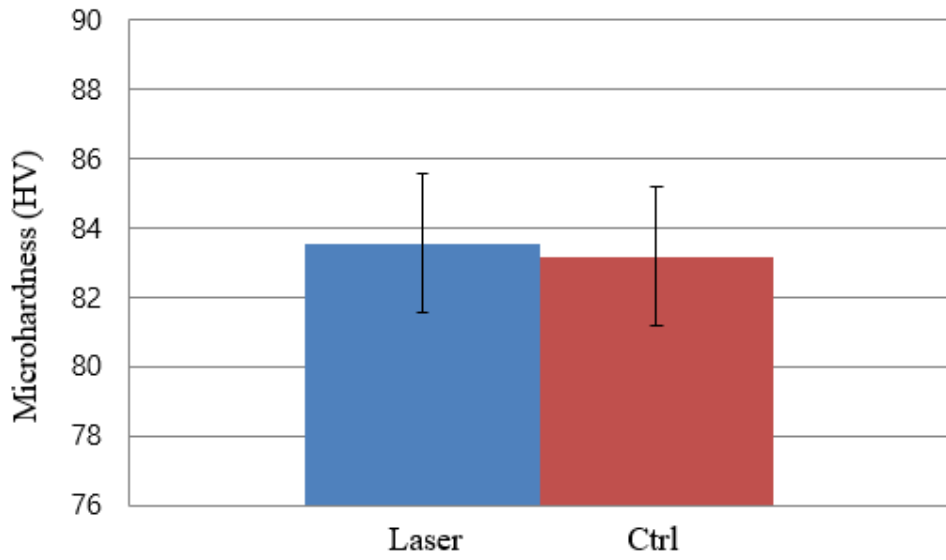


Fig. 2.13 Microhardness values for the top surfaces of as-received and 500 Hz PRF laser-treated samples.

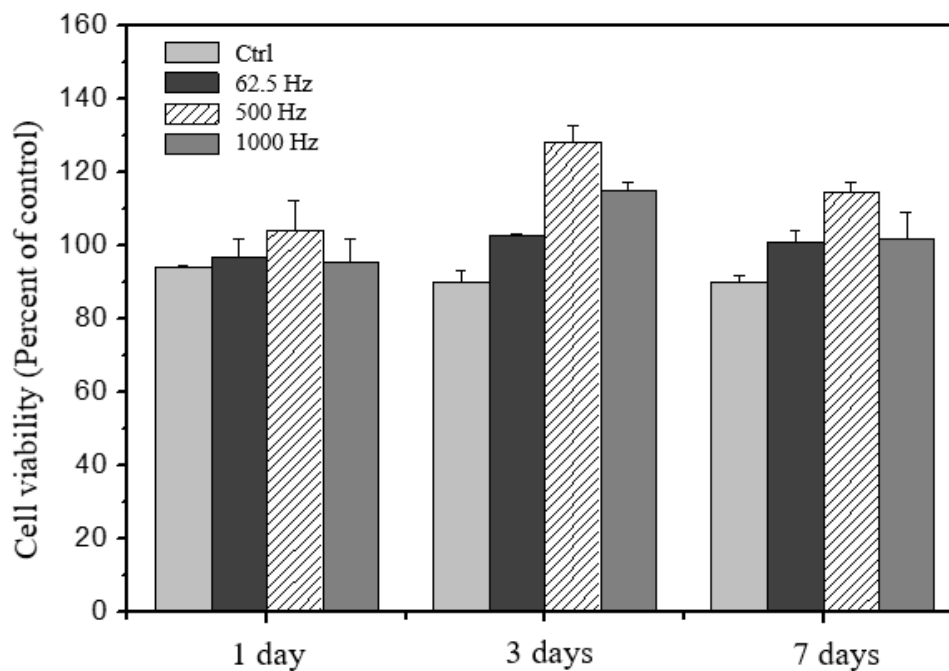


Fig. 2.14 Cell viability of as-received and laser-treated Mg alloys using various PRFs after immersion testing in Dulbecco's modified eagle medium for 1, 3, and 7 days.

2.4 Conclusion

In this study, the corrosion properties of clinically proven Mg-Ca-Zn alloys were modified using fs laser surface treatment. The treatment of the fs laser resulted in a modified surface microstructure that prevented galvanic corrosion by reducing the potential gap between the secondary phase in the matrix. The exceptionally thin and uniformly refined microstructure was observed, resulting in a reduced corrosion rate when treated with optimal laser energy of 500 Hz. Furthermore, the mechanical properties and biocompatibility of the Mg-Ca-Zn alloys were maintained after the surface treatment. The findings of this study may be applicable in a wide range of biomedical applications of biodegradable metals such as cardiovascular stents, orthopedic plates, and bone screws.

Chapter 3. Enhancement of coating ability physically and chemically via fs laser textured surface

3.1 Introduction

The application of Mg-based biodegradable metal has been used in orthopedic implantable devices such as bone screws, ligament screw plates, and porous scaffolds [111, 112]. The primary obstacle in developing such devices is directly related to the corrosion rate of Mg in body fluids. Mg corrosion in body fluids is accompanied by the generation of hydrogen gas and an increase of local pH from concentrated hydroxide ions, which, if not controlled, form a gas pocket that causes tissue necrosis and ultimately implant failure. One of the most commonly practiced methods to control the corrosion rate of Mg involves polymer coating of the metallic surface [8, 106, 113-115].

Biodegradable polymer coatings, such as poly-caprolactone, poly(lactic-co-glycolic acid) (PLGA), and poly(lactic acid), on Mg alloys, have shown effective prevention of early corrosion. They are often used as vehicles for selective loading of drugs to further enhance the benefits of implantable devices [116-119]. However, there are several known issues such as the delamination of polymer layers and pitting of the polymer coating, which often results in faster corrosion of the Mg alloy and potential

blockage of blood flow by large polymer film debris. Therefore, high interfacial adhesion strength with the metal surface is required for the effective utilization of the polymer as a coating material. Pretreatment processes such as plasma treatment and chemical oxidation have been developed to improve the adhesion strength of polymers on metal surfaces and stabilize the coating layer but they are still considered insufficient and in some cases, not biocompatible [120-123].

Recently, laser surface treatment has attracted considerable research interest and has been developed as a powerful tool to modify the surface properties of target materials. The laser surface modification allows for simple non-contact manufacturing, selective irradiation, and cost-effective, and maskless single-step processes in an ambient air environment without vacuum [124]. Therefore, the various approach can be applied through adjustment of the laser power/pulse energy. Typically, the corrosion resistance of the magnesium alloy can be improved through laser surface remelting and laser cladding techniques through the distribution of refined intermetallic compounds or the formation of an oxidation/passivation layer on the surface [125-129].

In particular, the laser surface texturing method using a femtosecond (fs) laser has been investigated in detail owing to the easy formation of micro-, nano-, and hierarchical structures on the material surface, which lead to changes in surface properties such as surface

roughness and surface energy. Furthermore, thermal stress and damage to the substrate can be minimized because the fs laser applies energy in a substantially shorter time than the pulse duration of a conventional laser. fs laser energy is deposited on the target substrate without interaction between the laser and plasma, resulting in alteration of the surface structure and chemical (oxidation, hydrophilic, and hydrophobic) properties [44, 47, 96, 130, 131]. In our previous work, we reported the utilization of fs laser to create a thin uniformly refined layer on top of an Mg-based alloy surface to reduce the corrosion rate from galvanic and pitting corrosion [32]. This method allowed the reduction of secondary phase fraction while retaining mechanical properties and biocompatibility.

Herein, the surface of Mg was modified with an fs laser to obtain a more stable and stronger polymer adhesion force between the coating interface. The drastic increase in surface adhesion strength and improvement of polymer coating ability was induced by the formation of micro pits, groove patterns, and oxidized nanostructures on the Mg surface. Optimized fs laser treatment condition revealed the mechanism by which the surface adhesion to polymer is improved both physically and chemically.

3.2 Experimental Procedures

3.2.1. Preparation of treated Mg

Pure Mg (99.9% purity) with a cylindrical shape, 8 mm diameter, and 1 mm thickness, was prepared. The chemical compositions of pure Mg were verified by inductively coupled plasma atomic emission spectroscopy. Samples were polished with a 2000 grit SiC paper to remove pollution and obtain a smooth surface before laser treatment. Thereafter, samples were sequentially cleaned using a sonicator (SD-300H, Mujigae, Korea) in 99% ethanol and acetone for 10 min each, and air-dried.

3.2.2. Laser process for fs laser textured surface and coating process

The laser used herein was a ytterbium femtosecond (fs) laser (s-Pulse HP, Amplitude, France). The laser system is capable of providing a beam with a pulsed width of 400 fs at a central wavelength of 343 nm, as shown in Fig. 1b. The repetition rate was fixed at 1 kHz. The spot diameter of the laser beam on the surface was approximately 120 μm . All samples were mounted on an XYZ stage that was translated at 0.5 mm/s in grating tracks to induce isotropic wetting behavior. A variety of textured surfaces were formed, not only by altering the laser energy but also by the diverse interval gap of the laser tracks. To produce different textured surfaces on

pure Mg, the pulse energy was varied with 80, 120, and 160 μJ , measured by a power detector (Nova 2, OPHIR). This indicated that the laser energy fluence (F) was 1.0, 1.5, and 2.0 J/cm^2 , respectively.

PLGA was spin-coated on textured Mg by laser modification and polished Mg. PLGA (LG857S, Resomer®) was dissolved in 2,2,2-trifluoroethanol with 11% (w/w) concentration. Generally, the thickness of the coating layer became thicker as the PLGA concentration increased [132]. In this study, the concentration of PLGA was selected as a condition that can serve as a barrier layer by spreading it evenly on the substrate with a constant thickness. The PLGA solution was spin-coated on polished Mg and fs laser-treated Mg, respectively, for 40 s at 2000 rpm. PLGA-coated Mg was dried in a vacuum overnight at 24 °C for further characterization. All processes in this study are shown in Fig. 3.1.

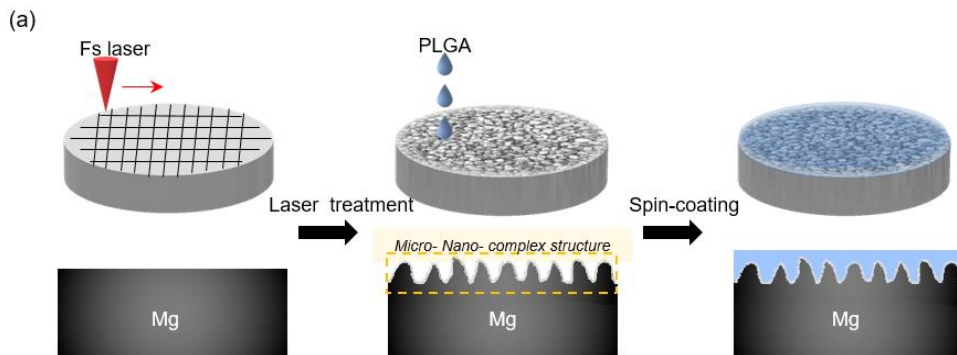


Fig. 3.1 Schematic graphical illustration of PLGA coating on treated Mg surface after formation of hierarchical topography via fs laser.

3.2.2. Physicochemical characterization

The surface was characterized via scanning electron microscopy (SEM; Inspect F50, FEI, USA). X-ray diffractometry (XRD; D/MAX-2500, Rigaku, Japan) with $\text{CuK}\alpha$ radiation was used to obtain crystal orientation of microstructural characteristics of specimens. The 3D structures and surface roughness of samples were analyzed using a confocal laser scanning microscope (LSM; LEXT OLS4100, Olympus, Japan). To measure surface wettability change of laser-treated Mg, contact angle measurement (SmartDrop, Femtobiomed, Korea) was performed by dropping 1 μL of deionized water. Elemental distributions and images were simultaneously captured using a scanning transmission electron microscope (STEM; FEI Talos F200X, USA) equipped with a Super-X energy-dispersive X-ray spectroscopy (EDS) detector.

3.2.3. Evaluation of corrosion properties

3.2.3.1. Hydrogen gas release tests

The corrosion property was evaluated by measuring the amount of generated hydrogen gas because it shows the degree of corrosion resistance of the samples [133, 134]. All samples exposed to 8Φ were immersed at

37 °C in Hank's balanced salt solution of 200 ml (HBSS; pH 7.4, Welgene, Korea). The evolution of hydrogen gas from samples was collected at the top of a beaker. A portion of Hank's solution was replaced every 24 h due to consideration of the diuresis process in the body.

3.2.3.2. Mg ion release tests

To quantify Mg ions, PLGA-coated and non-coated Mg substrates were immersed in serum-free 1 × Dulbecco's modified Eagle's medium (DMEM) in the ratio of exposed Mg area of 1 cm²/mL of media. Mg in media was incubated at 37 °C and 5% CO₂ to mimic the human environment. A portion of media was removed at 1, 3, and 7 d, and Mg ions were assayed using a Quantichrom Metal Ion Assay Kit series (DIMG-250, Bioassay Systems, USA) [135, 136].

3.2.4. Adhesion strength

Tensile tests were performed to measure the adhesion strength between the coating layer and textured surface. The tensile force tester (Instron 5966, Instron Engineering Corporation, USA) was used at a speed of 1 mm/min. On the cylindrical sample, the bottom was non-treated, and the top was area coated with polymer. The sample was held using highly adhesive glue (Loctite 401, Henkel) on both the bottom and top surfaces.

The adhesion strength was measured at the point where the coating was detached from the substrate.

3.2.5. Cytocompatibility test

To evaluate cell viability, cells were prepared as follows: L929 cells (NCTC clone 929, Korean cell line bank, Korea) were seeded 7×10^3 cells/well on an Mg substrate (Ctrl, PLGA@Bare, PLGA@FsMg) for 1 d in serum-supplemented DMEM, and incubated overnight at 37°C and 5% CO₂ for cell adhesion. Thereafter, the medium was changed to serum-free DMEM and incubated for 1, 3, and 7 d. Cells were further incubated for 24 h, and their viability was measured using the Cell Counting Kit-8 assay. This assay was conducted according to ISO 10993. For cell morphology observation, cells were pre-incubated at 37°C and 5% CO₂ on an Mg substrate overnight in serum-supplemented media, which was changed to an Mg ion-containing broth from day 3, and further incubated for 24 h. Thereafter, cells on the Mg substrate were fixed with ice-cold methanol to dehydrate, and observed by SEM.

3.3 Results and Discussion

3.3.1. Surface analysis after laser surface modification

The surface treatment of Mg substrates was performed by fs laser under various conditions listed in Table 3. The change of surface morphology characteristics following fs laser treatment is shown in Fig. 3.2. It appeared noticeably rough as the laser intensity increased in the range of 1.0–2.0. J/cm². As the shapes became noticeably rougher, they were formed into distinguishably flat (as-polished), embossed (pulse energy: 80 μJ), bump (120 μJ), or canyon (160 μJ)-like shapes, as shown in Fig. 3.2a-d. These surface features were scanned and imaged in three dimensions using LSM analysis, as shown in Fig. 3.2e-h. As the intensity of the laser increased, the surface characteristics that became rough corresponded to the results from the SEM analysis. In particular, an increase in roughness indicates an increase in the surface area of the Mg substrate, which affects surface wetting properties [36, 37].

In this laser condition, a higher density was applied than in the laser condition. Similarly, when the heat accumulation temperature is calculated using equation (1), 2436.3 K is a value that surpasses the boiling point of Mg in the canyon condition having the highest energy density in this study. As a result, ablation and evaporation of Mg could be conducted resulting in

the formation of microstructures and increasing roughness. Once micro-nano roughness emerged, the laser beam could be easily reflected and scattered back onto the surface by projecting structures. The laser irradiation was prone to be effectively trapped in fissures and holes when repeated reflections increase the coupling with the material. Multiple internal reflections could lead the laser beam into the bulk within these protruded structures. Refraction at the surface of these structures also caused transmission at oblique angles, substantially lengthening the optical path and boosting absorption. The degree of amplification was determined by the geometry and size of the surface characteristics.

Fig. 3.2i shows the wettability of each sample treated with an fs laser. The contact angle with water decreased sharply from 75.6° (as-polished) to 5.3° (canyon-like) according to the changed surface roughness. The wettability increased as the absolute value of the water contact angle decreased. Similar results have been reported as a phenomenon that occurs due to the change in wettability of the metal surface from the laser treatment, and it can be used as a controlled method for surface structure modification by the laser to obtain an ultra-small hydrophilic surface [38-40]. As laser intensity increased, surface oxide content increased, as shown in Fig. 3.2j. It was confirmed that the hydrophilic property was maintained for up to approximately 3 weeks in the canyon-like structure. In short, a super-hydrophilic substrate-surface structure was formed through fs laser surface

treatment, and a canyon-like structured surface sample with the lowest water contact angle among the treatment conditions is expected to show the most promising performance for adhesion of the polymer coating. The laser treatment and coating were fixed under these conditions to conduct the experiments that followed.

In general, laser surface treatment has been known to promote the oxidation reaction of Mg to oxides such as MgO or Mg(OH)₂ on the surface [41-44]. XRD analysis was performed to observe the phase change by fs-laser treatment, as shown in Fig. 3.2k. Following fs-laser treatment, major peaks of MgO appeared at 42.8° and 62°, which were relatively wide and had low strength. It was clearly distinguishable when compared to the clear and sharp shape peaks of the Mg substrate. This was indirect evidence of the formation of nanocrystalline MgO. By the crystallographic features, extremely nanoporous structures (in set in Fig. 3.2d) were observed on the sample surface with canyon-like structures. The formation of this unusual surface structure can be explained by the nanoscale Kirkendall diffusion effect [45-47]. The thermal energy obtained from the local energy of the fs-Laser appeared to lead to the diffusion of Mg atoms. It does not appear to undergo an oxidation reaction where the oxygen source obtained from the atmosphere penetrates the bulk. Instead, the nanoporous unique surface structure was formed by the nanoscale Kirkendall effect, where

simultaneous diffusion of Mg atoms to the surface occurred with a reaction with oxygen.

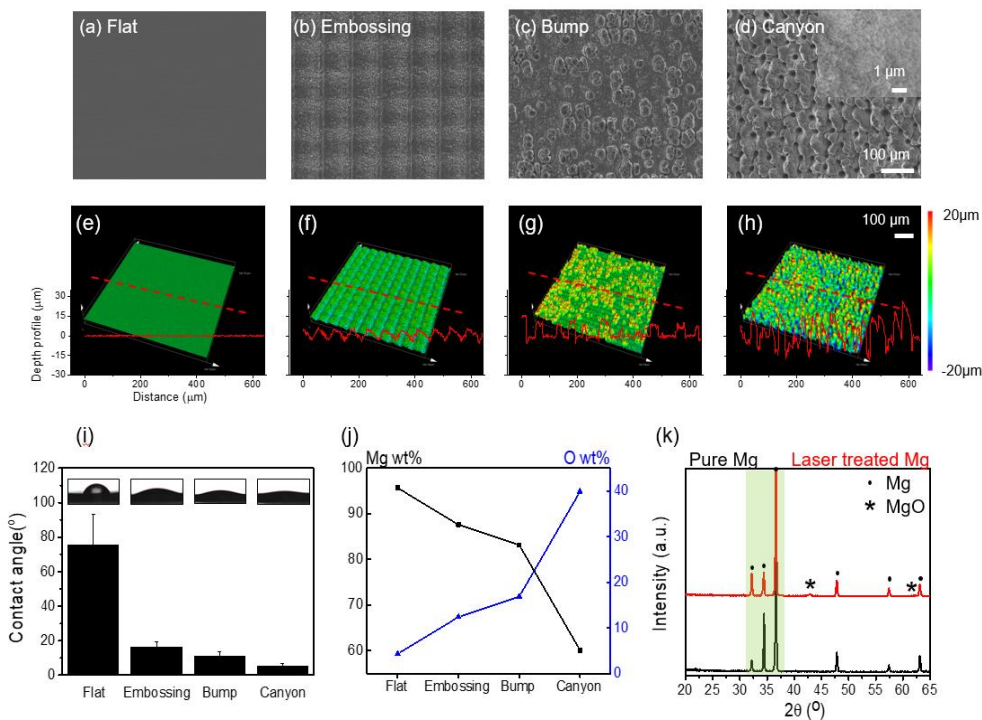


Fig. 3.2 Characteristics of treated Mg treated by fs laser: (a-d) SEM surface images of the morphology of Mg substrate and (e-h) 3D topography images and depth profile according to each laser parameter. (i) The mean contact angle of laser-treated Mg surface. (j) Weight percent (wt.%) change of Mg (black square) and oxygen (blue triangle) of each laser condition. (k) XRD patterns of as-received (black line; bare) and laser-treated alloy (red line; Canyon).

The results of TEM-EDS analysis clearly showed that the abovementioned nanoporous surface was composed of MgO (Fig. 3.3). The cross-sectional image that was analyzed in greater detail via TEM clearly showed different boundaries separating the Mg substrate and the oxidized nanoporous-structured MgO region. Selected area (electron) diffraction pattern analysis was conducted to investigate and confirm the difference in the crystal properties of the boundaries (Fig. 3.3e-h). The MgO region close to the surface showed ring pattern (polycrystalline) properties with values of d-spacing as 2.15 Å, 1.515 Å, and 1.21 Å which correspond to (200), (220), and (311) of MgO (JCPDS 89-7746), respectively. Additionally, high resolution-TEM image analysis verified this region to be polycrystalline (Fig. 3.3j). Respective d-spacing signals were simultaneously observed as red circles (g) in Fig. 3e, which corresponds to the interface between the Mg substrate and MgO (Fig. 3.5g). The Mg substrate region marked with the red circles (h) showed d-spacing values of 2.48, 1.61, and 1.89, corresponding to the (101), (102), and (110) planes of Mg, respectively, which were consistent with the XRD results (JCPDS 04-0770).

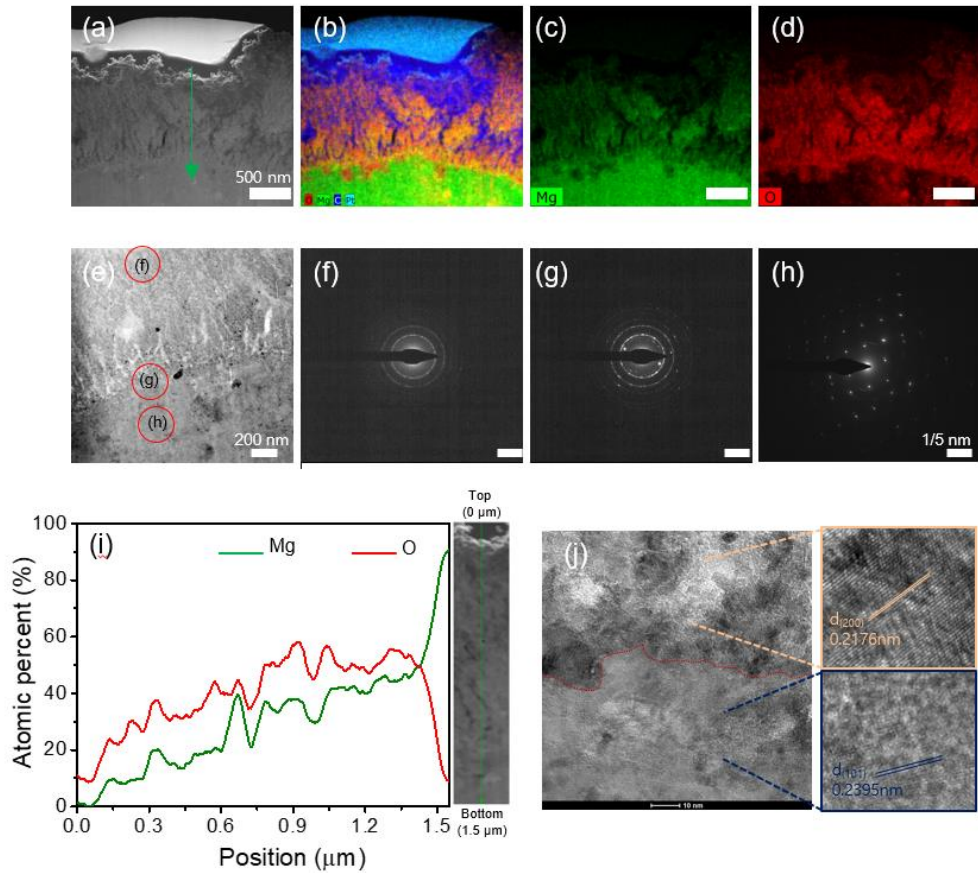


Fig. 3.3 (a-d) TEM-EDS of cross-section mapping on Canyon surface, (e-h) SAED pattern of the boundary of MgO between Mg. (i) EDAX line profile from the surface to bottom. (j) HR investigation at the boundary of MgO between Mg.

3.3.2. PLGA coating on Fs laser-treated Mg

Fs laser-treated Mg was spin-coated with PLGA and coating layer stability was evaluated (Fig. 3.4). The cross-section image of PLGA coated on fs laser-treated Mg (PLGA@FsMg) and PLGA coated on bare Mg (PLGA@Bare) is shown in Fig. 4a. PLGA layers were well coated on the Mg surface, with PLGA layers completely filled on groove areas of PLGA@FsMg. The average thickness of the PLGA coating from the bottom was $64.21 \pm 2.3 \mu\text{m}$ and $52.1 \pm 6.51 \mu\text{m}$ for PLGA@Bare and PLGA@FsMg, respectively. As confirmed in Fig. 3.2, super-hydrophilic properties of fs laser-treated surface will create a strong bond with the PLGA coating as the solvent for PLGA dissolution is water-miscible. This coincides with Wenzel's model that supports liquid spreading on a super-hydrophilic surface with roughness [137, 138]. Hydrophilic properties provide a favorable surface for polymer deposition because coating materials are quickly and widely spread on textured metal surfaces, influencing good adhesion [47, 139].

As the laser-treated Mg surface became rough, the polymer adhesion force on the surface was measured, as shown in Fig. 3.4b. The result showed that PLGA@FsMg endured $382.84 \pm 73.14 \text{ N}$ of load, which was 77% higher adhesion strength than PLGA@Bare with $215.91 \pm 51.98 \text{ N}$ of load. A rough surface structure by laser treatment appears to hook onto

the polymer coating layers, influencing the strong adhesion force. A similar effect was observed with plasma treatment on Mg, and surface-coated PLGA layers were strongly bound [123, 140, 141]. In addition, the bonding force with the polymer layer became more stable as the oxide surface area increased [139, 142]. These results indicate that oxide nanostructures produced by fs lasers improved coating ability. Protein absorption also shows a similar trend and the elongated shape of fibrinogen absorption was improved on a nano-rough surface rather than on a globular shape of bovine serum albumin [143]. Therefore, fs laser-treated surface which adds hooking layers on the surface could provide improved adhesion strength while promoting the favorable cellular reaction.

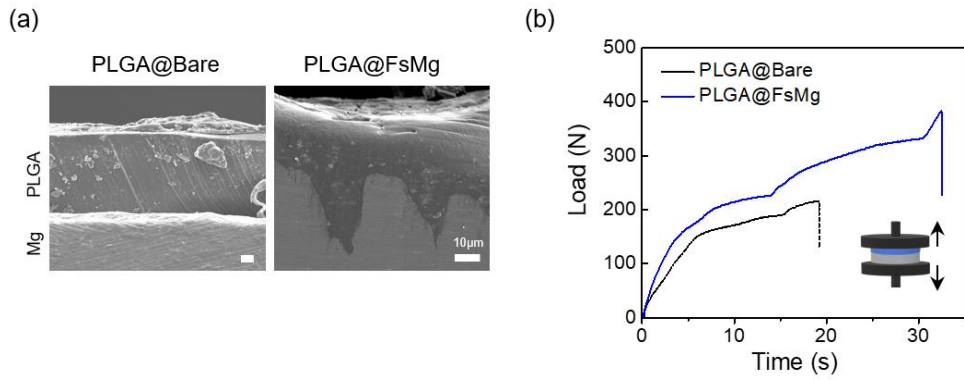


Fig. 3.4 (a) SEM images of the cross-section of samples after spin-coating; PLGA@Bare (left) and PLGA@FsMg (right). (b) Adhesion strength curve between PLGA coating layer between Mg substrates.

3.3.3. Corrosion property

PLGA-coated Mg was immersed in Hank's solution and tested for corrosion, as shown in Fig. 3.5a. Coating of PLGA on Mg delayed the initial corrosion and release of hydrogen gas for the first 3 d in comparison to that of bare Mg. Thereafter, PLGA@Bare abruptly released hydrogen gas, and only PLGA@FsMg maintained stable hydrogen gas release (Fig. 3.5a). The PLGA coating layer of PLGA@Bare was damaged such that Mg was exposed to the stimulated body fluid resulting in rapid pitting corrosion. However, PLGA layers on PLGA@FsMg were stable up to 162 h. The anti-corrosion effect of the PLGA coating was also confirmed by the Mg ion concentration profile in Fig. 3.5b. Similar to the hydrogen gas release profile, PLGA@FsMg showed effective Mg ion release control to a concentration of 15.7 mM in comparison to PLGA@Bare and Bare Mg with 32.6 and 40.8 mM, respectively. Additionally, the Mg ion concentration of PLGA@FsMg between days 3 to 7 showed increasing at decreasing rate. In contrast, the Mg ion concentration of PLGA@Bare and Ctrl was increased at an increasing rate. PLGA-coated samples were removed and the consistency of the coating layer was observed after the corrosion test. PLGA@Bare demonstrated that the whole coating layer was delaminated from Mg. In contrast, PLGA@FsMg showed slight damage to the coating layer at the edge of the Mg substrate, as shown in Fig. 3.5c. The cross-

sectional morphology of the corroded Mg sample observed by focused ion beam-SEM is shown in Fig. 3.5d. There was no coating layer in the specimens for the control group as it had peeled off from the substrate. In contrast, the coating layer, which was still attached to the surfaces of the laser-treated Mg after the corrosion test, was confirmed by SEM imaging.

In addition, PLGA is considered semi-permeable to the solution, which would occur a corrosion reaction between the coating layer and the Mg substrate. If the substrate shows low corrosion resistance, the chemical reaction progresses leading to delamination due to the evolution of hydrogen gas bubbles. Therefore, it is clear that the laser treatment not only increased the adhesion ability but also improved corrosion resistance.

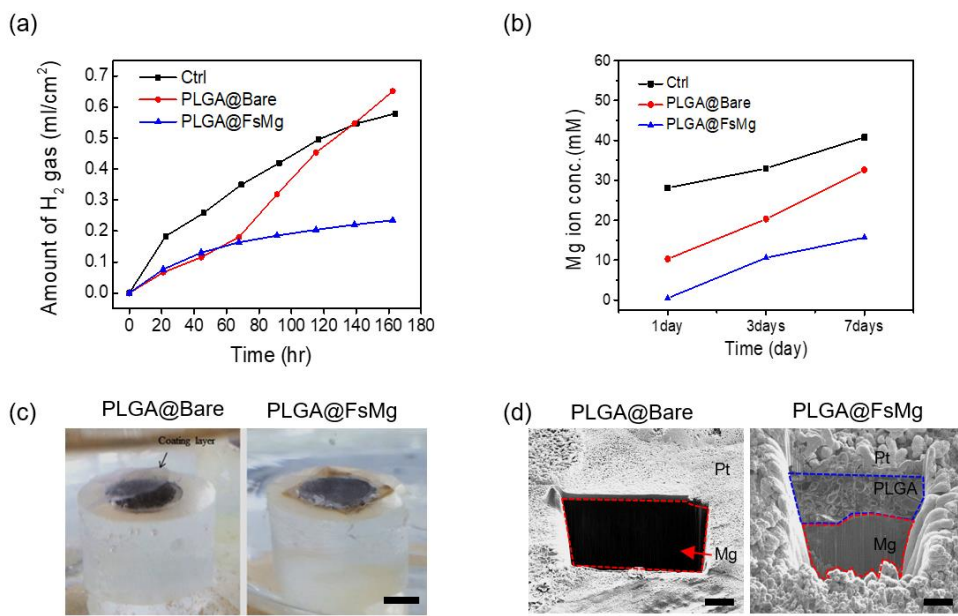


Fig. 3.5 (a) Amount of hydrogen gas and (b) concentration of Mg ion released by Ctrl, PLGA@Bare, and PLGA@FsMg. (c) The behavior of coating layer on substrates in immersion test after 7 days (left image: PLGA@Bare; right image: PLGA@FsMg); scale bar indicates 4 mm. (d) SEM images of cross-section after corrosion test (left image: PLGA@Bare; right image: PLGA@FsMg); scale bar indicates 20 μm.

3.3.4. Cell test

Mg samples coated with PLGA after fs laser treatment was incubated with cells to evaluate the stability of the PLGA coating layer under cell culture conditions, as shown in Fig. 3.6. To evaluate cell viability, L929 cells were directly seeded on PLGA-coated Mg substrates, cultured for 7 d, and displayed as normalized cell viability in Fig. 3.6a. PLGA@FsMg showed stable cell proliferation for 7 d. However, the viability decreased to 20% on PLGA@Bare on day 3 because cells on PLGA layers detached from the surface of Mg in the media following the trend observed in the corrosion test (Fig. 3.5c-d).

Although cells on bare Mg show stable cell attachment for 3 d, continuous release of hydrogen gas release could cause a problem for the implantable devices. Therefore, controlled corrosion of magnesium in a physiological environment could be the key to success for biomedical applications. Cell distribution on PLGA-coated Mg was visualized by SEM, which showed a lower number of cells distributed on PLGA@Bare, whereas a dense cell distribution was maintained on PLGA@FsMg for 3 d (Fig. 3.6b).

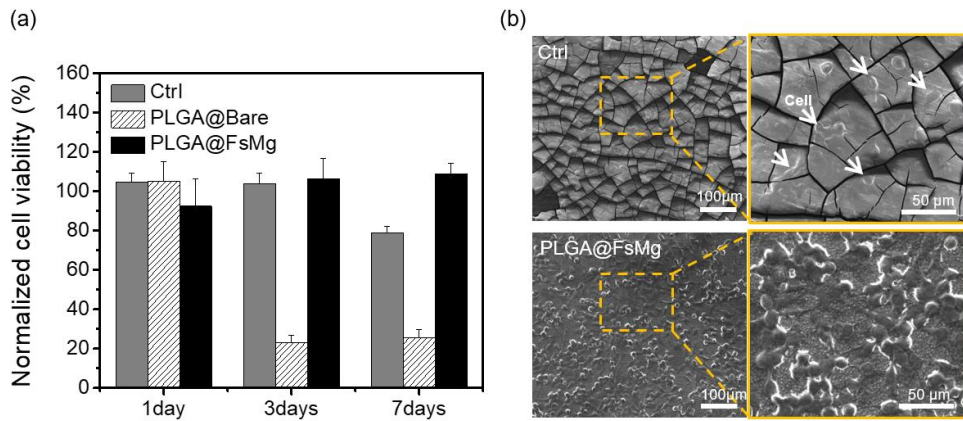


Fig. 3.6 (a) Cell viability of ctrl, PLGA@Bare, coating on PLGA@FsMg after immersion test in DMEM without serum for 1, 3, and 7 days. (b) Cell morphology on surface of ctrl (upper images) and PLGA@FsMg (below images) after corrosion test for 3 days.

3.4 Conclusion

In this study, we developed a quick and simple method to obtain physical and chemical modified Mg surface with extreme hydrophilic properties to improve the coating ability using an fs laser. Through an fs laser texturing technique, we physically modified the Mg surface to a textured surface and chemically modified it to a super-hydrophilic state, such that the coating material effectively penetrated, embedded, and interlocked into micro- nano- complex structures without any primers or chemical pretreatment. The enhanced coating quality led to increased adhesion strength and minimized the delamination from the substrate, resulting in improved corrosion properties and biocompatibility.

The introduction of the fs laser surface treatment technique on Mg to improve the polymer coating ability could open doors for the future application of completely biodegradable metallic devices with drug-eluting polymer coatings. Furthermore, it is especially beneficial for use in an industry where stable organic coating without chemical pretreatment is required.

Chapter 4. Hydroxyapatite coating via laser-induced hydrothermal process in the liquid precursor

4.1 Introduction

The coating material used for applications involving implants needs to be biocompatible and exhibit high resistance to corrosion. Based on these requirements, hydroxyapatite (HAp) is an appropriate candidate material that affords considerable advantages. It comprises Ca and P, which are the mineral components of bone tissue. Therefore, HAp is considered an excellent bioinert material as it provides a good environment for bone cells to adhere [144-150].

Among conventional CaP coating treatments, hydrothermal immersion [151-153] or biomimetic [154, 155] coating technology in supersaturated CaP solutions (dipping) has been studied based on stable nucleation and the growth of HAp. Similar to chemical coatings, physical coatings processes, which include thermal spray [156], plasma spray [157, 158], and sputtering [159, 160], have been used owing to their practical and definite adhesion between CaP and metallic substrates; however, physical coatings with high thermal energy can deform and damage the substrate. The chemical coating process based on the nucleation reaction is also not highly suitable because it commonly requires a prior complicated surface modification process and time-consuming HAp synthesis for completing the

formation of a firm adhesion coating layer on a metallic substrate [161]. Several methods have been designed for the coating process for practical implantable applications.

In this study, the surface of biodegradable Mg was treated in a supersaturated CaP solution with a nanosecond pulsed laser to combine the physical coating effect and chemical precipitation process in single-step coating without the requirement of any pretreatment such as plasma processing or chemical oxidation for functional applications.

Laser-induced single-step coating (LISSC) employs the effect of hydrothermal synthesis on a laser-irradiated solid (substrate)/liquid (coating precursor solution) interface. Deposition from the liquid state has advantages over other states of matter in terms of the relative ease of handling, simple setup, and recyclability [49, 162-165]. In addition, with LISSC coating, simultaneous synthesis and coating are possible on the surface of the material where the laser is focused. Therefore, various coating layers comprising desired materials can be formed depending on the type of immersion solution. In contrast, if the focal length of the laser is not automatically adjusted, it has the drawback of being difficult to apply to a complicated structural surface.

The laser-induced coating layer allows the development of CaP coating adhesion ability with minimal thickness, and this leads to improvement in the overall corrosion resistance of biodegradable metals.

The results of the analyses of the structural, crystallographic, and chemical properties verified the mechanism through which the coating ability between the coating layer and substrate increases. Furthermore, the implementation of processes such as cell adhesion and promotion of coating recovery for functional implants were checked in various ways, and finally, the applicability of this technique was confirmed by coating the implant device used in actual surgery.

4.2 Experimental Procedures

4.2.1. Preparation of laser-treated Mg

Cylindrical pure Mg (99.9% purity) extruded to a diameter of 8 mm was polished with a 2000 grip SiC paper for eliminating impurities on its surface before laser treatment. The polished samples were sequentially sonicated (SD-3000H, Mujiga, Korea) in 99% ethanol and acetone for 10 min. The cleaned Mg was placed in a 100-mm-diameter glass Petri dish for laser coating in a coating precursor solution.

The precursor solution contained calcium and phosphoric acid. The concentration of the modified CaP solution was increased by 1, 50, 100, and 150 times compared with Hank's balanced salt solution (HBSS; pH 7.4, WELGENE, Korea). CaCl₂ (1 M, C5670, Sigma-Aldrich, USA) and H₃PO₄ (1 M, P5811, Sigma-Aldrich, USA) solutions were used to form

supersaturated CaP precursor solution. The final modified solution was filtered 100 times, and it was transparent and without any precipitation because of the activation of buffer components in the HBSS. Thus, the stable CaP coating was performed only in the laser-focused area on the biodegradable Mg surface without the absorption of laser energy in the solution. Oxidation occurred on the surface of Mg, which was attributed to the change in the laser parameter in distilled water.

In this study, the surface/liquid interface was heated and melted using a nanosecond ytterbium fiber laser (Biolino MOPA, Laservall, Hong Kong) with a wavelength of 1064 nm and focal length of 160 mm. The spot size of the laser beam on the substrate was 60 μm in diameter. All samples were irradiated directly using a modified biomimetic solution with a laser processing system equipped with EZCAD software. The laser focus was translated at 100 mm/s using a galvo scanner operating at a repetition rate of 500 kHz with a laser beam emitting a Gaussian TEM₀₀ mode beam. Mg surface was irradiated with a pulse width of 200 ns, laser power of 10 W, and loop number of 50. The interval gap of the laser tracks was fixed at 10 μm in a zigzag manner. To form a uniform laser-induced coating layer on the screw, the focal length of the laser was fixed between the pit and groove of the screw. The circumferential area of the screw was divided into three sections; with the screw kept horizontal, each section was coated uniformly by laser treatment with simultaneous rotation. The screw used in this study

had a curved shape; the uniform coating on its surface was confirmed based on analyses through scanning electron microscopy (SEM) and corrosion experiments.

4.2.2. Surface characterization

The surfaces and cross-sections of the samples were examined using SEM (Inspect50, FEI, USA) to confirm the coating properties. The effects of laser treatment were analyzed using a secondary electron (SE) and a back-scattered electron (BSE) detector. Energy-dispersive X-ray spectroscopy (EDS) analysis equipped with SEM was used to measure the distribution and quantity of components. The 3D structures and roughness of the surfaces were analyzed using confocal laser scanning microscopy (LSM; LEXT OLS4100, Olympus, Japan), as the concentration of the solution was varied. X-ray diffraction (XRD; D8 ADVANCE, Bruker, USA) using Cu K α radiation was performed to determine the phases and characterize the microstructures of the coating materials. The measurements were conducted in the 2θ range of 10° - 90° in intervals of 0.02° . The oxygen level after laser surface treatment in distilled water (DW) was analyzed using X-ray photoelectron spectroscopy (XPS, PHI 5000, ULVAC-PHI, Japan) with a monochromator (Al K α source, 1486.6 eV, with a C 1s peak of 286.6 eV), and the beam size was $100 \times 100 \mu\text{m}^2$. The crystallinity and

elemental distributions of CaP on the Mg surface were simultaneously detected via scanning transmission electron microscopy (STEM; Talos F200X, FEI, USA) with a Super-X EDS detector. The ratio of Ca to P was calculated without other elements for a precise analysis of the laser-induced HAp coating layer. Selected area electron diffraction (SAED) patterns were measured for the crystallinity analysis of coating layers and substrates.

4.2.3. Analysis of coating property

Electrochemical corrosion properties were measured through polarization curves (263A potentiostat/galvanostat, Princeton Applied Research, USA). This analysis was performed at 37 °C in a beaker containing HBSS with Ag/AgCl as the standard reference electrode. The working electrode was a specimen with an exposed area of approximately 0.25 cm², and a platinum electrode served as the counter electrode. The corrosion potential and current density were measured at a scan rate of 0.05 V/s from -2 to -1 V. The corrosion rate (P_i) was calculated from the current density based on the following equation: $P_i = 22.85i_{\text{corr}}$. The optimal solution conditions were confirmed through Tafel analysis.

A peel-off test was performed using adhesive tape (Scotch™ 810, 3M, USA) to compare the adhesive properties of the thermally formed HAp region (TFH) and laser-induced HAp (LIH) coating region. A scratch test

was performed for the quantitative analysis. Subsequently, the adhesion strength was evaluated using a scratch tester (RST3, Anton Paar, Austria). A Rockwell-type spherical diamond tip with a radius of 10 μm was used as the scratch indenter. The scratch scanning speed was 10 mm/min, and the applied load was progressively increased from 500 to 4000 mN. The measured critical scratch load for each condition was calculated as the average value.

Mg substrates coated with CaP were immersed in a serum-free 1X Dulbecco's modified Eagle's medium (DMEM; LM001-05, WELGENE, Korea) at the area of constant exposure. The immersed samples were incubated at 37 °C in a 5% CO₂ environment to simulate the human physiological environment. A portion of Mg-ion-eluted DMEM was drawn off after 1, 3, and 7 days; the Mg ions were assayed using the Quantichrom metal ion assay kit series (DIMG-250, Bioassay Systems, USA). The corroded surfaces and cross-sections were dried in air and examined using optical microscopy (OM) and SEM after immersion tests in the DMEM. The property of coating recovery was detected after scratching the surface with a needle with a stable applied force of 3N, and the surface properties were analyzed using SEM and EDS.

EDS analysis was employed after the scratched specimens were left to corrode for 4 weeks to perform a corrosion characteristics analysis with and without HAp coating. The cross-section was examined using an electron

microscope immediately after the scratch was formed on each specimen, and the depth of damage was measured and compared using ImageJ (Image processing program, NIH). A mapping image of the Ca, P, Mg, and O components of the cross-section using the EDS analysis of the specimens corroded for 4 weeks after the scratch formation was used. Based on the location of scratch formation on this image, the depth of corrosion based on the distance was measured using the ImageJ program. After arranging the measured values using the Excel program, the statistical significance was analyzed and graphed as the origin (Origin 2020, OriginLab, USA). In addition, LISSC was applied to commercially available biodegradable orthopedic implant screws (Mg-Ca alloy, Resomet Bioresorbable bone screw; U&I Corp., Korea). The bottom halves of the screws were implanted on the artificial bones (saw bones) to check the delamination of the coating layer during the screwing process, and the effect of the LIH coating was verified using immersion corrosion tests for 4 weeks by comparing the cross-sections to those of uncoated screws. The result confirmed that the resistance to corrosion of the LIH-coated screw with a strong coating ability had improved despite externally applied stress.

4.2.4 Cell test (confocal microscopy)

The adhesion properties of osteoblasts on laser-based hydroxyapatite-coated surfaces were confirmed. Disk-shaped magnesium specimens (diameter = 8 mm) were prepared and tape-masked and only half of the specimens were selectively coated with HAp. The coated specimens were cleaned ultrasonically for 10 min each using acetone (98%, Sigma-Aldrich, USA) and ethanol (99.8%, Sigma-Aldrich, USA) and stored in a desiccator until the experiment. The osteoblasts (M3T3T-E1, ATCC, USA) were prepared for evaluating cell adhesion. The apatite-coated specimen was placed in a 24-well plate, and 1 mL of the minimum essential medium was filled with an alpha modification solution (Alpha-MEM, WELGENE, Korea) containing 10% fetal bovine serum (FBS, HyClone, USA) and 1% penicillin-streptomycin (Gibco, USA) media. The cells were seeded at 5.0×10^4 cells/well. Incubation at 37 °C, 5% CO₂, and 95% humidity for 3 h provided time for the cells to adhere to the material surface. Thereafter, the cell culture media were removed, and 2 mL of phosphate-buffered saline (PBS, WELGENE, Korea) was freshened three times to remove cells that did not adhere to the surface and the excess culture medium. The cells were fixed in a 4% paraformaldehyde solution at 4 °C for 20 min and permeabilized with 0.5% Triton X-100 PBS solution for 5 min. After rinsing three times with PBS, a 1% FBS solution was added and blocked for 30 min.

The cytoplasm was stained with rhodamine-phalloidin (R415, Invitrogen, USA) and the mounting medium for fluorescence with the DAPI solution (H-1200, Vector Laboratories, USA). Images were obtained using a fluorescence microscope (Imager A2m, ZEISS, Germany).

4.3 Results and Discussion

4.3.1. Surface analysis after HAp coating through LISSC for modifying a biomimetic solution

Fig. 4.1 illustrates the process of LISSC in a biomimetic precursor solution. As depicted in the scheme, the type, amount, and concentration of the precursor solution can be easily controlled. An experiment was conducted to confirm the changes in the Mg surface depending on the concentration of Ca and P in the solution. The surface morphologies of laser-treated specimens placed in DW and HBSS 1X solutions were similar, as depicted in Fig. 4.2. However, the amount of oxide in DW and HBSS 1X increased compared with the control (Table 3). Further, HAp started to precipitate in the form of particles following laser treatment in the HBSS 1X solution. HAp is nucleated and grown in the HBSS 50X solution by increasing the concentrations of Ca and P; the coating layer was stably formed up to HBSS 100X, but a valley-shaped morphology is formed when the concentration is higher than HBSS 150X. This leads to increased surface roughness, which provides pitting corrosion sites that accelerate the corrosion process.

Fig. 4.3 presents the results of analyzing the ratio of Ca (coating layer) and Mg (substrate) examined using EDS; the results indicate that the

ratio increased up to HBSS 100X, and then dropped sharply under the HBSS 150X condition. A large amount of hydrogen gas is generated on the Mg surface under HBSS 150X during the laser coating process, and it led to the dispersion of the laser beam. Further, the scattering of the beam was induced by the generation of floats during the laser treatment process; therefore, the coating layer could not be formed evenly.

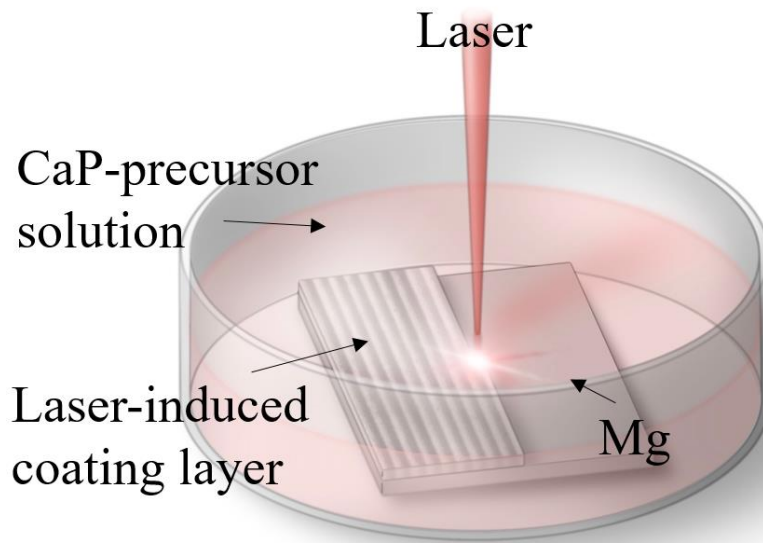


Fig. 4.1 Schematic of LISSC in the precursor solution.

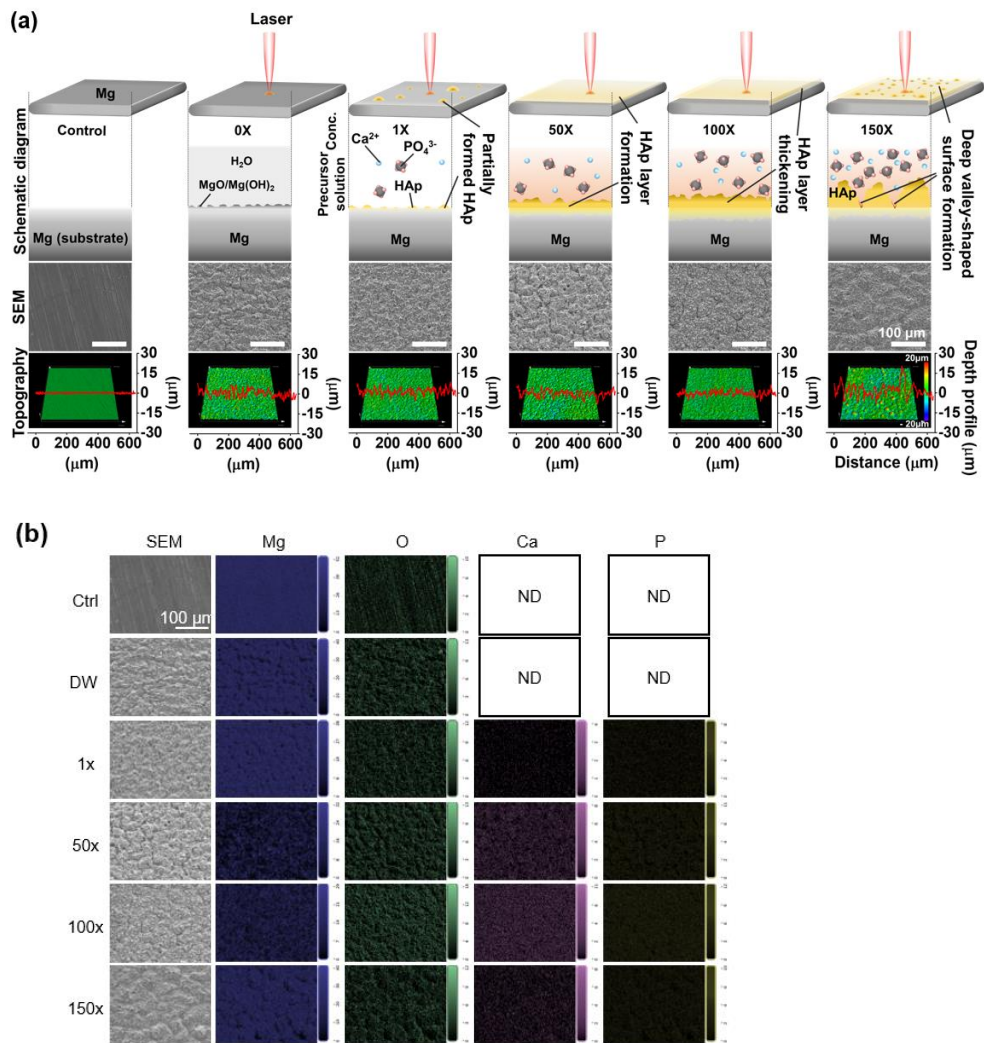


Fig. 4.2 (a) Surface analysis of SEM images and roughness profile with 3D microscopy under each solution condition following laser treatment. (b) Mapping images of laser-treated and bare Mg in modified biomimetic solution. Each color indicates Mg (blue), O (green), Ca (purple), and P (yellow). The contrast shows the quantity of each element on the surface after laser treatment.

Table 3. Elemental components of laser-treated samples on the surface; Magnesium (Mg), Oxide (O), Calcium (Ca), Phosphate (P).

At (%)	Mg	O	Ca	P
Ctrl	92.60	7.40	.	.
D.W	78.91	21.09	.	.
1x	77.56	15.58	0.85	6.02
50x	35.30	43.20	10.94	10.55
100x	31.32	42.75	12.72	13.20
150x	69.51	20.15	3.11	7.24

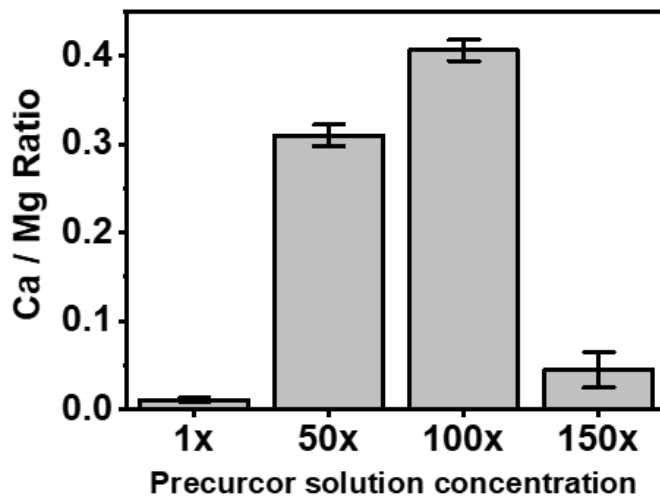


Fig. 4.3 Ratio of Ca and Mg at the modified biomimetic solution.

Fig. 4.4a and Table 4 present the electrochemical analysis to confirm the effect of the coating properties for each concentration. The corrosion potential of HBSS 1X was lower than that of the control because the HAp coating was not formed on the Mg surface; the surface area increased with roughness. The corrosion potential under the HBSS 50X condition was improved because of the formation of not only a barrier of precipitated HAp but also a MgO layer. The corrosion potential increases until the HBSS 100X condition and starts decreasing under HBSS 150X owing to the formation of valleys and the uneven coating layer. Thus, a concentration condition of HBSS 100X with a stable coating layer was selected as the laser-induced coating for the effective formation of the HAp coating layer; subsequently, a series of experiments were conducted. Fig. S1b presents the image seen by mapping the cross-section under the selected coating condition HBSS 100X. Ca, P, and O, the components of HAp, were evenly distributed on the surface.

As depicted in Fig. 4.4b, XRD analysis was performed to confirm whether the surface of the coating layer formed by laser irradiation was HAp. Following the laser coating, peaks indicating $\text{Ca}_{10}(\text{PO}_4)_6(\text{OH})_2$, which represent the HAp phase (JCPDS 09-0432), were seen. Therefore, the HAp coating layer was formed on the surface through laser-induced coating processing; a further detailed analysis was conducted using TEM.

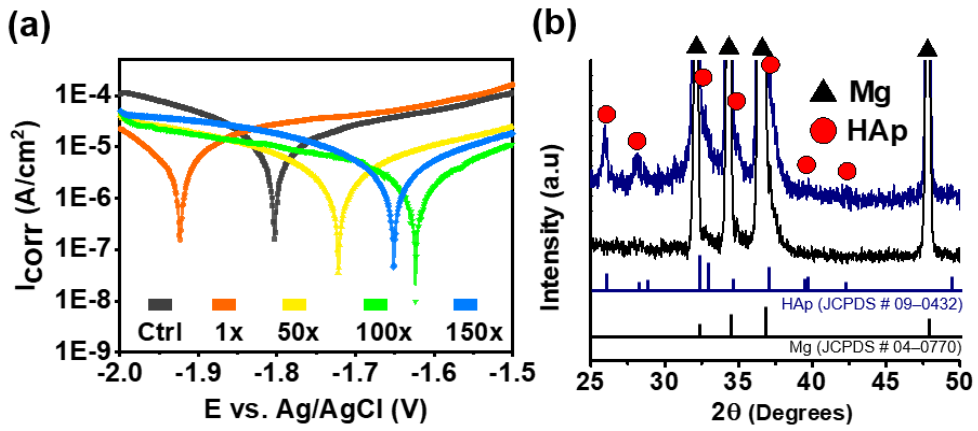


Fig. 4.4 (a) Electrochemical polarization curve with Ag/AgCl as the standard reference electrode and platinum as the counter electrode. (b) XRD curves of as-received (control) and laser-treated surface in biomimetic solution at 100X concentration.

Table 4. The difference in E_{corr} , I_{corr} , and P_i between specimens, as determined from the polarization test.

	E vs. Ag/AgCl (V)	I_{corr} (A/cm ²)	P_i (mm/year)
Ctrl	-1.80	7.17×10^{-6}	1.63×10^{-1}
1x	-1.92	6.95×10^{-6}	1.58×10^{-1}
50x	-1.72	2.78×10^{-6}	6.35×10^{-2}
100x	-1.62	1.34×10^{-6}	3.06×10^{-2}
150x	-1.65	2.93×10^{-6}	6.69×10^{-2}

4.3.2. Improvement of coating ability

As depicted in Fig. 4.5a, peel-off and scratch tests were performed to determine how well the coating layer formed by the laser adhered to Mg. The HAp-covered layer, which is similar to the immersion coating surface, is seen even in an area not affected by the direct laser beam because Mg has high thermal conductivity ($156 \text{ W m}^{-1} \text{ K}^{-1}$) and it reacts with a solution on the surface during the process. This region is referred to as a TFH region. A peel-off test was performed after the two regions were simultaneously formed on the same Mg surface to compare the adhesion properties of the LIH coating layer and TFH region. Fig. 4.5b illustrates that bare, THF, and LIH areas are formed in three sections; the coating layer is peeled off using tape on the right half of the sample. As depicted in Fig. 4.5c-f and as seen from the coating layer at the interface through EDS images before (Fig. 4.5c-d) and after (Fig. 4.5e-f) the peel-off test, Ca and P were evenly distributed on the coating layer in the LIH region. In contrast, the coating layer was peeled off completely from the interface of the TFH region, which resulted in the exposure of the Mg surface. Further, the difference between the TFH and LIH layers could be seen with the naked eye depending on the gloss after the peel-off test. The HAp of the TFH region was deposited on the surface with a weak adhesion force.

A scratch test was performed to quantitatively analyze the adhesion strength (Fig. 4.5g). The breakpoints were measured more precisely by mapping. The adhesion strength of the LIH region increased by approximately 26.52% when compared with the TFH region. (TFH: 6615.9 mN, LIH: 8370.5 mN). Further, a coating layer remaining in the LIH area was detected beyond the scratched area.

Fig. 4.6a presents the EDS mapping of each coated area before the peel-off test. The TFH region has several parts where Mg is exposed along with cracks. In the LIH region, Ca and P are well distributed along the Mg surface. OM images indicating the corrosion aspect for 7 days after the peel-off test (Fig. 4.6b). On the 7th day in the TFH region, both before and after the peel-off test, the bare area exhibited similar corrosion patterns. Interestingly, after the peel-off test, the area in the LIH region displayed a surface similar to that before the test. This is attributed to the improved bonding ability of the coating layer. Fig. S3 depicts the corrosion results at 1 and 4 weeks after the peel-off test through SEM images. In the TFH region, cracks were seen not only in the region affected by the peel-off test but also in that covered with the HAp layer. In the LIH area, the HAp coating layer remained even in the area affected by the tape test. The morphology of the coating layer did not change significantly following the immersion experiment for 4 weeks.

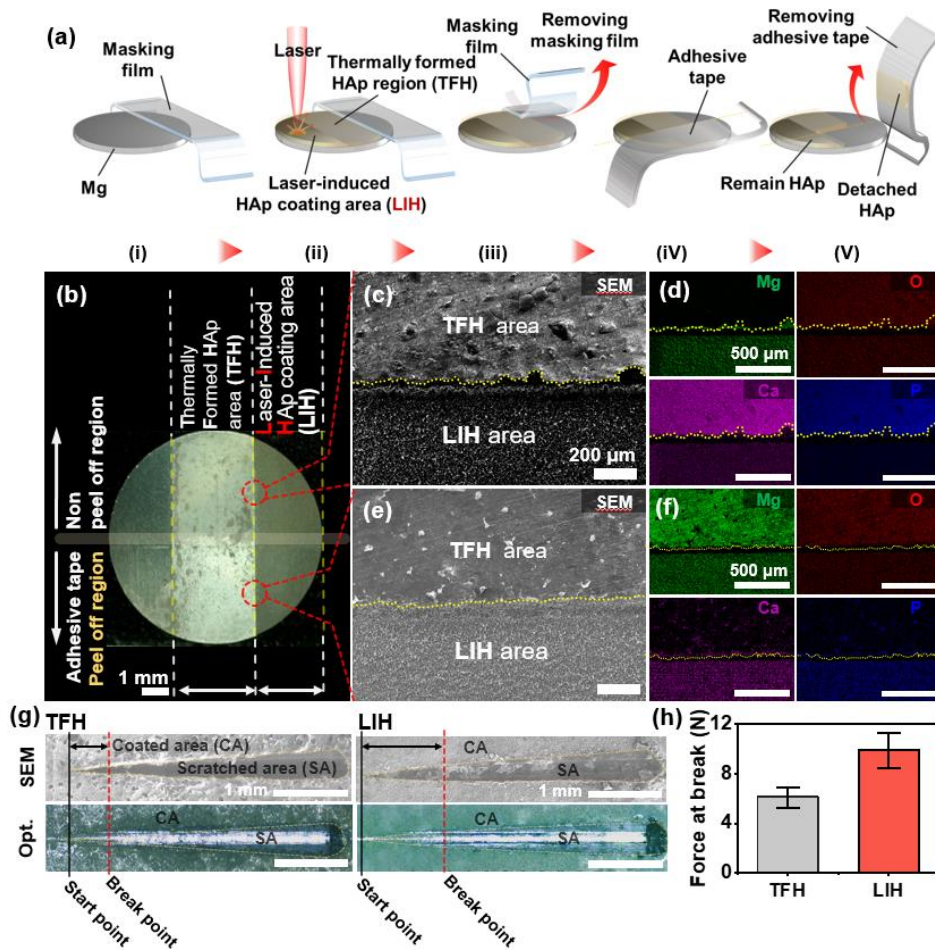


Fig. 4.5 Comparison of coating ability between thermally indirect layer and the laser-induced coating layer. (a) Illustration of adhesion test. (b) OM images before and after peel-off test in the bare, TFH, and LIH areas. (c, d) SEM and mapping of each element before the adhesion test. (e, f) SEM and distribution of Mg, O, Ca, and P after the peel-off test using adhesive tape. (g) Optical and SEM surface images following the scratch test. (h) Graph representing the critical load of the scratch test where interface breakage occurs.

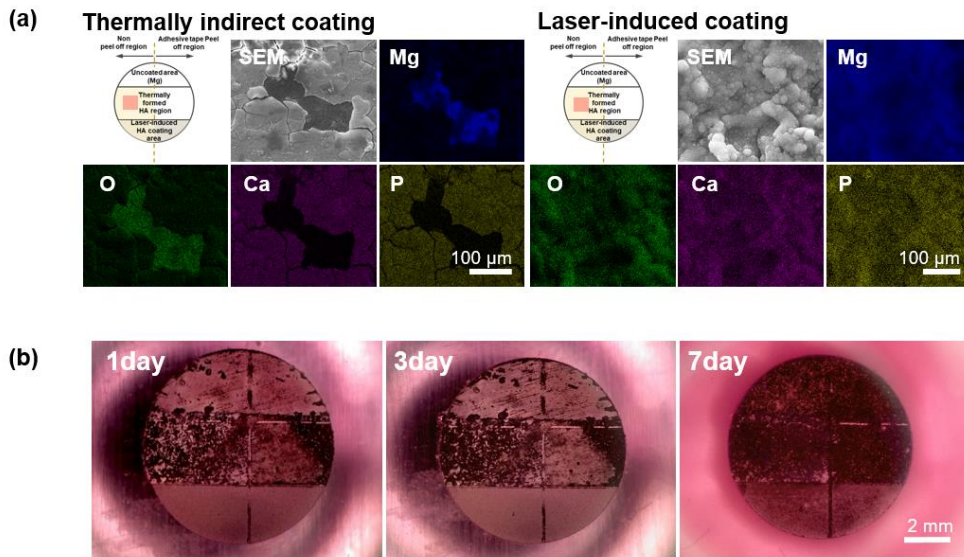


Fig. 4.6 (a) SEM surface images of coating layer after laser treatment. CaP coating layer evenly formed by laser (left) and peeled coating layer due to poor adhesion at thermally indirect region (right). (b) OM images in DMEM; bare, thermally formed region, and laser-induced coating region at 1,3, 7 days after the peel-off test.

4.3.3. Increased corrosion resistance on LIH coating layer

The cross-section of the coating layer is monitored following corrosion for 4 weeks, as depicted in Fig. 4.7. Corrosion products and oxide layers generated by the corrosion reaction are seen in the cross-section of the control. In contrast, in the TFH region, a thick oxide layer is detected because of media penetration between the disconnected coating layers. There is no significant difference from the control because the coating layer with a weak adhesion bond does not function properly. Interestingly, the corrosion products and oxide layer were thinner than under other conditions because the strong bonding and dense coating layer effectively blocked the corrosion-causing elements. Further, it was confirmed that the LIH coating remained intact through the cross-sectional Ca and P of the mapping images. This improvement in the corrosion property is directly related to the enhanced ability of the coating layer from the laser processing, which leads to quick recovery and restoration from the mechanical defects of the coating layer by forming a strong bond with the substrate [166-168]. A scratch was applied with a constant force, and SEM images were obtained 4 and 8 weeks following corrosion (Figs. 4.8). The simply placed HAp layer in the TFH region detached from the surrounding layer by scratching, and pitting corrosion proceeded between the broken scratch tracks. In the LIH region, the coating layer recovered over the scratched site by improved adhesion

bonding and minimized delamination from the substrate. This aspect was maintained for up to 8 weeks, which led to shallow and uniform corrosion for the same duration. Based on these results, it was confirmed that the coating ability of the LIH supported the rapid recovery of the HAp layer, which led to improved corrosion properties. As depicted in Fig. 4.9, the corrosion areas were measured from the scratched cross-sectional EDS mapping images following 4 weeks of the corrosion test for the quantitative analysis. As indicated in Fig. 4.9b, there was no significant difference in the scratch depth. However, as depicted in Fig. 4.9c, a deeper corrosion layer can be seen in the TFH region when compared with the LIH region. Pitting corrosion proceeds in the unrecovered coating layer, whereas the corrosion does not proceed further in the LIH area, where the scratches are somewhat recovered.

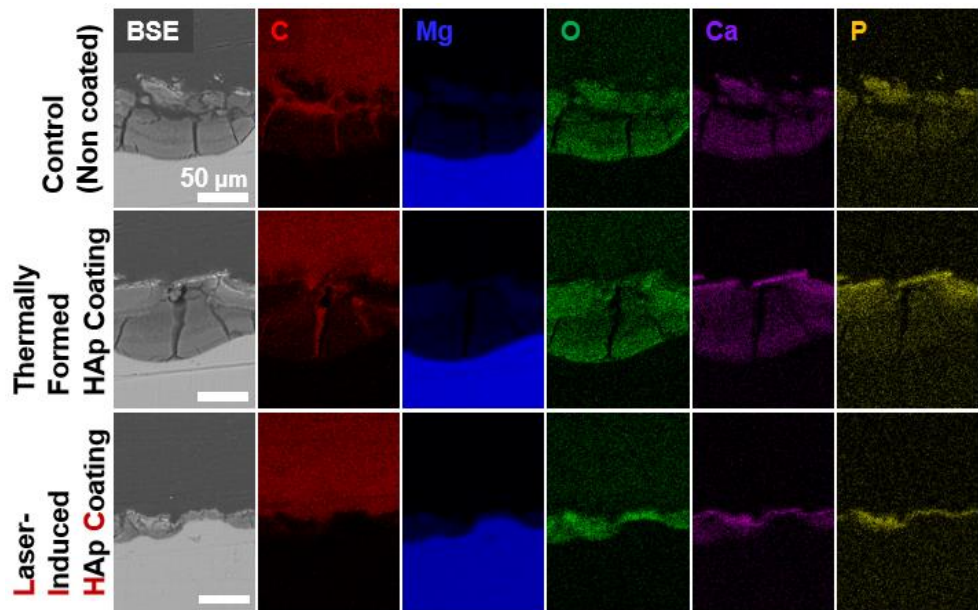


Fig. 4.7 EDS mapping of cross-section 4 weeks following the corrosion test on each area on the Mg surface.

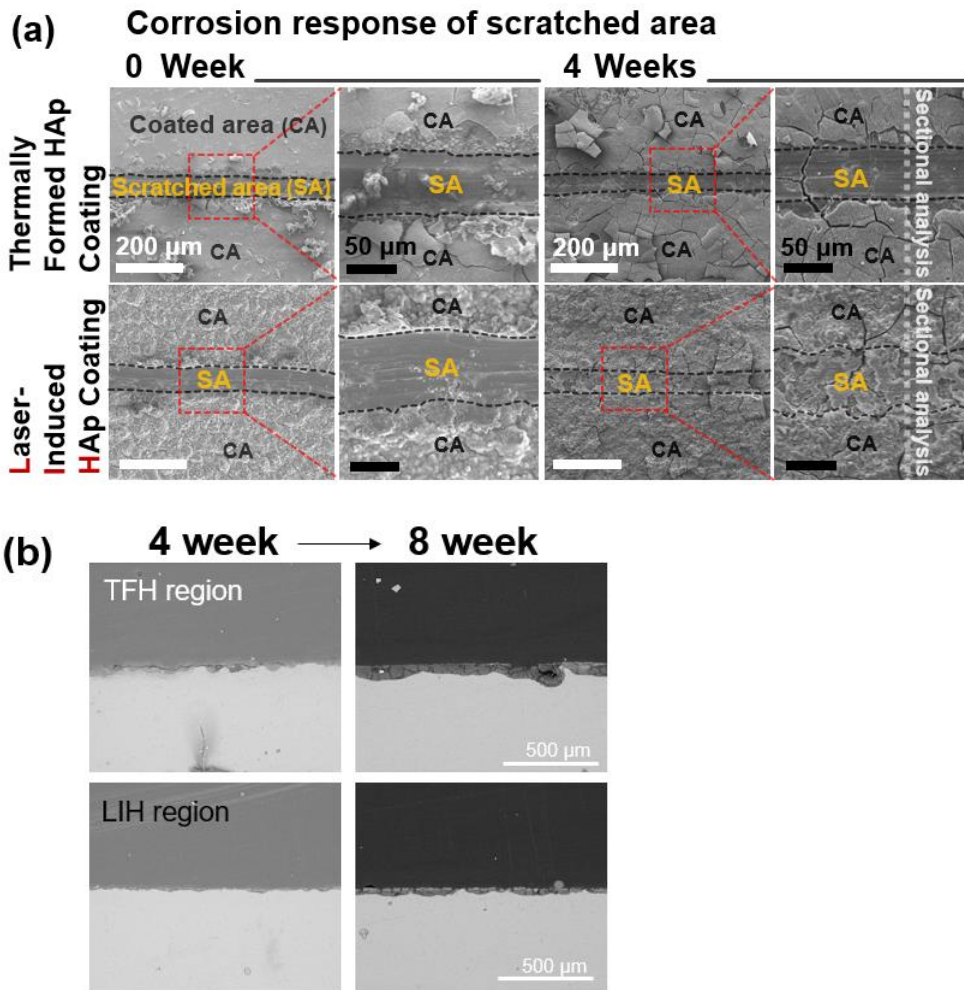


Fig. 4.8 (a) SEM images under each condition after the corrosion test: scratched area (SA) and coated area (CA). (b) Cross-sectional BSE images on each condition at 4 weeks and 8 weeks after the scratch test.

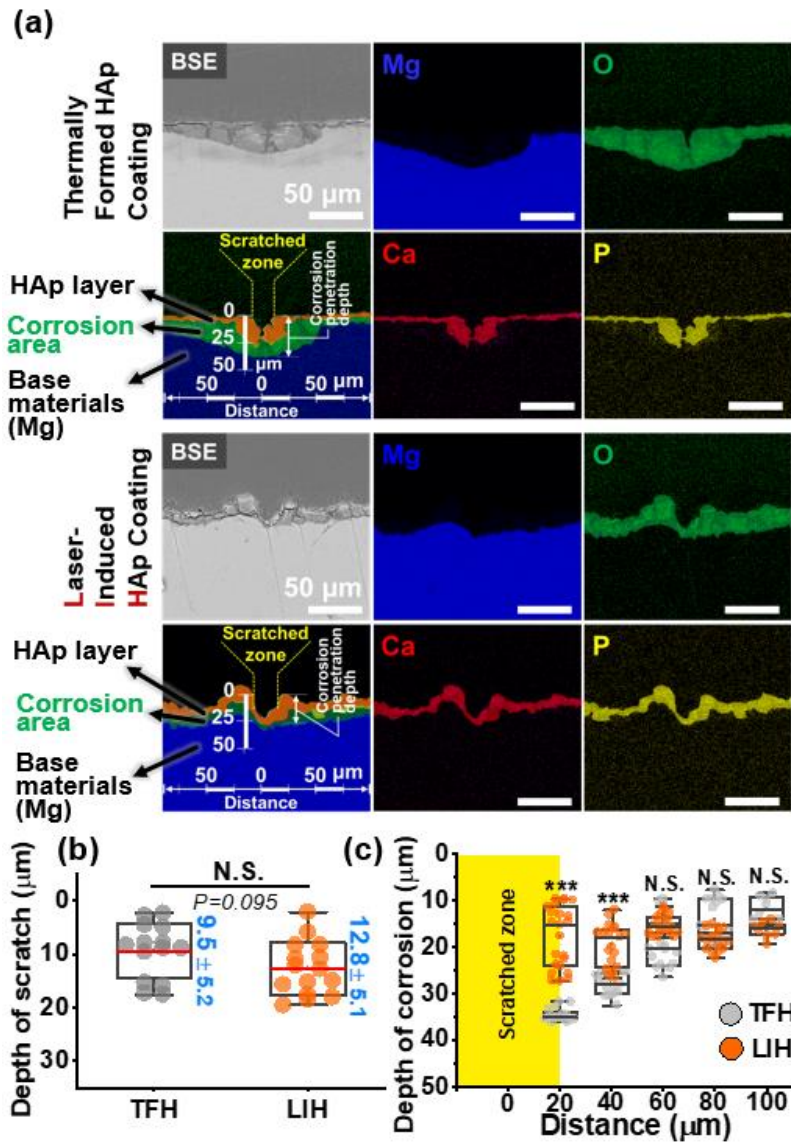


Fig. 4.9 (a) Cross-section of BSE and mapping under each condition 4 weeks after the scratch test. (b) Depth profile analysis at the scratched zones of the TFH and LIH regions. (c) Depth of corrosion as a function of the distance from the scratched zone.

4.3.4. Cross section analysis through TEM

The results of the TEM-EDS analysis indicated that the LIH surface comprised Ca, P, O, and Mg. Ca, P, and O appeared in the region formed by the laser energy (Fig. 4.10a). A reticular morphology, such as the structure of HAp, was detected in the uppermost part of the cross-section [152, 169-172]. In addition, the Mg at the interface physically holds the HAp coating as a hooked layer with a complex shape, which leads to improved adhesion strength [173]. The crystal properties of the coating layer and Mg substrate were investigated using the SAED pattern analysis (Fig. 4.10b). The SAED image of the part named number 2 does not exhibit crystalline rings or spots, confirming its amorphous nature. The Mg substrate named number 5 exhibited a metallic crystal structure; the d-spacing values of 2.78, 2.45, and 1.38 Å corresponded to (100), (101), and (200) of Mg (JCPDS 04-0770), respectively. High-resolution TEM analysis verified that the gradient component changes were achieved through the presence of HAp, MgO, and Mg at the interface (Fig. 4.10c). The element transition indicated that the ratio of Ca and P gradually decreased as Mg increased at the cross-section (Fig. 4.10d). This result indicates that the gradient element distribution allows bonding between the HAp coating layer and Mg substrate to improve the coating ability.

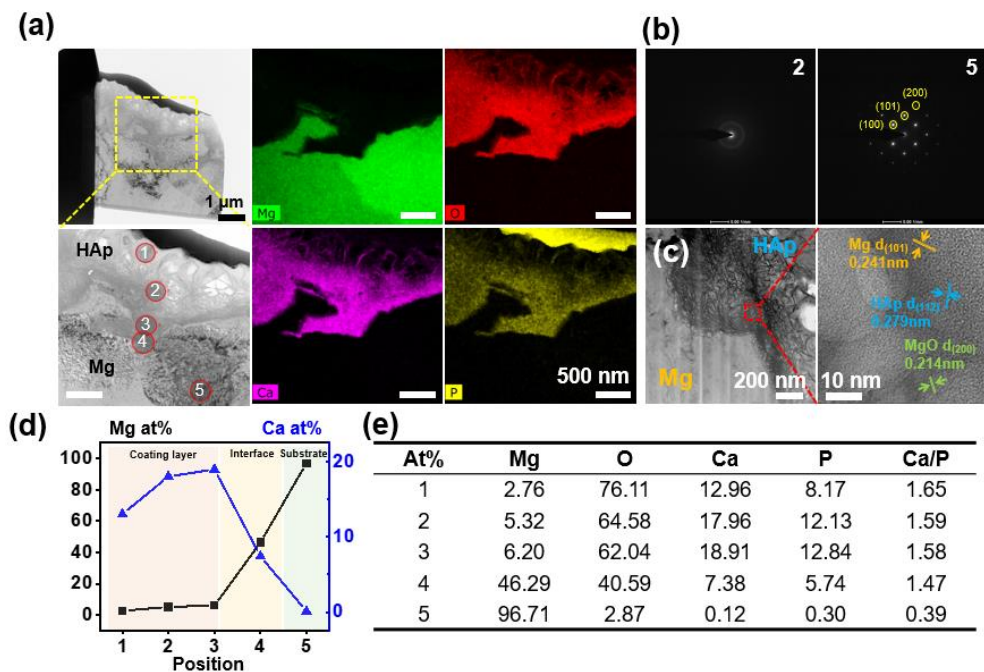


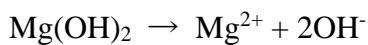
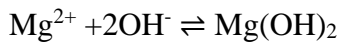
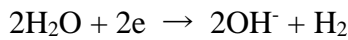
Fig. 4.10 (a) TEM-EDS of cross-section mapping in the LIH region. (b) SAED pattern in the HAp and Mg regions. (c) HR investigation at the boundary between CaP and Mg. (d) Distribution of Mg and Ca at each point of the cross-section. (e) Atomic percent of elements at the sections. TEM-EDS: transmission electron microscopy/energy-dispersive X-ray spectroscopy; SAED: selected area electron diffraction; HR: high-resolution.

4.3.5. Mechanism of HAp synthesis and coating

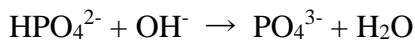
The formation of this surface can be explained through the Soret effect and hydrothermal synthesis [162-165, 174, 175]. The substrate/precursor interface is exposed to the rapid and localized energy of the laser beam, which leads to thermodynamic nonequilibrium conditions. This phenomenon induces large temperature gradients and thermal diffusion, which promote the separation of ions based on the Soret coefficients. In this process, the bulk motion of the liquid creates a convection flow, which leads to a collection of the coating material toward the irradiated area.

Laser energy accelerates the oxidation of the Mg surface based on hydrothermal synthesis [176]. Therefore, we confirmed the oxygen content and binding energy through surface analysis after the laser treatment of Mg in DW. The oxide content on the laser-treated surface was measured using EDS analysis. The surface melted more evenly, and the roughness increased with an increase in the number of the loop (Fig. 4.11a). When the number of loops exceeded 50, the surface changed into bumps because of the excessive laser energy. The amount of oxygen increased after laser treatment in DW (Fig. 4.11b). An examination of the cross-section indicated the formation of a clear oxide layer on the surface promoted by laser energy (Fig. 4.11c). The degree of oxidation was confirmed through XPS analysis for qualitative analysis at the core-level states (Fig. 4.11d-e). Compared to the binding

energy of the elemental atom, atoms in a higher positive oxidation state will have larger binding energy owing to the additional Coulombic interaction between the photoelectron and the atom core. Therefore, in this study, an increase in binding energy indicated an increased degree of oxidation. For the bare samples, the Mg and O peaks were located at 51.6 and 533.5 eV, respectively. Further, the binding energies of O and Mg increased with an increase in the number of loops; therefore, laser treatment in DW directly affects the oxidation of the Mg surface, which results in the rapid formation of a firm CaP coating layer. The natural reaction of Mg in an aqueous solution to understand the effect of surface oxidation on HAp layer production is expressed as follows [12, 78]:



The chemical reaction in which HAp is generated on the surface of Mg is as follows:



HAp-based compounds require OH⁻, which is supplied by Mg(OH)₂. It was hypothesized that Mg naturally generates MgO/Mg(OH)₂ in an aqueous solution; however, the laser further promotes the formation of MgO/Mg(OH)₂.

Distilled water has a refractive index of 1.2×10^{-6} at 1064 nm wavelength. According to this formula, the optical penetration depth is $l_{\alpha} = \alpha^{-1} = \lambda / 4\pi\kappa = 7$ cm, where α is the absorption coefficient, λ is the wavelength, and κ is the refractive index. We fixed the distance between the liquid surface and the Mg substrate to 0.5 cm to reduce water absorption. In particular, the laser traveled roughly 1/14 of its penetration depth in water before being absorbed by the Mg substrate. As a result, we assume the laser energy was mostly absorbed by the Mg substrate rather than water.

Assuming that the laser energy is completely absorbed by the Mg substrate, the temperature change at 200 ns is the following equation.

$$T_s = T_0 + \frac{A \cdot I \cdot \sqrt{\kappa \cdot t \cdot \pi}}{K} \quad (3)$$

where A is absorption coefficient, I is fluence of laser, κ is thermal diffusivity, t is time, and K is thermal conductivity. In this study, It was calculated to instantaneously raise the temperature up to 3765.69K. By the following reaction, $\text{Mg} + \text{H}_2\text{O} \rightarrow \text{MgO} + \text{H}_2$, the thermal energy of the laser is higher than the temperature for surface oxidation, which means that the

forward reaction can occur quickly enough. Therefore, the laser promotes the formation of Mg oxide, so that HAp can be effectively formed on the surface.

The overall mechanism of the CaP coating with the laser is illustrated in Fig. 4.12. First, the Mg melting and MgO/Mg(OH)₂ generation sites were created by laser irradiation. Thereafter, MgO/Mg(OH)₂ was evenly formed on the laser-treated surface with an increase in the number of loops, and Ca and P in the solution mixed with the OH⁻ supplied by the generated MgO/Mg(OH)₂. The generated layer was mixed with the Mg substrate via the laser energy supply to induce physical bonding when more than a certain portion of the HAp layer was formed.

In general, the laser beam supplied sufficient energy to form HAp on the surface of Mg, and the reactant synthesis and coating were carried out simultaneously on the surface. The coating layer was physically interlocked by the formation of the elemental gradient and the coexisting zone at the interface, thereby improving the bonding force of the coating.

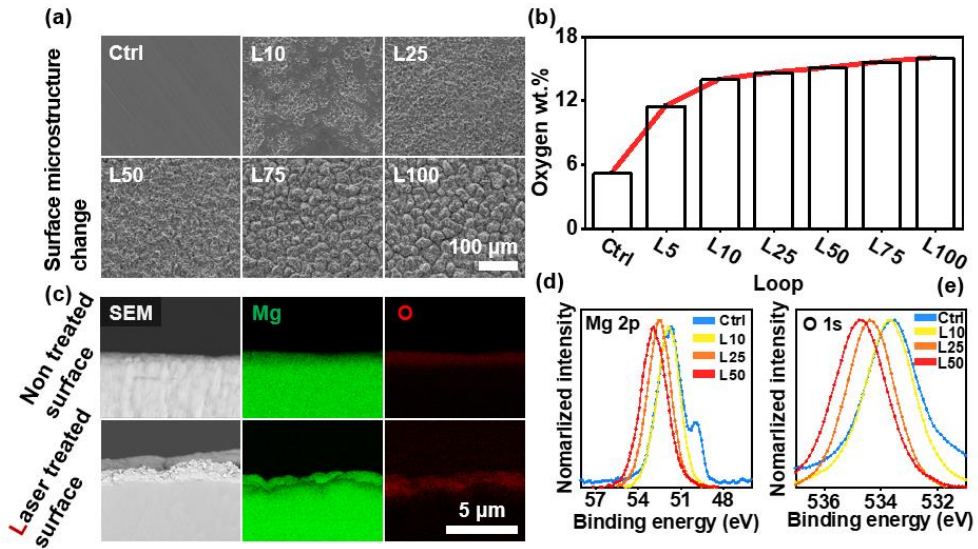


Fig. 4.11 (a) SEM images depicting surface morphology after laser processing in DW. The surface was melted by increasing the number of laser loops. (b) Weight percent (wt%) change in oxygen under each laser loop condition. (c) Cross-section images after laser treatment under the 50 loops condition in DW. (d, e) XPS spectra of Mg 2p and O 1s at each loop.

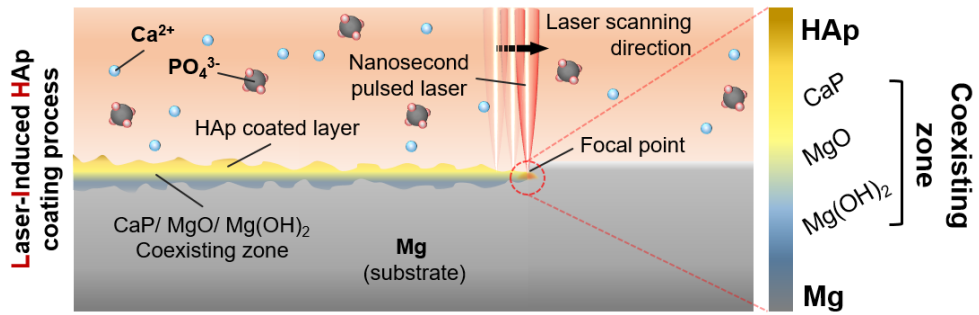


Fig. 4.12 Schematic depicting the mechanism of LIH coating on the Mg substrate.

4.3.6. Coating process on degradable screw and enhancement of biocompatibility on the LIH surface

Biodegradable Mg screws are used in the field of orthopedic surgery. In this study, bare and LIH-coated screws were inserted up to half into sawbones (implanted area) to examine the degree of peeling and the effect of LIH coating following the corrosion test (Fig. 4.13). The results of corrosion in the bare screw after the first week indicate that hydrogen gas was generated over the entire control sample surface, whereas the surface remained stable in the case of the LIH-coated screw, without the rapid formation of hydrogen gas even in the implanted area. This aspect was maintained even after 3–7 days of changing the solution (Fig. 4.13a). Cross-section mapping before and after the insertion test for the control and LIH-coated screws were compared, as depicted in Fig. 4.13b-c. The degree of corrosion can be estimated through the oxide distribution of the mapping because the oxide compound is formed during the corrosion reaction. The corrosion reaction continued on the bare sample, but the HAp coating layer remained intact on the LIH screw in the exposed area as well as the inserted area even after a week. The coating layer did not peel off owing to shear stress because of the improved coating ability of the LIH-coated screw. Thus, this technique can be applied in actual clinical practice by employing the same orthopedic implant process.

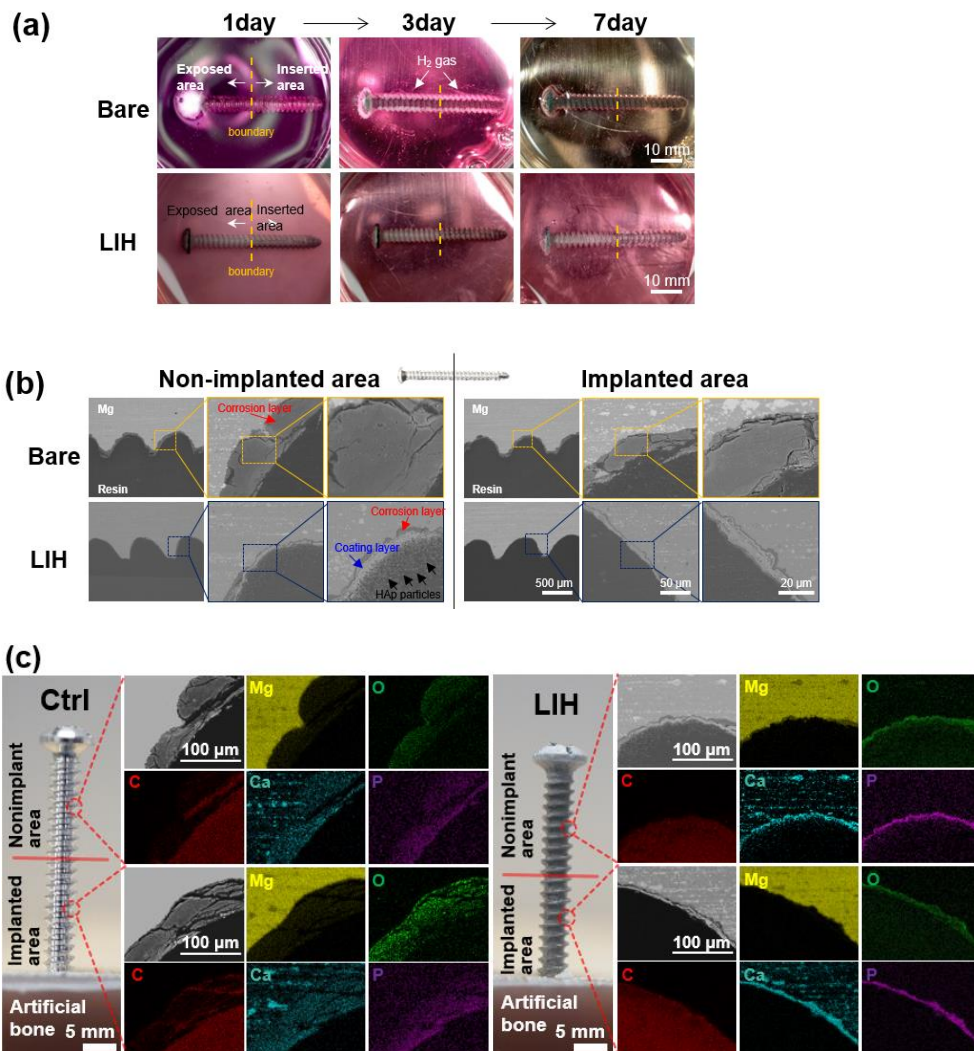


Fig. 4.13 (a) OM images for Mg screws after corrosion test in DMEM for 1, 3, and 7 days. (b) Cross-section of BSE for each condition of Mg implantable screw for 1 week. (c) EDS Mapping of cross-section after corrosion test 4W on each area on Mg surface.

As depicted in Fig. 4.14a, the Mg-ion concentration profiles at the LIH layer and the control were analyzed for a more quantitative comparison of the anticorrosion effect. The Mg-ion elution amount was 15.73 ± 5.35 and 1.04 ± 7.68 mM for the bare specimen and LIH region, respectively, on day 1. On the 7th day, the gap in the quantity of Mg-ion elution widened further: the value was 21.02 ± 7.36 mM for the LIH region, and it decreased by 58.76% compared with 50.97 ± 10.33 mM for the bare sample. Subsequently, cell adhesion was examined to confirm the amount of Mg-ion release and the reactivity of cells in vitro (Fig. 4.14b-e). The nucleus of the cell is represented by blue color and the cytoplasm is represented by orange color. The area of the bare surface where hydrogen gas is generated by the corrosion reaction was examined; in this area, the cells did not adhere and the region remained vacant. In contrast, dense cells could be seen easily in the LIH region, which indicates excellent biocompatibility of the HAp layer formed by the laser treatment and the remarkable osseointegration, as indicated by stable cell adhesion. Further, it was illustrated that the cell adhesion region in the LIH increased by approximately 2 times compared with the bare surface (Fig. 4.14e).

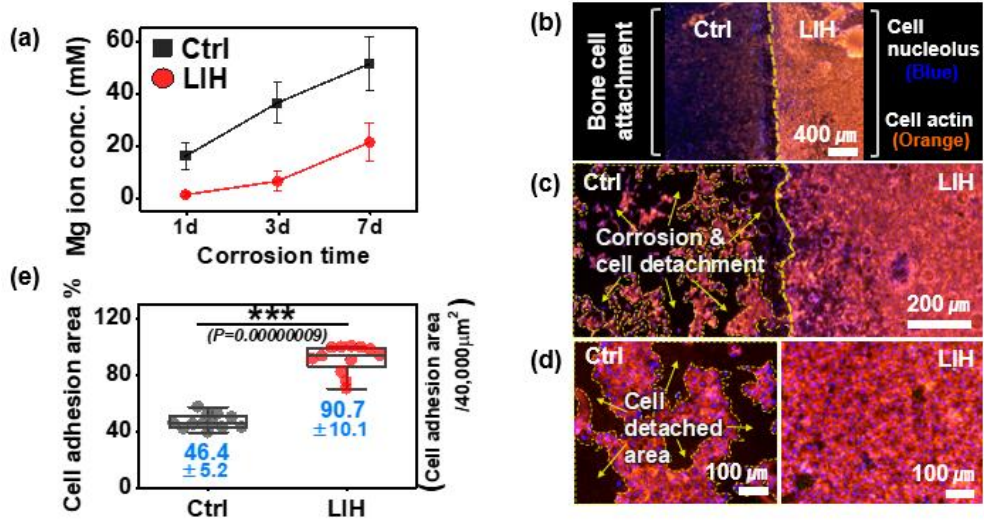


Fig.4.14 (a) The amount of released Mg ion after corrosion test at 1,3, and 7 days. (b-d) Comparison of cell adhesion at each area; cell nucleolus indicated blue, and actin indicated orange. (e) The analysis of cell adhesion area by calculating image processing.

4.4 Conclusion

In this study, a simple, quick, and one-step coating technology (LISSC) was developed to coat physicochemical HAp on the surface of Mg in a liquid precursor environment. The laser-treated surface was modified through the nucleation and growth of HAp on the surface of Mg in a short time such that the coating material adheres tightly without pretreatment or chemicals. The enhanced coating ability led to improved adhesion strength, which resulted in increased resistance to corrosion and functional properties such as biocompatibility and rapid coating recovery. This technology with liquid precursors can be applied to a variety of medical device fields such as orthopedic and dental applications without limitations on the shape of the device. Furthermore, it could be utilized to apply different coating materials on any substrate by modifying the laser conditions and the composition of the liquid precursor.

Chapter 5. Conclusion

Magnesium (Mg) alloy is attracting attention as an orthopedic material because it has properties similar to bone compared to existing biomaterials and is decomposed in the human body while promoting bone formation after plantation. However, the corrosion rate of magnesium alloys is accelerated in body fluids rich in chlorinated compounds. In particular, rapid hydrogen gas and pH changes occurring in the early stages of reaction have the potential to cause excessive inflammatory reactions and fibrosis of surrounding tissues. In order to control the initial corrosion rate of the magnesium alloy, research on various coating technologies is being actively conducted, but there are problems to be solved in the method using the coating, such as the stability of the coating layer.

Laser surface modification has been used in many applications because non-contact processing is possible in a general process atmosphere. Selective processing on local regions and various processing effects can be expected according to the pulse width or wavelength of the laser. Therefore, in this study, the initial corrosion rate control and biocompatibility of Mg alloys were improved through surface treatment using laser and advanced coating techniques to overcome the shortcomings of the coating technique and improve performance.

First, the optimum conditions for suppressing corrosion were studied by applying various femtosecond (fs) laser conditions. To check the initial corrosion rate, the amount of Mg ion elution was investigated depending on each condition in the Hanks' balanced salt solution (HBSS). The surface and phase changes were observed using scanning electron microscopy (SEM) and X-ray diffraction analysis (XRD). Galvanic corrosion, which is a typical corrosion mechanism in metal alloys, was reduced through a solid solution of the secondary phase using laser surface melting with the minimum region.

Second, by using the effect of the fs laser surface texturing, the Mg surface was modified to have super-hydrophilic properties, and through this, the polymer coating ability was improved for controlling the corrosion rate. A series of experiments were carried out by spin-coating a biodegradable high molecular compound, poly-lactic-co-glycolic acid (PLGA), under the same conditions, on the Mg groups. As a result of checking the Mg elution amount after immersion corrosion in the media solution, it was confirmed that the amount of Mg ions was decreased in the laser textured group compared to the bare Mg group. The cross-sectional results after corrosion also showed a consistent result. In particular, by measuring the cell adhesion, it was proved that the biocompatibility of the laser-modified group was improved more effectively than the non-coated group.

Third, through laser treatment in a precursor solution containing hydroxyapatite (HAp), a mineral component of bone, it was possible to synthesize and coat the coating material at the same time. In addition to the advantages of the process, the coating ability was improved compared to the conventional dip coating method, following demonstration using various analyses. The possibility of application in the medical field was confirmed by applying this coating method to products used as implant screws. The laser-induced coating layer can withstand a scratch load and has improved corrosion resistance in long-term corrosion tests.

In the future, based on the above research results, according to the biodegradable product group (eg. screw, plate, scaffold, stent, etc.), the range of application of biodegradable alloys will be further expanded by controlling the corrosion rate. It is expected that the laser process will be effectively performed in various fields where the coating is applied by utilizing surface treatment and in-solution coating methods.

Reference

- [1] S. Bauer, P. Schmuki, K. Von Der Mark, J. Park, Engineering biocompatible implant surfaces: Part I: Materials and surfaces, *Progress in Materials Science* 58(3) (2013) 261-326.
- [2] M.P. Staiger, A.M. Pietak, J. Huadmai, G. Dias, Magnesium and its alloys as orthopedic biomaterials: a review, *Biomaterials* 27(9) (2006) 1728-1734.
- [3] H.F. Hildebrand, C. Veron, P. Martin, Nickel, chromium, cobalt dental alloys and allergic reactions: an overview, *Biomaterials* 10(8) (1989) 545-548.
- [4] F. Barrere, T. Mahmood, K. De Groot, C. Van Blitterswijk, Advanced biomaterials for skeletal tissue regeneration: Instructive and smart functions, *Materials Science and Engineering: R: Reports* 59(1-6) (2008) 38-71.
- [5] Y.F. Zheng, X.N. Gu, F. Witte, Biodegradable metals, *Materials Science and Engineering: R: Reports* 77 (2014) 1-34.
- [6] F. Witte, A. Eliezer, Biodegradable metals, *Degradation of implant materials*, Springer2012, pp. 93-109.
- [7] S.V. Dorozhkin, Calcium orthophosphate coatings on magnesium and its biodegradable alloys, *Acta Biomater* 10(7) (2014) 2919-34.
- [8] H.-S. Han, S. Loffredo, I. Jun, J. Edwards, Y.-C. Kim, H.-K. Seok, F. Witte, D. Mantovani, S. Glyn-Jones, Current status and outlook on the clinical translation of biodegradable metals, *Materials Today* 23 (2019) 57-71.
- [9] S. Virtanen, Biodegradable Mg and Mg alloys: Corrosion and biocompatibility, *Materials Science and Engineering: B* 176(20) (2011) 1600-1608.
- [10] M.M. Jamel, M.M. Jamel, H.F. Lopez, Designing advanced biomedical

biodegradable Mg alloys: a review, *Metals* 12(1) (2022) 85.

[11] M. Uddin, C. Hall, P. Murphy, Surface treatments for controlling corrosion rate of biodegradable Mg and Mg-based alloy implants, *Science and technology of advanced materials* (2015).

[12] M. Ascencio, M. Pekguleryuz, S. Omanovic, An investigation of the corrosion mechanisms of WE43 Mg alloy in a modified simulated body fluid solution: The effect of electrolyte renewal, *Corrosion Science* 91 (2015) 297-310.

[13] Y. Sun, B. Zhang, Y. Wang, L. Geng, X. Jiao, Preparation and characterization of a new biomedical Mg–Zn–Ca alloy, *Materials & Design* 34 (2012) 58-64.

[14] K. Ralston, N. Birbilis, M. Weyland, C. Hutchinson, The effect of precipitate size on the yield strength-pitting corrosion correlation in Al–Cu–Mg alloys, *Acta Materialia* 58(18) (2010) 5941-5948.

[15] S. Agarwal, J. Curtin, B. Duffy, S. Jaiswal, Biodegradable magnesium alloys for orthopaedic applications: A review on corrosion, biocompatibility and surface modifications, *Materials Science and Engineering: C* 68 (2016) 948-963.

[16] M. Ali, M. Elsherif, A.E. Salih, A. Ul-Hamid, M. Hussein, S. Park, A.K. Yetisen, H. Butt, Surface modification and cytotoxicity of Mg-based bio-alloys: An overview of recent advances, *Journal of Alloys and Compounds* 825 (2020) 154140.

[17] J. Yang, F. Cui, I.S. Lee, Surface modifications of magnesium alloys for biomedical applications, *Annals of biomedical engineering* 39(7) (2011) 1857-1871.

[18] P. Wan, L. Tan, K. Yang, Surface modification on biodegradable magnesium alloys as orthopedic implant materials to improve the bio-adaptability: a review, *Journal of Materials Science & Technology* 32(9) (2016) 827-834.

- [19] C. Shuai, C. He, L. Xu, Q. Li, T. Chen, Y. Yang, S. Peng, Wrapping effect of secondary phases on the grains: increased corrosion resistance of Mg–Al alloys, *Virtual and Physical Prototyping* 13(4) (2018) 292-300.
- [20] S.R. Paital, A. Bhattacharya, M. Moncayo, Y.H. Ho, K. Mahdak, S. Nag, R. Banerjee, N.B. Dahotre, Improved corrosion and wear resistance of Mg alloys via laser surface modification of Al on AZ31B, *Surface and Coatings Technology* 206(8) (2012) 2308-2315.
- [21] A. Kurella, N.B. Dahotre, Review paper: surface modification for bioimplants: the role of laser surface engineering, *J Biomater Appl* 20(1) (2005) 5-50.
- [22] J. Dutta Majumdar, I. Manna, Laser processing of materials, *Sadhana* 28(3) (2003) 495-562.
- [23] B. Vrancken, L. Thijs, J.-P. Kruth, J. Van Humbeeck, Heat treatment of Ti6Al4V produced by Selective Laser Melting: Microstructure and mechanical properties, *Journal of Alloys and Compounds* 541 (2012) 177-185.
- [24] G.N. Levy, The role and future of the laser technology in the additive manufacturing environment, *Physics Procedia* 5 (2010) 65-80.
- [25] J.P. Kruth, G. Levy, F. Klocke, T.H.C. Childs, Consolidation phenomena in laser and powder-bed based layered manufacturing, *CIRP Annals* 56(2) (2007) 730-759.
- [26] C. Liu, J. Liang, J. Zhou, L. Wang, Q. Li, Effect of laser surface melting on microstructure and corrosion characteristics of AM60B magnesium alloy, *Applied Surface Science* 343 (2015) 133-140.
- [27] A.K. Mondal, S. Kumar, C. Blawert, N.B. Dahotre, Effect of laser surface treatment on corrosion and wear resistance of ACM720 Mg alloy, *Surface and Coatings Technology* 202(14) (2008) 3187-3198.
- [28] C. Taltavull, B. Torres, A. López, P. Rodrigo, E. Otero, J. Rams, Selective laser surface melting of a magnesium-aluminium alloy, *Materials*

Letters 85 (2012) 98-101.

[29] G. Abbas, Z. Liu, P. Skeldon, Corrosion behaviour of laser-melted magnesium alloys, *Applied Surface Science* 247(1-4) (2005) 347-353.

[30] W. Khalfaoui, E. Valerio, J.E. Masse, M. Autric, Excimer laser treatment of ZE41 magnesium alloy for corrosion resistance and microhardness improvement, *Optics and Lasers in Engineering* 48(9) (2010) 926-931.

[31] L. Guo, T. Yue, H. Man, Excimer laser surface treatment of magnesium alloy WE43 for corrosion resistance improvement, *Journal of materials science* 40(13) (2005) 3531-3533.

[32] W. Pacquentin, N. Caron, R. Oltra, Nanosecond laser surface modification of AISI 304L stainless steel: Influence the beam overlap on pitting corrosion resistance, *Applied Surface Science* 288 (2014) 34-39.

[33] J.G. Hoekstra, S.B. Qadri, J.R. Scully, J.M. Fitz-Gerald, Laser Surface Modification of a Crystalline Al-Co-Ce Alloy for Enhanced Corrosion Resistance, *Advanced engineering materials* 7(9) (2005) 805-809.

[34] A. Coy, F. Viejo, F. Garcia-Garcia, Z. Liu, P. Skeldon, G. Thompson, Effect of excimer laser surface melting on the microstructure and corrosion performance of the die cast AZ91D magnesium alloy, *Corrosion Science* 52(2) (2010) 387-397.

[35] S. Ha, S.-J. Kim, S. Hong, C.-D. Yim, D.-I. Kim, J. Suh, K.H. Oh, H.N. Han, Improvement of ductility in magnesium alloy sheet using laser scanning treatment, *Materials Letters* 64(3) (2010) 425-427.

[36] M. Kulka, A. Pertek, Microstructure and properties of borided 41Cr4 steel after laser surface modification with re-melting, *Applied Surface Science* 214(1) (2003) 278-288.

[37] B. Yilbas, M. Khaled, N. Abu-Dheir, N. Aqeeli, S. Furquan, Laser texturing of alumina surface for improved hydrophobicity, *Applied surface science* 286 (2013) 161-170.

- [38] A.G. Demir, P. Maressa, B. Previtali, Fibre laser texturing for surface functionalization, *Physics Procedia* 41 (2013) 759-768.
- [39] A.O. Ijaola, E.A. Bamidele, C.J. Akisin, I.T. Bello, A.T. Oyatobo, A. Abdulkareem, P.K. Farayibi, E. Asmatulu, Wettability transition for laser textured surfaces: a comprehensive review, *Surfaces and Interfaces* 21 (2020) 100802.
- [40] A.Y. Vorobyev, C. Guo, Direct femtosecond laser surface nano/microstructuring and its applications, *Laser & Photonics Reviews* 7(3) (2013) 385-407.
- [41] A.A. Ionin, S.I. Kudryashov, S.V. Makarov, A.A. Rudenko, L.V. Seleznev, D.V. Sinitsyn, E.V. Golosov, Y.R. Kolobov, A.E. Ligachev, Beam spatial profile effect on femtosecond laser surface structuring of titanium in scanning regime, *Applied Surface Science* 284 (2013) 634-637.
- [42] A.Y. Vorobyev, C. Guo, Femtosecond laser structuring of titanium implants, *Applied Surface Science* 253(17) (2007) 7272-7280.
- [43] K.M.T. Ahmmed, E.J.Y. Ling, P. Servio, A.-M. Kietzig, Introducing a new optimization tool for femtosecond laser-induced surface texturing on titanium, stainless steel, aluminum and copper, *Optics and Lasers in Engineering* 66 (2015) 258-268.
- [44] D. Kam, S. Bhattacharya, J. Mazumder, Control of the wetting properties of an AISI 316L stainless steel surface by femtosecond laser-induced surface modification, *Journal of micromechanics and microengineering* 22(10) (2012) 105019.
- [45] A. Gokhan Demir, V. Furlan, N. Lecis, B. Previtali, Laser surface structuring of AZ31 Mg alloy for controlled wettability, *Biointerphases* 9(2) (2014) 029009.
- [46] V. Zorba, L. Persano, D. Pisignano, A. Athanassiou, E. Stratakis, R. Cingolani, P. Tzanetakis, C. Fotakis, Making silicon hydrophobic: wettability control by two-lengthscale simultaneous patterning with

- femtosecond laser irradiation, *Nanotechnology* 17(13) (2006) 3234.
- [47] A.G. Demir, T.B. Taketa, R. Tolouei, V. Furlan, C. Paternoster, M.M. Beppu, D. Mantovani, B. Previtali, Laser surface structuring affects polymer deposition, coating homogeneity, and degradation rate of Mg alloys, *Materials Letters* 160 (2015) 359-362.
- [48] L. Hirt, A. Reiser, R. Spolenak, T. Zambelli, Additive Manufacturing of Metal Structures at the Micrometer Scale, *Adv Mater* 29(17) (2017).
- [49] Y. Chen, S.F. Hung, W.K. Lo, Y. Chen, Y. Shen, K. Kafenda, J. Su, K. Xia, S. Yang, A universal method for depositing patterned materials in situ, *Nature communications* 11(1) (2020) 1-8.
- [50] L.D. Zarzar, B.S. Swartzentruber, B.F. Donovan, P.E. Hopkins, B. Kaehr, Using Laser-Induced Thermal Voxels to Pattern Diverse Materials at the Solid-Liquid Interface, *ACS Appl Mater Interfaces* 8(33) (2016) 21134-9.
- [51] E. Edri, N. Armon, E. Greenberg, S. Moshe-Tsurel, D. Lubotzky, T. Salzillo, I. Perelshtein, M. Tkachev, O. Girshevitz, H. Shpaisman, Laser Printing of Multilayered Alternately Conducting and Insulating Microstructures, *ACS applied materials & interfaces* 13(30) (2021) 36416-36425.
- [52] J.X. Yang, B.H. Dai, C.Y. Chiang, I.C. Chiu, C.W. Pao, S.Y. Lu, I.Y. Tsao, S.T. Lin, C.T. Chiu, J.W. Yeh, P.C. Chang, W.H. Hung, Rapid Fabrication of High-Entropy Ceramic Nanomaterials for Catalytic Reactions, *ACS Nano* (2021).
- [53] L. Pramatarova, E. Pecheva, T. Petrov, A. Kondyurin, R. Pramatarova, N. Minkovski, Ion beam and laser processing for hydroxyapatite formation, *Vacuum* 76(2-3) (2004) 339-342.
- [54] L. Pramatarova, E. Pecheva, D. Dimova-Malinovska, R. Pramatarova, U. Bismayer, T. Petrov, N. Minkovski, Porous silicon as a substrate for hydroxyapatite growth, *Vacuum* 76(2-3) (2004) 135-138.
- [55] L. Pramatarova, E. Pecheva, R. Presker, M. Pham, M. Maitz, M.

Stutzmann, Hydroxyapatite growth induced by native extracellular matrix deposition on solid surfaces, *Eur Cell Mater* 9 (2005) 9.

[56] C.M. Jin, W. Lee, D. Kim, T. Kang, I. Choi, Photothermal Convection Lithography for Rapid and Direct Assembly of Colloidal Plasmonic Nanoparticles on Generic Substrates, *Small* 14(45) (2018) e1803055.

[57] H.-G. Kim, M.S. Park, Circuit patterning using laser on transparent material, *Surface and Coatings Technology* 315 (2017) 377-384.

[58] A. Ishikawa, T. Tanaka, S. Kawata, Improvement in the reduction of silver ions in aqueous solution using two-photon sensitive dye, *Applied Physics Letters* 89(11) (2006).

[59] X. Zeng, C. Chen, S. Zheng, S. Weng, L. Chen, Y. Yuan, J. Dong, Z. Hu, M. Li, Corrigendum: Rapid in situ synthesis of silver nanoparticles on the distal facet of a fiber by laser-induced photo-reduction (2014 *Laser Phys. Lett.* 11 016003), *Laser Physics Letters* 11(11) (2014).

[60] A. Oyane, M. Nakamura, I. Sakamaki, Y. Shimizu, S. Miyata, H. Miyaji, Laser-assisted wet coating of calcium phosphate for surface-functionalization of PEEK, *PLoS One* 13(10) (2018) e0206524.

[61] A. Oyane, N. Saito, I. Sakamaki, K. Koga, M. Nakamura, A.J. Nathanael, N. Yoshizawa, K. Shitomi, K. Mayumi, H. Miyaji, Laser-assisted biomineralization on human dentin for tooth surface functionalization, *Mater Sci Eng C Mater Biol Appl* 105 (2019) 110061.

[62] B.H. Lee, A. Oyane, H. Tsurushima, Y. Shimizu, T. Sasaki, N. Koshizaki, A new approach for hydroxyapatite coating on polymeric materials using laser-induced precursor formation and subsequent aging, *ACS Appl Mater Interfaces* 1(7) (2009) 1520-4.

[63] A. Oyane, N. Matsuoka, K. Koga, Y. Shimizu, M. Nakamura, K. Kawaguchi, N. Koshizaki, Y. Sogo, A. Ito, H. Unuma, Laser-assisted biomimetic process for surface functionalization of titanium metal, *Colloids and Interface Science Communications* 4 (2015) 5-9.

- [64] R. Zeng, W. Dietzel, F. Witte, N. Hort, C. Blawert, Progress and challenge for magnesium alloys as biomaterials, *Advanced Engineering Materials* 10(8) (2008).
- [65] G. Song, Control of biodegradation of biocompatible magnesium alloys, *Corrosion Science* 49(4) (2007) 1696-1701.
- [66] T. Lei, W. Tang, S.-H. Cai, F.-F. Feng, N.-F. Li, On the corrosion behaviour of newly developed biodegradable Mg-based metal matrix composites produced by in situ reaction, *Corrosion Science* 54 (2012) 270-277.
- [67] S. Zhang, J. Li, Y. Song, C. Zhao, X. Zhang, C. Xie, Y. Zhang, H. Tao, Y. He, Y. Jiang, In vitro degradation, hemolysis and MC3T3-E1 cell adhesion of biodegradable Mg-Zn alloy, *Materials Science and Engineering: C* 29(6) (2009) 1907-1912.
- [68] S. Zhang, X. Zhang, C. Zhao, J. Li, Y. Song, C. Xie, H. Tao, Y. Zhang, Y. He, Y. Jiang, Research on an Mg-Zn alloy as a degradable biomaterial, *Acta biomaterialia* 6(2) (2010) 626-640.
- [69] Y. Song, E.-H. Han, D. Shan, C.D. Yim, B.S. You, The effect of Zn concentration on the corrosion behavior of Mg-xZn alloys, *Corrosion Science* 65 (2012) 322-330.
- [70] N. Eliaz, *Degradation of implant materials*, Springer Science & Business Media 2012.
- [71] H. Hermawan, D. Dubé, D. Mantovani, Developments in metallic biodegradable stents, *Acta biomaterialia* 6(5) (2010) 1693-1697.
- [72] A.C. Hänzi, I. Gerber, M. Schinhammer, J.F. Löffler, P.J. Uggowitzer, On the in vitro and in vivo degradation performance and biological response of new biodegradable Mg-Y-Zn alloys, *Acta biomaterialia* 6(5) (2010) 1824-1833.
- [73] P.-R. Cha, H.-S. Han, G.-F. Yang, Y.-C. Kim, K.-H. Hong, S.-C. Lee, J.-Y. Jung, J.-P. Ahn, Y.-Y. Kim, S.-Y. Cho, Biodegradability engineering of

biodegradable Mg alloys: Tailoring the electrochemical properties and microstructure of constituent phases, *Scientific reports* 3 (2013).

[74] X. Gu, N. Li, W. Zhou, Y. Zheng, X. Zhao, Q. Cai, L. Ruan, Corrosion resistance and surface biocompatibility of a microarc oxidation coating on a Mg–Ca alloy, *Acta Biomaterialia* 7(4) (2011) 1880-1889.

[75] C. Liu, Y. Wang, R. Zeng, X. Zhang, W. Huang, P. Chu, In vitro corrosion degradation behaviour of Mg–Ca alloy in the presence of albumin, *Corrosion Science* 52(10) (2010) 3341-3347.

[76] Y. Jeong, W. Kim, Enhancement of mechanical properties and corrosion resistance of Mg–Ca alloys through microstructural refinement by indirect extrusion, *Corrosion Science* 82 (2014) 392-403.

[77] G. Song, A. Atrens, X. Wu, B. Zhang, Corrosion behaviour of AZ21, AZ501 and AZ91 in sodium chloride, *Corrosion science* 40(10) (1998) 1769-1791.

[78] G.L. Song, A. Atrens, Corrosion mechanisms of magnesium alloys, *Advanced engineering materials* 1(1) (1999) 11-33.

[79] S.A. Khan, Y. Miyashita, Y. Mutoh, Z.B. Sajuri, Influence of Mn content on mechanical properties and fatigue behavior of extruded Mg alloys, *Materials Science and Engineering: A* 420(1) (2006) 315-321.

[80] M. Yamasaki, N. Hayashi, S. Izumi, Y. Kawamura, Corrosion behavior of rapidly solidified Mg–Zn–rare earth element alloys in NaCl solution, *Corrosion Science* 49(1) (2007) 255-262.

[81] J. Chang, X. Guo, S. He, P. Fu, L. Peng, W. Ding, Investigation of the corrosion for Mg–xGd–3Y–0.4 Zr (x= 6, 8, 10, 12wt%) alloys in a peak-aged condition, *Corrosion Science* 50(1) (2008) 166-177.

[82] M.-C. Zhao, M. Liu, G. Song, A. Atrens, Influence of the β -phase morphology on the corrosion of the Mg alloy AZ91, *Corrosion Science* 50(7) (2008) 1939-1953.

[83] Q. Wang, L. Tan, W. Xu, B. Zhang, K. Yang, Dynamic behaviors of a

Ca–P coated AZ31B magnesium alloy during in vitro and in vivo degradations, *Materials Science and Engineering: B* 176(20) (2011) 1718-1726.

[84] F. Witte, J. Fischer, J. Nellesen, C. Vogt, J. Vogt, T. Donath, F. Beckmann, In vivo corrosion and corrosion protection of magnesium alloy LAE442, *Acta biomaterialia* 6(5) (2010) 1792-1799.

[85] Y. Song, S. Zhang, J. Li, C. Zhao, X. Zhang, Electrodeposition of Ca–P coatings on biodegradable Mg alloy: in vitro biomineralization behavior, *Acta Biomaterialia* 6(5) (2010) 1736-1742.

[86] J. Hu, C. Zhang, B. Cui, K. Bai, S. Guan, L. Wang, S. Zhu, In vitro degradation of AZ31 magnesium alloy coated with nano TiO₂ film by sol–gel method, *Applied Surface Science* 257(21) (2011) 8772-8777.

[87] A. Zomorodian, F. Brusciotti, A. Fernandes, M. Carmezim, T.M. e Silva, J. Fernandes, M. Montemor, Anti-corrosion performance of a new silane coating for corrosion protection of AZ31 magnesium alloy in Hank's solution, *Surface and coatings technology* 206(21) (2012) 4368-4375.

[88] P. Volovitch, J. Masse, A. Fabre, L. Barrallier, W. Saikaly, Microstructure and corrosion resistance of magnesium alloy ZE41 with laser surface cladding by Al–Si powder, *Surface and Coatings Technology* 202(20) (2008) 4901-4914.

[89] S. Ignat, P. Sallamand, D. Grevey, M. Lambertin, Magnesium alloys (WE43 and ZE41) characterisation for laser applications, *Applied Surface Science* 233(1) (2004) 382-391.

[90] M. Hazra, A. Mondal, S. Kumar, C. Blawert, N.B. Dahotre, Laser surface cladding of MRI 153M magnesium alloy with (Al+ Al₂O₃), *Surface and Coatings Technology* 203(16) (2009) 2292-2299.

[91] Y. Gao, C. Wang, Q. Lin, H. Liu, M. Yao, Broad-beam laser cladding of Al–Si alloy coating on AZ91HP magnesium alloy, *Surface and Coatings Technology* 201(6) (2006) 2701-2706.

- [92] J.D. Majumdar, I. Manna, Mechanical properties of a laser-surface-alloyed magnesium-based alloy (AZ91) with nickel, *Scripta Materialia* 62(8) (2010) 579-581.
- [93] L. Zhang, Y. Zhang, J. Lu, F. Dai, A. Feng, K. Luo, J. Zhong, Q. Wang, M. Luo, H. Qi, Effects of laser shock processing on electrochemical corrosion resistance of ANSI 304 stainless steel weldments after cavitation erosion, *Corrosion Science* 66 (2013) 5-13.
- [94] U. Trdan, M. Skarba, J. Grum, Laser shock peening effect on the dislocation transitions and grain refinement of Al–Mg–Si alloy, *Materials Characterization* 97 (2014) 57-68.
- [95] U. Trdan, J. Grum, SEM/EDS characterization of laser shock peening effect on localized corrosion of Al alloy in a near natural chloride environment, *Corrosion Science* 82 (2014) 328-338.
- [96] A. Gökhan Demir, V. Furlan, N. Lecis, B. Previtali, Laser surface structuring of AZ31 Mg alloy for controlled wettability, *Biointerphases* 9(2) (2014) 029009.
- [97] L. Wang, J. Zhou, J. Liang, J. Chen, Microstructure and corrosion behavior of plasma electrolytic oxidation coated magnesium alloy pre-treated by laser surface melting, *Surface and Coatings Technology* 206(13) (2012) 3109-3115.
- [98] J.-P. Kruth, G. Levy, F. Klocke, T. Childs, Consolidation phenomena in laser and powder-bed based layered manufacturing, *CIRP Annals-Manufacturing Technology* 56(2) (2007) 730-759.
- [99] J.D. Majumdar, R. Galun, B. Mordike, I. Manna, Effect of laser surface melting on corrosion and wear resistance of a commercial magnesium alloy, *Materials Science and Engineering: A* 361(1) (2003) 119-129.
- [100] A. Mondal, S. Kumar, C. Blawert, N.B. Dahotre, Effect of laser surface treatment on corrosion and wear resistance of ACM720 Mg alloy, *Surface and Coatings Technology* 202(14) (2008) 3187-3198.

- [101] S. Liu, J. Hu, Y. Yang, Z. Guo, H. Wang, Microstructure analysis of magnesium alloy melted by laser irradiation, *Applied surface science* 252(5) (2005) 1723-1731.
- [102] G. Abbas, Z. Liu, P. Skeldon, Corrosion behaviour of laser-melted magnesium alloys, *Applied Surface Science* 247(1) (2005) 347-353.
- [103] K.-H. Leitz, B. Redlingshöfer, Y. Reg, A. Otto, M. Schmidt, Metal Ablation with Short and Ultrashort Laser Pulses, *Physics Procedia* 12 (2011) 230-238.
- [104] T. Kurita, K. Komatsuzaki, M. Hattori, Advanced material processing with nano-and femto-second pulsed laser, *International journal of machine tools and manufacture* 48(2) (2008) 220-227.
- [105] J. Krüger, W. Kautek, The femtosecond pulse laser: a new tool for micromachining, *LASER PHYSICS-LAWRENCE- 9* (1999) 30-40.
- [106] J.-W. Lee, H.-S. Han, K.-J. Han, J. Park, H. Jeon, M.-R. Ok, H.-K. Seok, J.-P. Ahn, K.E. Lee, D.-H. Lee, Long-term clinical study and multiscale analysis of in vivo biodegradation mechanism of Mg alloy, *Proceedings of the National Academy of Sciences* 113(3) (2016) 716-721.
- [107] A. Ionin, S. Kudryashov, S. Makarov, A. Rudenko, L. Seleznev, D. Sinitsyn, E. Golosov, Y.R. Kolobov, A. Ligachev, Beam spatial profile effect on femtosecond laser surface structuring of titanium in scanning regime, *Applied surface science* 284 (2013) 634-637.
- [108] C.H. Crouch, J.E. Carey, J.M. Warrender, M.J. Aziz, E. Mazur, F.Y. Génin, Comparison of structure and properties of femtosecond and nanosecond laser-structured silicon, *Applied Physics Letters* 84(11) (2004) 1850-1852.
- [109] K. Wei, Z. Wang, X. Zeng, Influence of element vaporization on formability, composition, microstructure, and mechanical performance of the selective laser melted Mg–Zn–Zr components, *Materials Letters* 156 (2015) 187-190.

[110] C.S. Barrett, Structure of metals, McGraw-Hill Book Company, Inc.; New York 1943.

[111] D. Zhao, F. Witte, F. Lu, J. Wang, J. Li, L. Qin, Current status on clinical applications of magnesium-based orthopaedic implants: A review from clinical translational perspective, *Biomaterials* 112 (2017) 287-302.

[112] A. Ewald, D. Kreczy, T. Brückner, U. Gbureck, M. Bengel, A. Hoess, B. Nies, J. Bator, U. Klammert, A. Fuchs, Development and bone regeneration capacity of premixed magnesium phosphate cement pastes, *Materials* 12(13) (2019) 2119.

[113] S. Yin, W. Duan, W. Liu, L. Wu, J. Yu, Z. Zhao, M. Liu, P. Wang, J. Cui, Z. Zhang, Influence of specific second phases on corrosion behaviors of Mg-Zn-Gd-Zr alloys, *Corrosion Science* 166 (2020) 108419.

[114] A. Pardo, M. Merino, A. Coy, F. Viejo, R. Arrabal, S. Feliú Jr, Influence of microstructure and composition on the corrosion behaviour of Mg/Al alloys in chloride media, *Electrochimica Acta* 53(27) (2008) 7890-7902.

[115] X. Gu, Y. Zheng, S. Zhong, T. Xi, J. Wang, W. Wang, Corrosion of, and cellular responses to Mg-Zn-Ca bulk metallic glasses, *Biomaterials* 31(6) (2010) 1093-1103.

[116] A.K. Blakney, F.I. Simonovsky, I.T. Suydam, B.D. Ratner, K.A. Woodrow, Rapidly biodegrading PLGA-polyurethane fibers for sustained release of physicochemically diverse drugs, *ACS biomaterials science & engineering* 2(9) (2016) 1595-1607.

[117] O.A. Sindeeva, O.I. Gusliakova, O.A. Inozemtseva, A.S. Abdurashitov, E.P. Brodovskaya, M. Gai, V.V. Tuchin, D.A. Gorin, G.B. Sukhorukov, Effect of a Controlled Release of Epinephrine Hydrochloride from PLGA Microchamber Array: In Vivo Studies, *ACS applied materials & interfaces* 10(44) (2018) 37855-37864.

[118] M. Hussain, J. Xie, Z. Hou, K. Shezad, J. Xu, K. Wang, Y. Gao, L.

- Shen, J. Zhu, Regulation of drug release by tuning surface textures of biodegradable polymer microparticles, *ACS applied materials & interfaces* 9(16) (2017) 14391-14400.
- [119] Y. Chen, Y. Song, S. Zhang, J. Li, C. Zhao, X. Zhang, Interaction between a high purity magnesium surface and PCL and PLA coatings during dynamic degradation, *Biomedical Materials* 6(2) (2011) 025005.
- [120] J. Gao, X. Shi, B. Yang, S. Hou, E. Meng, F. Guan, S. Guan, Fabrication and characterization of bioactive composite coatings on Mg–Zn–Ca alloy by MAO/sol–gel, *Journal of Materials Science: Materials in Medicine* 22(7) (2011) 1681-1687.
- [121] X. Xu, P. Lu, M. Guo, M. Fang, Cross-linked gelatin/nanoparticles composite coating on micro-arc oxidation film for corrosion and drug release, *Applied surface science* 256(8) (2010) 2367-2371.
- [122] W. Ng, M. Wong, F. Cheng, Stearic acid coating on magnesium for enhancing corrosion resistance in Hanks' solution, *Surface and Coatings Technology* 204(11) (2010) 1823-1830.
- [123] M. Golda-Cepa, A. Chorylek, P. Chytrosz, M. Brzychczy-Wloch, J. Jaworska, J. Kasperczyk, M. Hakkarainen, K. Engvall, A. Kotarba, Multifunctional PLGA/Parylene C coating for implant materials: An integral approach for biointerface optimization, *ACS applied materials & interfaces* 8(34) (2016) 22093-22105.
- [124] J.D. Majumdar, I. Manna, Laser processing of materials, *Sadhana* 28(3-4) (2003) 495-562.
- [125] M. Godec, B. Podgornik, D. Nolan, Microstructural Development in a Laser-Remelted Al-Zn-Si-Mg Coating, *Scientific Reports* 7(1) (2017) 1-7.
- [126] Z. Xu, U. Eduok, J. Szpunar, Effect of annealing temperature on the corrosion resistance of MgO coatings on Mg alloy, *Surface and Coatings Technology* 357 (2019) 691-697.
- [127] U. Eduok, Z. Xu, J. Szpunar, Fabricating protective silica/PMDS

composite films for Mg alloy: Correlating bulk silica reinforcement with barrier performance, *Journal of Non-Crystalline Solids* 485 (2018) 47-56.

[128] A. Riquelme, P. Rodrigo, M.D. Escalera-Rodríguez, J. Rams, Characterisation and mechanical properties of Al/SiC metal matrix composite coatings formed on ZE41 magnesium alloys by laser cladding, *Results in Physics* 13 (2019) 102160.

[129] K. Huang, X. Lin, C. Xie, T. Yue, Laser cladding of Zr-based coating on AZ91D magnesium alloy for improvement of wear and corrosion resistance, *Bulletin of Materials Science* 36(1) (2013) 99-105.

[130] K.T. Ahmmed, E.J.Y. Ling, P. Servio, A.-M. Kietzig, Introducing a new optimization tool for femtosecond laser-induced surface texturing on titanium, stainless steel, aluminum and copper, *Optics and Lasers in Engineering* 66 (2015) 258-268.

[131] A. Vorobyev, C. Guo, Femtosecond laser structuring of titanium implants, *Applied surface science* 253(17) (2007) 7272-7280.

[132] N.J. Ostrowski, B. Lee, A. Roy, M. Ramanathan, P.N. Kumta, Biodegradable poly (lactide-co-glycolide) coatings on magnesium alloys for orthopedic applications, *Journal of Materials Science: Materials in Medicine* 24(1) (2013) 85-96.

[133] J.-K. Jeon, H. Seo, J. Park, S.J. Son, Y.R. Kim, E.S. Kim, J.W. Park, W.-G. Jung, H. Jeon, Y.-C. Kim, Conceptual Study for Tissue-Regenerative Biodegradable Magnesium Implant Integrated with Nitric Oxide-Releasing Nanofibers, *Metals and Materials International* (2019) 1-10.

[134] J. Park, H.-S. Han, J. Park, H. Seo, J. Edwards, Y.-C. Kim, M.-R. Ok, H.-K. Seok, H. Jeon, Corrosion behavior of biodegradable Mg-based alloys via femtosecond laser surface melting, *Applied Surface Science* 448 (2018) 424-434.

[135] H.K. Kim, H.S. Han, K.S. Lee, D.H. Lee, J.W. Lee, H. Jeon, S.Y. Cho, H.J. Roh, Y.C. Kim, H.K. Seok, Comprehensive study on the roles of

released ions from biodegradable mg–5 wt% ca–1 wt% Zn alloy in bone regeneration, *Journal of tissue engineering and regenerative medicine* 11(10) (2017) 2710-2724.

[136] J. Wang, F. Witte, T. Xi, Y. Zheng, K. Yang, Y. Yang, D. Zhao, J. Meng, Y. Li, W. Li, Recommendation for modifying current cytotoxicity testing standards for biodegradable magnesium-based materials, *Acta biomaterialia* 21 (2015) 237-249.

[137] R.N. Wenzel, Resistance of solid surfaces to wetting by water, *Industrial & Engineering Chemistry* 28(8) (1936) 988-994.

[138] R.N. Wenzel, Surface roughness and contact angle, *The Journal of Physical Chemistry* 53(9) (1949) 1466-1467.

[139] R.-G. Hu, S. Zhang, J.-F. Bu, C.-J. Lin, G.-L. Song, Recent progress in corrosion protection of magnesium alloys by organic coatings, *Progress in Organic Coatings* 73(2-3) (2012) 129-141.

[140] M. Tahara, N. Cuong, Y. Nakashima, Improvement in adhesion of polyethylene by glow-discharge plasma, *Surface and coatings Technology* 174 (2003) 826-830.

[141] A. Baumgärtner, M. Muthukumar, Effects of surface roughness on adsorbed polymers, *The Journal of chemical physics* 94(5) (1991) 4062-4070.

[142] A. Yfantis, I. Paloumpa, D. Schmeißer, D. Yfantis, Novel corrosion-resistant films for Mg alloys, *Surface and Coatings Technology* 151 (2002) 400-404.

[143] K. Rechendorff, M.B. Hovgaard, M. Foss, V.P. Zhdanov, F. Besenbacher, Enhancement of protein adsorption induced by surface roughness, *Langmuir* 22(26) (2006) 10885-10888.

[144] S.V. Dorozhkin, Calcium orthophosphates: occurrence, properties, biomineralization, pathological calcification and biomimetic applications, *Biomatter* 1(2) (2011) 121-164.

- [145] K. De Groot, J. Wolke, J. Jansen, Calcium phosphate coatings for medical implants, *Proceedings of the Institution of Mechanical Engineers, Part H: Journal of Engineering in Medicine* 212(2) (1998) 137-147.
- [146] T. Onoki, T. Hashida, New method for hydroxyapatite coating of titanium by the hydrothermal hot isostatic pressing technique, *Surface and Coatings Technology* 200(24) (2006) 6801-6807.
- [147] T. Kobayashi, S. Itoh, S. Nakamura, M. Nakamura, K. Shinomiya, K. Yamashita, Enhanced bone bonding of hydroxyapatite-coated titanium implants by electrical polarization, *Journal of Biomedical Materials Research Part A* 82(1) (2007) 145-151.
- [148] P. Habibovic, J. Li, C.M. Van Der Valk, G. Meijer, P. Layrolle, C.A. Van Blitterswijk, K. De Groot, Biological performance of uncoated and octacalcium phosphate-coated Ti6Al4V, *Biomaterials* 26(1) (2005) 23-36.
- [149] A. Saithna, The influence of hydroxyapatite coating of external fixator pins on pin loosening and pin track infection: a systematic review, *Injury* 41(2) (2010) 128-132.
- [150] C.-Y. Yang, C.-W. Yang, L.-R. Chen, M.-C. Wu, T.-S. Lui, A. Kuo, T.-M. Lee, Effect of vacuum post-heat treatment of plasma-sprayed hydroxyapatite coatings on their in vitro and in vivo biological responses, *Journal of Medical and Biological Engineering* 29(6) (2009) 296-302.
- [151] D. Liu, K. Savino, M.Z. Yates, Microstructural engineering of hydroxyapatite membranes to enhance proton conductivity, *Advanced Functional Materials* 19(24) (2009) 3941-3947.
- [152] M. Tomozawa, S. Hiromoto, Growth mechanism of hydroxyapatite-coatings formed on pure magnesium and corrosion behavior of the coated magnesium, *Applied Surface Science* 257(19) (2011) 8253-8257.
- [153] S.M. Kim, J.H. Jo, S.M. Lee, M.H. Kang, H.E. Kim, Y. Estrin, J.H. Lee, J.W. Lee, Y.H. Koh, Hydroxyapatite-coated magnesium implants with improved in vitro and in vivo biocorrosion, biocompatibility, and bone

response, *Journal of Biomedical Materials Research Part A: An Official Journal of The Society for Biomaterials, The Japanese Society for Biomaterials, and The Australian Society for Biomaterials and the Korean Society for Biomaterials* 102(2) (2014) 429-441.

[154] J. Waterman, A. Pietak, N. Birbilis, T. Woodfield, G. Dias, M. Staiger, Corrosion resistance of biomimetic calcium phosphate coatings on magnesium due to varying pretreatment time, *Materials Science and Engineering: B* 176(20) (2011) 1756-1760.

[155] K. Baker, J. Drelich, I. Miskioglu, R. Israel, H. Herkowitz, Effect of polyethylene pretreatments on the biomimetic deposition and adhesion of calcium phosphate films, *Acta biomaterialia* 3(3) (2007) 391-401.

[156] S. Saber-Samandari, K. Alamara, S. Saber-Samandari, Calcium phosphate coatings: Morphology, micro-structure and mechanical properties, *Ceramics International* 40(1) (2014) 563-572.

[157] H. Herman, Plasma-sprayed coatings, *Scientific American* 259(3) (1988) 112-117.

[158] P. Fauchais, Understanding plasma spraying, *Journal of Physics D: Applied Physics* 37(9) (2004) R86.

[159] Z. Hong, L. Luan, S.-B. Paik, B. Deng, D.E. Ellis, J.B. Ketterson, A. Mello, J.G. Eon, J. Terra, A. Rossi, Crystalline hydroxyapatite thin films produced at room temperature—an opposing radio frequency magnetron sputtering approach, *Thin Solid Films* 515(17) (2007) 6773-6780.

[160] V.F. Pichugin, R.A. Surmenev, E.V. Shesterikov, M. Ryabtseva, E. Eshenko, S.I. Tverdokhlebov, O. Prymak, M. Epple, The preparation of calcium phosphate coatings on titanium and nickel–titanium by rf-magnetron-sputtered deposition: composition, structure and micromechanical properties, *Surface and Coatings Technology* 202(16) (2008) 3913-3920.

[161] A. Oyane, X. Wang, Y. Sogo, A. Ito, H. Tsurushima, Calcium

phosphate composite layers for surface-mediated gene transfer, *Acta biomaterialia* 8(6) (2012) 2034-2046.

[162] M. Nakamura, A. Oyane, Physicochemical fabrication of calcium phosphate-based thin layers and nanospheres using laser processing in solutions, *Journal of Materials Chemistry B* 4(38) (2016) 6289-6301.

[163] A. Oyane, N. Saito, I. Sakamaki, K. Koga, M. Nakamura, A.J. Nathanael, N. Yoshizawa, K. Shitomi, K. Mayumi, H. Miyaji, Laser-assisted biomineralization on human dentin for tooth surface functionalization, *Materials Science and Engineering: C* 105 (2019) 110061.

[164] S.H. Um, Y.W. Chung, Y. Seo, H. Seo, M.R. Ok, Y.C. Kim, H.S. Han, J.J. Chung, J.R. Edwards, H. Jeon, Robust Hydroxyapatite Coating by Laser-Induced Hydrothermal Synthesis, *Advanced Functional Materials* 30(48) (2020) 2005233.

[165] N. Armon, E. Greenberg, E. Edri, O. Nagler-Avramovitz, Y. Elias, H. Shpaisman, Laser-Based Printing: From Liquids to Microstructures, *Advanced Functional Materials* 31(13) (2021) 2008547.

[166] A.S. Hamdy, I. Doench, H. Möhwald, Assessment of a one-step intelligent self-healing vanadia protective coatings for magnesium alloys in corrosive media, *Electrochimica Acta* 56(5) (2011) 2493-2502.

[167] A.S. Hamdy, I. Doench, H. Möhwald, Smart self-healing anti-corrosion vanadia coating for magnesium alloys, *Progress in Organic Coatings* 72(3) (2011) 387-393.

[168] S. Hiromoto, Self-healing property of hydroxyapatite and octacalcium phosphate coatings on pure magnesium and magnesium alloy, *Corrosion Science* 100 (2015) 284-294.

[169] Z. Li, T. Wen, Y. Su, X. Wei, C. He, D. Wang, Hollow hydroxyapatite spheres fabrication with three-dimensional hydrogel template, *CrystEngComm* 16(20) (2014) 4202-4209.

[170] S. Hiromoto, M. Inoue, T. Taguchi, M. Yamane, N. Ohtsu, In vitro and

in vivo biocompatibility and corrosion behaviour of a bioabsorbable magnesium alloy coated with octacalcium phosphate and hydroxyapatite, *Acta biomaterialia* 11 (2015) 520-530.

[171] N. Eliaz, T. Sridhar, Electrocrystallization of hydroxyapatite and its dependence on solution conditions, *Crystal Growth and Design* 8(11) (2008) 3965-3977.

[172] M. Tomozawa, S. Hiromoto, Microstructure of hydroxyapatite-and octacalcium phosphate-coatings formed on magnesium by a hydrothermal treatment at various pH values, *Acta Materialia* 59(1) (2011) 355-363.

[173] W. Harun, R. Asri, J. Alias, F. Zulkifli, K. Kadirgama, S. Ghani, J. Shariffuddin, A comprehensive review of hydroxyapatite-based coatings adhesion on metallic biomaterials, *Ceramics International* 44(2) (2018) 1250-1268.

[174] B.-H. Lee, A. Oyane, H. Tsurushima, Y. Shimizu, T. Sasaki, N. Koshizaki, A new approach for hydroxyapatite coating on polymeric materials using laser-induced precursor formation and subsequent aging, *ACS applied materials & interfaces* 1(7) (2009) 1520-1524.

[175] C.M. Jin, W. Lee, D. Kim, T. Kang, I. Choi, Photothermal convection lithography for rapid and direct assembly of colloidal plasmonic nanoparticles on generic substrates, *Small* 14(45) (2018) 1803055.

[176] Z. Yan, R. Bao, C.M. Busta, D.B. Chrisey, Fabrication and formation mechanism of hollow MgO particles by pulsed excimer laser ablation of Mg in liquid, *Nanotechnology* 22(26) (2011) 265610.

Abstract in Korean

마그네슘 합금은 기존 생체재료에 비해 골과 유사한 물성을 가지고 이식 후 골 형성 촉진과 동시에 인체 내에서 분해되기 때문에 새로운 정형외과용 재료로써 주목받고 있다. 그러나 마그네슘 합금의 부식속도는 염화 화합물이 풍부한 체액에서 가속화되고, 특히 부식 초기에 발생하는 급격한 수소기체 및 pH 변화는 과도한 염증 반응 및 주변조직의 섬유화를 유발할 가능성이 있어, 마그네슘 합금을 인체이식용 소재로 사용하기에 제약이 되고 있다. 마그네슘 합금의 초기 부식속도를 제어하기 위하여 다양한 코팅기술에 관한 연구가 활발히 진행되고 있으나 코팅층의 안정성 등 코팅을 이용한 방법도 해결해야 할 문제가 있다.

레이저는 일반 공정 분위기에서 비접촉식 가공이 가능하고 국소 부위에 따른 선택적인 공정이 가능할 뿐만 아니라, 레이저의 펄스폭이나 파장대에 따른 다양한 공정효과를 기대할 수 있기 때문에 많은 활용분야에서 사용되고 있다. 따라서 본 연구에서는, 코팅 기법의 단점 보완 및 성능향상을 위해 레이저를 활용한 표면 처리 및 발전된 코팅기법을 통해, 마그네슘 및 합금의 초기 부식속도 제어와 생체적합성을 향상시키고자 하였다.

첫 번째로, 펨토초 레이저 조건을 다양하게 적용하여 부식을 억제하는 최적 조건을 찾았으며 초기 부식속도를 알기 위해, 각각의 조건에 따라 마그네슘 이온 용출량을 조사한 후, 생체 모사액인 Hanks'balanced salt solution(HBSS)에서 부식평가를 진행하고 주사전자현미경(SEM), X-ray 회절분석법(XRD)를 이용하여 표면과 상변화를 관찰하였다. 단상이 아닌 금속합금에서 대표적인 부식 메카니즘인 갈바닉 부식을 레이저를 이용한 제 2 상의 고용을 통해 부식 저항성을 향상시켰고, 레이저 영향부의 빠른 냉각속도로 인해 결정립이 미세화되어 부식층이 균일하게 형성되므로, 국부 부식을 억제하는 효과를 보였다.

두 번째로, 펨토초 레이저 텍스처링 레이저 공법의 효과를 이용하여 마그네슘 표면을 초친수성의 성질을 갖도록 개질하고, 이를 통해 분해속도 조절을 위한 고분자 코팅능력의 향상을 유도하였다. 레이저 표면 처리하지 않은 마그네슘 그룹과 표면 처리한 마그네슘 그룹에 동일한 조건으로 생분해성 고분자 화합물인 PLGA (poly-lactic-co-glycolic acid)를 동일한 조건으로 스펀코팅하여 일련의 실험들을 진행하였다. 미디어 용액에서 침지부식 후에 마그네슘 용출량을 확인해본 결과, 처리 전에 비해 표면 개질 후 코팅을 진행한 그룹에서 마그네슘 이온양의 감소를 확인할 수 있었다. 이는 부식 후의 단면 결과 역시 일치된 반응을 보여주었다. 특히, 코팅층의 접착력을 측정하여

레이저 처리에 의해 코팅 효과가 향상된 그룹의 코팅이, 그렇지 않은 그룹의 코팅에 비해 더 효과적으로 작용한다는 것을 증명할 수 있었다.

세 번째로, 뼈의 무기질 성분인 하이드록시 아파타이트 (HAp)의 성분이 함유된 전구체 용액 내 레이저 처리를 통해, 코팅재 합성과 코팅이 동시에 가능하게 하였다. 공정상의 이점뿐만 아니라 기존 침지 코팅 방식보다 향상된 코팅능을 다양한 방법으로 확인하였고, 실제 임플란트 스크류로 사용되는 제품에 이 코팅 방식을 적용해봄으로써 산업 현장에서의 적용 가능성을 확인할 수 있었다. 적용된 코팅법에 의해 형성된 레이저 유도 코팅층은 스크래치 하중에도 견디는 성능으로, 장기간 부식 실험에서 향상된 부식저항성 효과를 보였다.

향후, 위의 연구결과를 토대로, 생분해성 제품군에 따라 (예. 스크류, 플레이트, 스캐폴드, 스텐트 등등) 원하는 대로 부식 속도를 제어하여 생분해성 합금의 활용 범위가 더욱 넓어질 뿐만 아니라, 레이저를 이용한 표면처리 및 용액내 코팅 방법을 활용하여 코팅이 적용되는 다양한 분야에도 효과적으로 적용될 것이라 예상된다.